The Dissertation Committee for Tuo Wang Certifies that this is the approved version of the following dissertation:

Atomic Layer Deposition of Amorphous Hafnium-Based Thin Films with Enhance Thermal Stabilities

Committee:

John G. Ekerdt, Supervisor

Alexander A. Demkov

Gyeong S. Hwang

Brian A. Korgel

Charles B. Mullins

Atomic Layer Deposition of Amorphous Hafnium-Based Thin Films with Enhance Thermal Stabilities

by

Tuo Wang, B.S.

Dissertation

Presented to the Faculty of the Graduate School of
The University of Texas at Austin
in Partial Fulfillment
of the Requirements
for the Degree of

Doctor of Philosophy

The University of Texas at Austin
December, 2010

Dedication

To my parents

Acknowledgements

There are many individuals to whom I am grateful for navigating me through the process of this dissertation. Foremost among these, I would like to express my deepest appreciation to my advisor, Professor John G. Ekerdt, for his constant support, guidance, patience and encouragement during my graduate studies. This dissertation could not have possible without him. I am deeply indebted to Prof. Ekerdt who is always available to help me regardless of his busy schedule not only for questions in my academic research but difficulties in all aspects of my life. I consider myself very fortunate to have had him as my advisor. I would also like to thank Prof. Alexander A. Demkov, Prof. Gyeong S. Hwang, Prof. Brian A. Korgel, and Prof. Charles B. Mullins for their insights and generous feedback on my research as great teachers and committee members. I appreciate Prof. Isaac Sanchez for providing me so many helpful advices towards my degree.

I am also very grateful to my talented and hard-working colleagues in our research group. I owe special thanks to Ryan Fitzpatrick, Wes Ahearn, and Luke Henderson, who spent numerous hours in teaching me operating the experimental equipment and answered me innumerous questions. My thanks are also extended to former and current group members, Navneet Salivati, Shawn Coffee, Wyatt Winkenwerder, Kelly Thom, Jinhong Shin, Hyun-Woo Kim, Ben Spivey, Dan Bost, Songyan Jia, Joe McCrate, Blair Cox, Brad Leonhardt, and Tyler Elko-Hansen, for providing me experimental guidance and encouraging research environment. I am also thankful to Jinlong Gong, Ming Pan, and Dave Flaherty, who are in Prof. Mullins research group and provided me helpful assistance on my experiments.

I would like to thank The University of Texas at Austin and the Cockrell School of Engineering for providing me such a great opportunity to pursue my Ph.D. degree. The staff in our department: T Stockman, Kay Swift, Eddie Ibarra, Jim Smitherman, Butch Cunningham, Randy Rife, Kevin Haynes, and Tammy McDade, have been very helpful. I also acknowledge the excellent support from Dr. Bill Lackowski and Mike Tiner in The Center for Nano and Molecular Science and Technology, and the X-ray Diffraction Lab manager, Vince Lynch.

Finally, I am forever grateful to my parents. It was through their love and guidance that I became the person I am today. I only hope I can give them as much as they have given me.

Atomic Layer Deposition of Amorphous Hafnium-Based Thin Films with Enhance Thermal Stabilities

Publication No._____________

Tuo Wang, Ph.D.

The University of Texas at Austin, 2010

Supervisor: John G. Ekerdt

The continuous scaling of microelectronic devices requires high permittivity (high-*k*) dielectrics to replace SiO_2 as the gate material. HfO_2 is one of the most promising candidates but the crystallization temperature of amorphous HfO_2 is too low to withstand the fabrication process. To enhance the film thermal stability, HfO_2 is deposited using atomic layer deposition (ALD), and incorporated with various amorphizers, such as La_2O_3, Al_2O_3, and Ta_2O_5. The incorporation is achieved by growing multiple ALD layers of HfO_2 and one ALD layer of MO_x (M = La, Al, and Ta) alternately (denoted as [xHf + 1M]), and the incorporation concentration can be effectively controlled by the HfO_2-to-MO_x ALD cycle ratio (the x value). The crystallization temperature of 10 nm HfO_2 increases from 500 °C to 900 °C for 10 nm [xHf + 1M] film, where x = 3, 3, and 1 for M = La, Al, and Ta, respectively. The incorporation of La_2O_3 ad Ta_2O_5 will not compromise the dielectric constant of the film because of the high-*k* nature of La_2O_3 and Ta_2O_5. Angle resolved X-ray photoelectron spectroscopy (AR-XPS) reveals that when the HfO_2-to-MO_x ALD cycle ratio is large

enough ($x > 3$ and 4 for La and Al, respectively), periodic structures exist in films grown by this method, which are comprised of repeated M-free HfO_2 ultrathin layers sandwiched between HfM_xO_y layers. Generally, the film thermal stability increases with thinner overall thickness, higher incorporation concentration, and stronger amorphizing capability of the incorporated elements. When the x value is low, the films are more like homogeneous films, with thermal stabilities determined by the film thickness and the amorphizer. When the x value is large enough, the periodically-repeated structure may add an extra factor to stabilize the amorphous phase. For the same incorporation concentration, films with an appropriately high periodicity may have an increased thermal stability. The manner by which the periodic structure and incorporated element affect thermal stability is explored and resolved using nanolaminates comprised of alternating layers of $y\mathrm{HfO_2}$ and $[x\mathrm{Hf} + 1\mathrm{M}] \times n$, where y varied from 2 to 20, x varied from 1 to 2, and n varied from 4 to 22.

Table of Contents

List of Tables xii

List of Figures xiii

List of Illustrations xix

Chapter 1: Introduction 1
  1.1. Overview 1
  1.2. Current Research 3
    1.2.1. HfO_2 as a High-*k* Dielectric Material and Its Drawbacks 3
    1.2.2. HfO_2-Based Ternary Oxides 3
      1.2.2.1. $HfSi_xO_y$, $HfAl_xO_y$, and HfO_xN_y 3
      1.2.2.2. High-*k* Amorphizer: La_2O_3, Ta_2O_5 5
    1.2.3. Known Factors Affecting the Thermal Stability of Thin Films...6
      1.2.3.1. Incorporated Elements and the Amorphous Network Structure They Form 6
      1.2.3.2. Film Thickness and Film Structure 7
  1.3. Objective and Overview of Chapters 9
  1.4. References 12

Chapter 2: Atomic Layer Deposition of Lanthanum Stabilized Amorphous Hafnium Oxide Thin Films 16
  2.1. Introduction 16
  2.2. Experimental Details..17
  2.3 Results and Discussion 20
    2.3.1. Compositional Analysis 20
    2.3.2. Crystallinity and Dielectric Constant..22
    2.3.3. Evidence of a Periodic Structure and Its Comparison to Homogeneous Films 26
  2.4. Summary 31
  2.5. References 31

Chapter 3: Subnanoscale Lanthanum Distribution in Lanthanum-Incorporated Hafnium Oxide Thin Films Grown Using Atomic Layer Deposition 34

3.1 Introduction..........34

3.2. Experimental Details..........37

3.2.1. Film Deposition..........37

3.2.2. Cross-Sectional Transmission Electron Microscopy (TEM) and Atomic Force Microscopy (AFM)..........38

3.2.3. X-ray Photoelectron Spectroscopy (XPS)..........39

3.2.4. Ellipsometry..........39

3.3. Results and Discussion..........40

3.3.1. Angle-Resolved XPS..........42

3.3.2. Void Fraction by Ellipsometry..........51

3.4. Summary..........58

3.5. References..........59

Chapter 4: Optical Properties of La-Incorporated HfO_2 upon Crystallization 62

4.1. Introduction..........62

4.2. Experimental Details..........63

4.3. Results and Discussion..........64

4.4. Summary..........71

4.5. References..........72

Chapter 5: Structure versus Thermal Stability: the Periodic Structure of ALD-Grown Al-Incorporated HfO_2 Films and Its Effect on Amorphous Stabilization.....74

5.1. Introduction..........74

5.2. Experimental Details..........77

5.3. Results and Discussion..........79

5.3.1. Amorphous Stabilization of 10 nm ALD-Grown Al-HfO_2 Films..........79

5.3.2. Periodicity of ALD-Grown Al-HfO_2 Films..........81

5.3.3. Structure versus Thermal Stability..........85

5.4. Summary..........91

5.5. References..........92

Chapter 6: The Relationship between Film Structure and Enhanced Thermal Stability of Ta_2O_3-Incorporated HfO_2 Grown by Atomic Layer Deposition 95

6.1. Introduction...95

6.2. Experimental Details...97

6.3. Results and Discussion 99

6.3.1. XPS Analysis of As-Deposited 10 nm [*x*Hf + 1Ta] Films 99

6.3.2. Thermal Stability of 10 nm [*x*Hf + 1Ta] Films........................102

6.3.3. Dielectric Constant and Leakage Current Density of [2Hf + 1Ta] Films 107

6.3.4. Relationship between Film Structure and Thermal Stability...110

6.4. Summary 122

6.5. References 123

Chapter 7: Research Summary...127

7.1. Conclusion 127

7.2. Recommendations for Future Work...129

Appendix...131

Bibliography 132

Vita………...140

List of Tables

Table 2.1. Comparison of lowest La-incorporation concentration (metal based) that ALD periodic structure and homogeneous films require to suppress crystallization after 800 and 900 °C annealing. 28

Table 3.1. Calculated EALs at the three take off angles that define section II and III; overlayer film thickness at which the corresponding EALs are calculated. 49

List of Figures

Figure 2.1. XP spectra of La 3d, Si 2p, and Hf 4f at different La-incorporation levels. The *x*:*y* designations refer to the HfO_2:La_2O_3 ALD cycle ratios 21

Figure 2.2. Hf, La, and Si atomic concentration (top inset) and La incoorporation level (metal based) as a function of HfO_2:La_2O_3 ALD cycle ratio; bottom inset, O 1s peak for all La-incorporation levels. 22

Figure 2.3. XRD spectra of 10 nm $HfLa_xO_y$ films after 30 s annealing in a N_2 ambient; inset, XRD spectra for 10 nm HfO_2. 23

Figure 2.4. Cross-sectional HRTEM images for samples above and below the La-incorporation levels that stabilize an amorphous structure at (a) 800 and (b) 900 °C. 25

Figure 2.5. CET as a function of physical thickness (measured by SE). HfO_2 films (☐) were annealed at 500 °C for 30 s, and [6Hf + 1La] films (■) were annealed at 800 °C for 30 s. The fits for HfO_2 (dash line) and [6Hf + 1La] (solid line) lead to *k* of 16.7 ± 0.3 and 16.6 ± 0.4, respectively. 26

Figure 2.6. XP spectra of La 3d and Hf 4f spectra of a 10 nm [6Hf + 1La] × 21 sample at take off angle = 8, 9, and 10°. 27

Figure 2.7. XRD spectra of [6Hf + 1La] films of different thickness (3, 10, 30, and 50 nm) after 800 and 1000 °C annealing under a N_2 ambient for 30 s. 29

Figure 3.1. Cross-sectional TEM images for two as-deposited samples at (a) high La-incorporation level, [3Hf + 1La] × 41; and (b) low La-incorporation level, [9Hf + 1La] × 14. Both samples are homogeneous in TEM...41

Figure 3.2. X-ray photoelectron spectra of Hf 4f and La 3d of a 10 nm as-deposited [4Hf + 1La] × 32 sample at (a, b)normal 45° take off angle; and at (c, d) near-grazing take off angles. 43

Figure 3.3. (La 3d)/(O 1s) photoelectron intensity ratio of a 10 nm as-deposited [4Hf + 1La] × 32 sample. $14° \leq \theta \leq 18°$ and $18° \leq \theta \leq 25°$ represent the second HfO_2 and $HfLa_xO_y$ layer from the sample surface, respectively. 45

Figure 3.4. (La 3d)/(O 1s) photoelectron intensity ratio of a set of [xHf + 1La] samples. (a) When $x = 2, 3$, the films are more like homogeneous mixtures; (b) when $x = 4, 6, 8$, the existence of an $HfLa_xO_y$–HfO_2–$HfLa_xO_y$ structure is confirmed by the features marked as sections I, II, and III. 47

Figure 3.5. (a) Overall atomic percentage of Hf, La, and Si impurities; (b) and volume fraction of $LaSi_yO_x$ ($f_{A,2}$) in solids of a set of 10 nm as-deposited [xHf + 1La] films, where $x = 1$–6. 54

Figure 3.6. AFM images of as-deposited 10 nm (a) [2Hf + 1La] × 45 and (b) [6Hf + 1La] × 22 samples; the rms roughness is (a) 0.139 and (b) 0.132 nm. 55

Figure 3.7. Void fractions of six as-deposited 10 nm [xHf + 1La] films, where x=1–6; inset, a typical ellipsometry spectrum of as-deposited 10 nm [1Hf + 1La] × 84. 56

Figure 4.1. (a) ε_2 of the dielectric constant and (b) E_g determined from the Tauc plot for 10 nm HfO_2 films upon different annealing conditions. Inset, XRD spectra of 10 nm HfO_2. 65

Figure 4.2. (a) ε_2 of the dielectric constant and (b) E_g determined from the Tauc plot for 10 nm as-deposited HfO_2 and $[x\text{Hf} + 1\text{La}] \times n$, where $x = 6$ and 1. 66

Figure 4.3. ε_2 of 10 nm (a) [6Hf + 1La] and (b) [3Hf + 1La], for as-deposited, and at the highest annealing temperature to remain amorphous (800 and 900 °C, respectively), and at the temperature at which the films crystallize (900 and 1000 °C, respectively). 68

Figure 4.4. E_g determined from the Tauc plot for 10 nm (a) [6Hf + 1La] and (b) [3Hf + 1La], for as-deposited, and at the highest annealing temperature to remain amorphous (800 and 900 °C, respectively), and the temperature at which the film crystallizes (900 and 1000 °C, respectively). 69

Figure 4.5. ε_2 of 10 nm crystallized HfO_2, [6Hf + 1La], and [3Hf + 1La]. 70

Figure 5.1. The Al-incorporation level of as-deposited Al-HfO_2 films versus Hf:Al ALD cycle ratio...79

Figure 5.2. XRD spectra showing the minimum Al-incorporation levels for 10 nm Al-HfO_2 films to remain amorphous after 800 and 900 °C annealing for 30 s in a N_2 environment...81

Figure 5.3. (Al 2p)/(O 1s) photoelectron intensity ratios of (a)10 nm Al_2O_3; (b) [8Hf + 1Al] × 14 and [5Hf + 1Al] × 21; (c) [4Hf + 1Al] × 23; (d) [3Hf + 1Al] × 28 and [2Hf + 1Al] × 35 films; error bars at 7, 12, 18, 22, and 26° for the [4Hf + 1La] × 23 sample are shown at the corresponding data points, respectively. 82

Figure 5.4. XRD spectra of (a) 10 nm as-deposited HfO_2 and HfO_2 annealed at 450, 500, and 550 °C; (b) 40 nm as-deposited HfO_2 and HfO_2 annealed at 400 °C. 86

Figure 5.5. XRD spectra of (a) 10 nm and (b) 40 nm [3Hf + 1Al] films annealed at 900 °C (10 nm [3Hf + 1Al] is annealed at 950 °C for comparison); (c) 10 nm and (d) 40 nm [8Hf + 1Al] films annealed at 800 °C (10 nm [8Hf + 1Al] is annealed at 850 °C for comparison). 87

Figure 5.6. XRD spectra of (a) 10 nm and (b) 40 nm [3Hf + 1La] films annealed at 900 °C (10 nm [3Hf + 1La] is annealed at 950 °C for comparison); (c) 10 nm and (d) 40 nm [6Hf + 1La] films annealed at 800 °C (10 nm [6Hf + 1La] is annealed at 850 °C for comparison). 89

Figure 6.1. XP spectra of Ta 4f, O 1s, and Hf 4f peaks for as-deposited 10 nm [xHf + 1Ta] × n (x = 1, 4, and 8), Ta_2O_5, and HfO_2. 100

Figure 6.2. Atomic Ta-incorporation concentration of as-deposited Ta-HfO_2 versus HfO_2:Ta_2O_5 ALD cycle ratio. 101

Figure 6.3. XRD spectra of 10 nm (a) HfO_2 annealed at 450 and 500 °C, and (b) Ta_2O_5 annealed at 750 and 800 °C for 30 s in a N_2 ambient. 103

Figure 6.4. XRD spectra of 10 nm [xHf + 1Ta] (x = 1, 2, 7, and 8 from (a) to (d), respectively, after various annealing temperatures for 30 s in a N_2 ambient. $^{\alpha}$Atomic Ta/(Hf + Ta)%. 104

Figure 6.5. Crystallization onset temperatures for 10 nm [*x*Hf + 1Ta] × *n* samples (x = 1–8). 106

Figure 6.6. CET as a function of as-deposited [2Hf + 1Ta] film thickness. The solid line is the linear fit. 107

Figure 6.7. Leakage current density (*J*) versus voltage of (a) 10 nm Ta_2O_5 and (b) 10 nm [2Hf + 1Ta], as-deposited, after 700 and 800 °C 30 s annealing; (c) leakage current density (*J*) versus electric filed (*E*) of 10 nm Ta_2O_5 and [2Hf + 1Ta] after 700 °C 30 s annealing. 108

Figure 6.8. Leakage current density (*J*) versus electric filed (*E*) of as-deposited thinner (10 nm) and thicker (40 nm) [2Hf + 1Ta], and 800 °C annealed thinner (10 nm) and thicker (40 nm) [2Hf + 1Ta]. 109

Figure 6.9. XRD spectra of 10 nm [2Hf + 1Ta] × 54, {5Hf + [1Hf + 1Ta] × 5} × 10, and {10Hf + [1Hf + 1Ta] × 10} × 5 after 800 °C annealing, and their corresponding illustrations. Ta can be regarded as homogeneously distributed in [2Hf + 1Ta] and [1Hf + 1Ta]. Inset: qualitative presentation of La% distribution in different layers, highlighting the transition from $HfTa_xO_y$ in the [1Hf + 1Ta] × 5 layer to the HfO_2-only layer. 112

Figure 6.10. Crystallization temperatures and structure illustrations of 10 nm HfO_2-$HfTa_xO_y$ nanolaminate films for two comparisons. First comparison: fixed $HfTa_xO_y$ layer thickness with thinner HfO_2, (b)→(a)→(c); second comparison: fixed HfO_2 layer thickness with thinner $HfTa_xO_y$, (d)→(a)→(e). Sample (a) is the standard and $HfTa_xO_y$ layers are grown as [1Hf + 1Ta]. 115

Figure 6.11. Crystallization temperatures and structure illustrations of 10 nm HfO_2-$HfAl_xO_y$ nanolaminate films for two comparisons. First comparison: fixed $HfAl_xO_y$ layer thickness with thinner HfO_2, (b)→(a)→(c); second comparison: fixed HfO_2 layer thickness with thinner $HfAl_xO_y$, (d)→(a)→(e). Sample (a) is the standard and $HfAl_xO_y$ layers are grown as [2Hf + 1Al]. 118

List of Illustrations

Illustration 1.1. Pictorial presentation of an n-channel MOSFET highlighting the gate dielectric layer. 2

Illustration 2.1. Pictorial presentation of the periodic structure during the intermediate state of the crystallization process 30

Illustration 3.1. Schematic illustration of elastic scattering at small take off angles. Photoelectrons from a deeper depth may make their way to the sample surface through a shortcut caused by elastic scattering. 49

Illustration 3.2. Pictorial presentation of the $HfLa_xO_y$–HfO_2–$HfLa_xO_y$ structure in [4Hf + 1La], [6Hf + 1La], and [6Hf + 1La] films. The relative thickness is calculated from the EAL × sin θ values in Table 3.1. 50

Illustration 3.3. Schematic illustration of a film described by an EMA model, which incorporates a solid (material A) with its separate EMA model and voids (material B). Volume fractions f_A, f_B are fitted to the spectra; volume fractions $f_{A,1}, f_{A,2}$ are calculated from the measured atomic composition. The optical properties of HfO_2 and La_2O_3 are measured from two 100 nm thick samples. 53

Chapter 1: Introduction

1.1. OVERVIEW

The continuous scaling of complementary metal-oxide-semiconductor (CMOS) technology has enabled the Si-based microelectronics industry to stimulate the world's extraordinary economic expansion over the past fifty years. As predicted by the well-known Moore's Law, the number of transistors on an integrated circuit doubles every 18 to 24 months, which has been achieved by scaling the transistor dimensions that requires a corresponding reduction in the gate dielectric thickness. Although thermally grown SiO_2 has been used as the ideal gate dielectric material for decades because the SiO_2–Si interface might be one of the most perfect interfaces from a device perspective, this material is fast approaching its thickness limit. As the SiO_2 thickness is reduced to about 2 nm, a large gate leakage current flows across the dielectric because of direct tunneling. To continue scaling semiconductor devices below 45 nm, which would require a SiO_2 dielectric thinner than 1.2 nm, new materials need to be introduced into Si-dominated technology.[1]

Illustration 1.1 explains the relationship between the device scaling and the dielectric constant of the gate material. The Field effect transistor (FET) is the key element of CMOS technology. The saturation current of a metal oxide semiconductor FET (MOSFET) can be approximately written as $I_{D.Sat} \propto \frac{C \times W}{L_g}(V_g - V_t)^2$, where $I_{D.Sat}$ is the saturation current, C is the capacitance of unit area, L_g is the gate length, W is the gate width, V_g is the gate voltage, and V_T is the threshold voltage. Assume a parallel plate capacitor, $C = \frac{k\varepsilon_0}{d}$, where k is the dielectric constant, ε_0 is the permittivity of free space, and d is the thickness of the gate material. Thus, $I_{D.Sat} \propto \frac{W \times d}{k \times L_g}(V_g - V_t)^2$. Moore's Law dictates that the reduction of the gate length L_g has to be compensated by the same reduction of thickness d to maintain the capacitance. However, as the thickness of SiO_2 approaches to around 2 nm, the quantum mechanical phenomenon of electron tunneling occurs between the gate and channel, leading to increased power consumption. Therefore, the semiconductor industry requires alternative gate dielectrics with dielectric constants higher than that of SiO_2 to achieve the same gate capacitance with a thicker physical dielectric thickness and a lower gate leakage current.

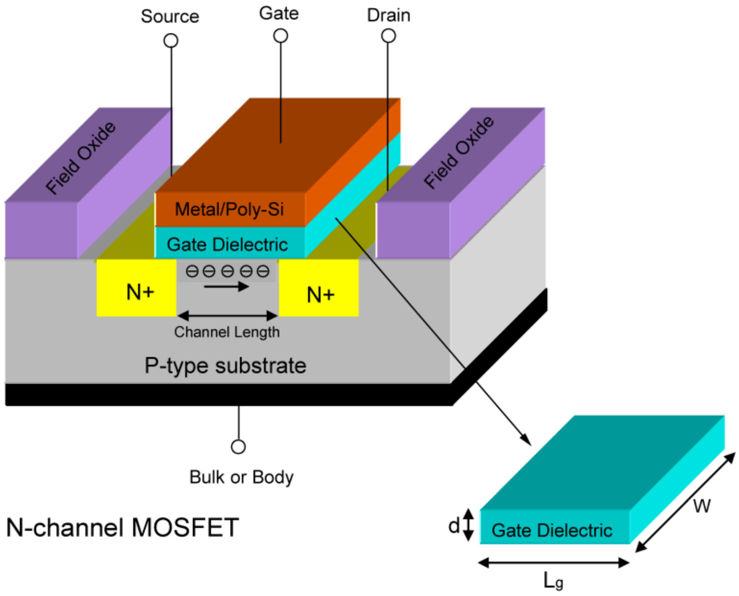

Illustration 1.1. Pictorial presentation of an n-channel MOSFET highlighting the gate dielectric layer.

1.2. CURRENT RESEARCH

1.2.1. HfO_2 as a High-*k* Dielectric Material and Its Drawbacks

In recent years, HfO_2 has become one of the most promising dielectric materials to replace conventional SiO_2 because of its high dielectric constant ($k \sim 20$), relatively wide bandgap (~ 5.5 eV) and relatively good stability on Si.[1–5] However, HfO_2 suffers from a major disadvantage. It easily crystallizes under low temperature annealing (~ 500 °C). Most HfO_2 films grown by chemical vapor deposition (CVD) and atomic layer deposition (ALD) are amorphous as-grown.[2,6] But after the post deposition densification anneal (450 °C) and the high temperature dopant activation anneal (~1000 °C), amorphous HfO_2 crystallizes into a mixed polycrystalline phase where the monoclinic phase is dominant. The resultant grain boundaries in the film may serve as charge leakage paths and increase leakage current. Moreover, different phases may coexist in polycrystalline HfO_2 thin films,[7–9] and the polymorphs have different dielectric constants (tetragonal ~70, cubic ~29, and monoclinic ~16),[10] which leads to a spatially-varying dielectric constant. Zhao and Vanderbilt have shown that the dielectric constant varies by as much as 50% between different phases,[10] resulting in devices with variable capacitance values among different regions. Thus it is desirable to find methods to stabilize the amorphous phase of HfO_2 under the high temperature annealing conditions in the device fabrication process, although crystalline HfO_2 has a higher dielectric constant than amorphous phase with reported values ranging from .13 to 20.

1.2.2. HfO_2-Based Ternary Oxides

1.2.2.1. $HfSi_xO_y$, $HfAl_xO_y$, and HfO_xN_y

Extensive effort has been made to stabilize the amorphous phase of HfO_2. One of the methods is incorporating HfO_2 with a robust amorphous dielectric, such as SiO_2 or

Al_2O_3. Hf-silicates ($HfSi_xO_y$) and Hf-aluminates ($HfAl_xO_y$) are among the most well-researched HfO_2-based ternary oxides. An obvious advantage of $HfSi_xO_y$ is that the incorporated SiO_2 has a very high thermal stability, and its affinity with the Si substrate is relatively good because the $HfSi_xO_y$–Si interface has a similar interface quality as SiO_x–Si interface.[1] But SiO_2 has a low k value (~ 3.9). Although it is reported that a small amount of Si (~ 8%, cation basis) in $HfSi_xO_y$ may increase the dielectric constant of the film because of the transformation from the monoclinic to the tetragonal phase of crystallized HfO_2,[11] a large amount of Si (~ 50%, cation basis) in $HfSi_xO_y$ is needed for the film to remain amorphous at the 800 ~ 900 °C annealing range, which decreases the dielectric constant to less than 10,[12] reducing the advantage of the high-k film.

ALD-grown Al_2O_3 has a dielectric constant of 10,[13] thus the higher k property of Al_2O_3 is expected to be reflected in Hf-aluminates. Besides being an amorphous dielectric with high crystallization temperature, Al_2O_3 has other unique advantages such as a large bandgap (~ 8.8 eV) and Al_2O_3 is a good barrier to oxygen diffusion and protects the Si surface from oxidation.[14–16] It is widely reported that $HfAl_xO_y$ can remain amorphous at an annealing temperature higher than 900 °C.[17–19] But a 20 nm $HfAl_xO_y$ film required 25% Al (metal basis) to remain amorphous at 900°C,[17] which reduces the dielectric constant from ~ 20 to ~ 12.[19,20]

Hafnium oxynitrides (HfO_xN_y) are shown to suppress the crystallization commonly observed for HfO_2 films upon high temperature annealing.[21] Incorporating nitrogen is known to form a diffusion barrier for boron, preventing the dopant diffusion from the B-doped poly-Si gate.[22,23] It is also found that the atomic N could passivate O vacancies in the gate dielectrics during the nitridation process and remove electron leakage paths mediated by O vacancies, thus reduce the electron leakage current.[24,25] However, N-incorporation suffers from the fact that the incorporation of N atoms into interstitial sites causes a serious issue of bandgap narrowing for the gate dielectric.[24] A possible solution is that high temperature annealing may help to break N–O bonds and make N atoms move around in the dielectric to form stable N–Hf bonds. This will increase the bandgap and band offsets of a nitrided dielectric film so that the high-*k* material can have a sufficient injection barrier to be used as alternative gate dielectric.[25]

1.2.2.2. High-k Amorphizer: La_2O_3, Ta_2O_5

Although $HfSi_xO_y$ and $HfAl_xO_y$ achieve higher crystallization temperatures, their dielectric constant values decrease below that of HfO_2. Thus it is obvious that future CMOS device scaling requires new dielectric materials with both high crystallization temperature and high dielectric constant.

La_2O_3 ($k \sim 20$),[26,27] and Ta_2O_5 ($k \sim 27$)[28] have been considered as high-*k* dielectrics to replace SiO_2 as the gate material. Unfortunately, oxygen may diffuse through La_2O_3 and cause the growth of La-silicate at the Si interface upon annealing,[29,30] reducing the overall capacitance values. Another objection to La_2O_3 is that it easily turns into $La(OH)_3$ with ambient H_2O.[31–33] The performance of La_2O_3 dielectrics appears to be rather unstable compared to HfO_2, when La_2O_3 and HfO_2 are synthesized and examined under similar reactor conditions.[34] Ta_2O_5 also easily reacts with Si and forms a low-*k* interfacial layer upon annealing, which drastically reduces the effective *k* value.[1] Ta_2O_5 has a relatively small bandgap (4.4 eV) and electron band offset (0.3 eV) with respect to Si.[35] An even more serious disadvantage of Ta_2O_5 is the reported high leakage current density because of oxygen vacancies and/or impurities in the film.[36,37] Thus it is unlikely for pure La_2O_3 or Ta_2O_5 to be used as the high-*k* dielectric layer in CMOS devices.

On the other hand, it is reported that incorporating La_2O_3 and Ta_2O_5 into HfO_2 effectively increase the crystallization temperature of the film. The advantages of HfO_2, such as good stability on Si, relatively wide bandgap (~ 5.5 eV), can be retained as long as the film is still HfO_2-dominant. Moreover, it is expected that incorporating La_2O_3 and Ta_2O_5 will not cause the degradation of the dielectric constant, in contrast to SiO_2 or Al_2O_3. $HfLa_xO_y$ films grown by cosupttering with 33% and 40% La (metal basis) remain amorphous after annealing at 800 and 900 °C, respectively. The dielectric constant of the 40% La (metal basis) $HfLa_xO_y$ film is about 22. The C–V characteristics demonstrate good qualities at Si–$HfLa_xO_y$ interface and few fixed charges in the film.[38] $HfTa_xO_y$ has also been grown by cosputtering, with a crystallization temperature of 900 °C when the Ta concentration is 40% (metal basis).[39] The $HfTa_xO_y$ MOSFETs have higher electron mobility than controlled HfO_2 control devices.[39]

1.2.3. Known Factors Affecting the Thermal Stability of Thin Films

1.2.3.1. Incorporated Elements and the Amorphous Network Structure They Form

The thermal stability of amorphous HfO_2 films can be enhanced by incorporating appropriate elements.[17,18,38–40] The relative effectiveness of the incorporated elements can be reflected by the structures of the amorphous oxides they form. The network structures of the amorphous oxides reported recently for gate dielectric applications can be classified into three categories: continuous random network (CRN), random close packed (RCP) structure, and modified continuous random network (MCRN). The differences between different amorphous structures are related to the molar volume and the coordination number versus the metal-oxygen (M–O) distance,[41,42] as well as the electronegativity difference between M and O, and average bond ionicity.[42] The conventional gate material, thermally grown SiO_2, has a CRN structure; while the high-k substituent in this study, HfO_2, has a RCP structure.[42] For the three amorphizers incorporated into HfO_2 in this study, La_2O_3 forms a RCP structure; Al_2O_3 and Ta_2O_5 form MCRN structure.

Generally speaking, a CRN material has a higher thermal stability than a RCP material. While forming a CRN structure, each atom in SiO_2 is bonded according to its primary chemical valence and predominantly forms covalent bonds.[43] The Si–O covalent bonds in SiO_2 make SiO_2 a very stable amorphous material. The Hf–O bond in HfO_2 is predominantly ionic,[44] thus O atoms can move around more easily compared with O atoms in SiO_2. Therefore, HfO_2 has a much lower crystallization temperature than SiO_2.

When incorporating RCP materials into HfO_2, The RCP material may either be an amorphizer or a crystallizer. La_2O_3 forms a RCP structure and incorporating La_2O_3 into HfO_2 has been shown to be effective in stabilizing the amorphous phase.[38,45,46] Although La_2O_3 is a much weaker amorphizer compared with SiO_2, La-incorporation does not decrease the dielectric constant of the film as found with SiO_2.[38,45] On the other hand, Y_2O_3 also forms a RCP structure but Y-incorporation stabilizes the cubic phase of HfO_2.[47,48]

The MCRN structure is intermediate between CRN and RCP, in which metal atom ionic bonds disrupt and modify the covalently bonded CRN structure.[43] Comparing the electronegativity difference between M and O, and average bond ionicity, some MCRN materials are more CRN-like, or SiO_2-like, such as Al_2O_3; while some others are more RCP-like, such as Ta_2O_5. The CRN-like MCRN materials are stronger amorphizers, but RCP-like MCRN materials have higher dielectric constants, thus the choice of incorporating elements involves an optimization/compromise between higher thermal stability and higher dielectric constant.

1.2.3.2. Film Thickness and Film Structure

When films are very thin, they are not in a thermal equilibrium, but in a quasi-equilibrium,[42] and the thermodynamically unstable phases for bulk materials may become stable for thin films. Thus the crystallization temperature of a thin film is closely related to the film thickness. It is reported that while as-deposited 45 Å thick HfO_2 is amorphous, thicker films are grown as a polycrystalline structure of monoclinic or tetragonal phases.[49] The dependence of film crystallization temperature on the thickness of HfO_2 films is also reported. The crystallization temperature increases from 430 to 600 °C with thickness decreases from 40 to 5 nm.[2] The overall energy of a film is determined by the contributions from both the bulk and the surface. Generally crystalline materials have lower energy than the corresponding amorphous materials. But Navrotsky revealed that monoclinic HfO_2 and ZrO_2 are found to have the largest surface enthalpy and amorphous HfO_2 and ZrO_2 the smallest surface enthalpy.[50] As film thickness decreases, the surface energy of the amorphous phase makes a greater contribution to the total energy, which enables the film to remain amorphous. This is the reason why thinner as-deposited HfO_2 is more likely to be amorphous while thicker films are more easily to crystallize.

It is important to specify the film thickness when discussing the crystallization temperature of a thin film, otherwise it would be difficult to compare the effectiveness of the amorphous stabilization abilities of different incorporated elements. For example, about 50% of Si is needed in $HfSi_xO_y$ for the film to remain amorphous at the 800 ~ 900 °C range,[12] and 25% Al is needed in $HfAl_xO_y$ for the film to remain amorphous at 900 °C.[17] But it can not be concluded that Al is a stronger amorphizer than Si, only based on these two concentration values, because the $HfSi_xO_y$ film in Ref 12 is 200 ~ 300 nm, and the $HfAl_xO_y$ in Ref 17 is only 20 nn. Before comparing the amorphous stabilization effects of different amorphizers, one has to make sure that all the films under comparison are of the same/similar thickness.

1.3. OBJECTIVE AND OVERVIEW OF CHAPTERS

The objectives of this work are to stabilize the amorphous phase of HfO_2 upon annealing by incorporating amorphizing elements and to develop and explanation for how the amorphizer functions. The basic idea is to incorporate another element or oxide into HfO_2, i.e., add an amorphizer. The initial intent was to search for possible high-*k* amorphizers so that the incorporation does not degrade the dielectric constant of the film as SiO_2 or Al_2O_3 do. As the research moved forward, relationships between film structure and thermal stability were noticed and studied. This dissertation gives a comprehensive study describing the amorphous-stabilization mechanism in ALD-grown thin films, in the following order from Chapter 2 to 6. Chapter 2 shows that incorporating La_2O_3 into HfO_2 using ALD is an effective method to grow amorphous high-*k* thin films without compromising the dielectric constant. Chapter 3 investigates the spatial distribution of La in ALD-grown, La-incorporated HfO_2 thin films, and confirms the existence of HfO_2–$HfLa_xO_y$ periodic structures in certain films. By examining the optical properties, Chapter 4 studies the structure change of La-incorporated HfO_2 upon amorphous-to-crystalline phase transformation. In Chapter 5, Al_2O_3, which forms a different amorphous network structure than La_2O_3, is used to stabilize the amorphous phase of HfO_2, and reveals the relationship between film structure and thermal stability. Chapter 6 chooses Ta_2O_5 as another high-*k* amorphizer to suppress crystallization, and investigates the crystallization mechanism in ALD-grown films with HfO_2–HfM_xO_y periodic structures (M = incorporated element). A summary of the work and suggestions for future research are presented in Chapter 7.

Chapter 2 studies ALD-grown La-incorporated HfO_2 thin films. X-ray photoelectron spectroscopy (XPS) shows that the La-incorporation level can be controlled by varying the HfO_2 to La_2O_3 ALD cycle ratios. Microstructure is determined with X-ray diffraction (XRD) and cross-sectional transmission electron microscopy (TEM). The introduction of La increases the film crystallization temperature from 500 °C for a HfO_2 film to 800, 900 and 950 °C for 10 nm films containing 13% La (metal basis), 25% La and 43% La, respectively. The results indicate that ALD incorporating La_2O_3 into HfO_2 is a potential method to grow amorphous HfO_2-based high-*k* dielectric thin films

In many cases, the ALD-grown ternary system is neither a nanolaminate with clear layer interface nor a homogeneous mixture. And the distribution of the incorporated element is a critical factor determining the film properties. Chapter 3 provides an in-depth study of the subnanoscale spatial distribution (in the growth direction) of La in La-incorporated HfO_2 thin films grown by ALD. The (La 3d)/(O 1s) photoelectron intensity ratios are examined by angle resolved XPS (AR-XPS), which confirms the existence of a $HfLa_xO_y$–HfO_2–$HfLa_xO_y$ structure. The film void fractions are acquired from ellipsometry, which shows an abrupt decrease of film void fraction after two HfO_2 growth cycles. More than two and less than three ALD HfO_2 layers interact with one ALD layer of La_2O_3 in such a way that the first two ALD HfO_2 layers mismatch with La_2O_3 and form a HfO_2–La_2O_3 mixture with a different structure compared to films with a third ALD HfO_2 layer that completes the formation of a continuous HfO_2 surface. At least four ALD HfO_2 layers are required for La-free HfO_2 interval layers to exist in the film.

Chapter 4 investigates the change of the imaginary part of the dielectric constant (ε_2) and the bandgap energy (E_g) of HfO_2 and La-incorporated HfO_2 (La-HfO_2) upon crystallization, which would reflect the film structure change during the amorphous-to-crystalline phase transformation. As-deposited HfO_2 and La-HfO_2 have similar absorption tails, implying the existence of disorder in the amorphous film structure and band tails in the gap. Upon crystallization, the absorption tails are reduced and E_g increases for both HfO_2 and La-HfO_2. But disorder still exists and interband states form in pure HfO_2, whereas crystallized La-HfO_2 is almost free of disorder, which might be the result of La atoms forced into the HfO_2 network, forming a new $HfLa_xO_y$ network after crystallization.

Al_2O_3 is used as the amorphizer in Chapter 5. It is know that amorphous Al_2O_3 forms a MCRN, which is thermally more stable than the RCP structure of HfO_2. Besides the widely reported amorphizing capability of Al_2O_3, it is found the thermal stability of ALD-grown Al-HfO_2 films with periodic structures is less dependent on film thickness, whereas pure HfO_2 and homogeneous-like Al-HfO_2 films lose their thermal stabilities with thicker film thickness. The distribution of Al in ALD-grown Al-HfO_2 is studied using AR-XPS. Films with a Hf:Al ALD cycle ratio > 4 have a periodic HfO_2–$HfAl_xO_y$ structure, while films with a Hf:Al ALD cycle ratio < 4 appear more like homogeneous films. Increasing the thickness of a homogeneous-like film (Hf:Al = 3:1 ALD cycle ratio) from 10 nm to 40 nm leads to crystallization when annealed at 900 °C (The crystallization temperature T_c of the 10 nm 3:1 film is lower than 950 °C). Amorphous films with a periodic structure (Hf:Al = 8:1, ALD cycle ratio) do not display a dependence of crystallization on film thickness at the same 800 °C annealing condition (The T_c of the 10 nm 8:1 film is lower than 850 °C). Changing the periodic structure of an ALD-grown Al-incorporated HfO_2 film is shown to be a potential method to tune the film thermal stability.

In Chapter 6, Ta_2O_5, which has a higher dielectric constant than HO_2, is used as the amorphizer. 10 nm films with HfO_2:Ta_2O_5 ALD cycle ratio equals to 1:1 and 2:1 remain amorphous up to 900 and 750 °C, respectively. The thermal stability of the 1:1 film is higher than both 10 nm HfO_2 and Ta_2O_5; the dielectric constant of the 2:1 film is

21.5, higher than HfO_2 grown in the same condition. HfO_2–$HfTa_xO_y$ nanolaminates are grown to study the crystallization mechanism of the nanolaminates, as well as films composed of repeated [one ALD layer of Ta_2O_5 + x ALD layers of HfO_2] structures, where x is large enough to form periodic structures with Ta-free HfO_2 ultrathin layers. For both the nanolaminate and periodic films, crystallization starts from the HfO_2 ultrathin layers, and the $HfTa_xO_y$ layers block the growth of the crystalline phase. The thermal stability of these two kinds of non-homogeneous films is influenced by the Ta concentration in the $HfTa_xO_y$ layers, thickness of the HfO_2 layers, and thickness of the $HfTa_xO_y$ layers, with different degrees of controllability. For a general periodically-structured HfM_xO_y film (M = an incorporated element), films with an appropriately high periodicity are shown to have an extra thermal stability.

1.4. REFERENCES

(1) Wilk, G. D.; Wallace, R. M.; Anthony, J. M. *J. Appl. Phys.* **2001**, *89*, 5243–5275.

(2) Gusev, E. P.; Cabral, C.; Copel, M.; D'Emic, C.; Gribelyuk, M. *Microelectron. Eng.* **2003**, *69*, 145–151.

(3) Kukli, K.; Aarik, J.; Uustare, T.; Lu, J.; Ritala, M.; Aidla, A.; Pung, L.; Harsta, A.; Leskela, M.; Kikas, A.; Sammelselg, V. *Thin Solid Films* **2005**, *479*, 1–11.

(4) Kukli, K.; Pilvi, T.; Ritala, M.; Sajavaara, T.; Lu, J.; Leskela, M. *Thin Solid Films* **2005**, *491*, 328–338.

(5) Hausmann, D. M.; Kim, E.; Becker, J.; Gordon, R. G. *Chem. Mater.* **2002**, *14*, 4350–4358.

(6) Chiou, Y.; Chang, C.; Wu, T. *J. Mater. Res.* **2007**, *22*, 1899–1906.

(7) Mommer, N.; Lee, T.; Gardner, J. A. *J. Mater. Res.* **2000**, *15*, 377–381.

(8) Garvie, R. C. *J. Phys. Chem.* **1978**, *82*, 218–224.

(9) Wang, J.; Li, H. P.; Stevens, R. *J. Mater. Sci.* **1992**, *27*, 5397–5430.

(10) Zhao, X.; Vanderbilt, D. *Phys. Rev. B*. **2002**, *65*, 233106/1–233106/4.

(11) Tomida, K.; Kita, K.; Toriumi, A. *Appl. Phys. Lett.* **2006**, *89*, 142902/1–142902/3.

(12) Neumayer, D. A.; Cartier, E. *J. Appl. Phys.* **2001**, *90*, 1801–1808.

(13) Ghiraldelli, E.; Pelosi, C.; Gombia, E.; Chiavarotti, G.; Vanzetti, L. *Thin Solid Films* **2008**, *517*, 434–436.

(14) Gusev, E. P.; Copel, M.; Cartier, E.; Baumvol, I. J.; Krug, C.; Gribelyuk, M. A. *Appl. Phys. Lett.* **2000**, *76*, 176–178.

(15) Copel, M.; Cartier, E.; Gusev, E. P.; Guha, S.; Bojarczuk, N.; Poppeller, M. *Appl. Phys. Lett.* **2001**, *78*, 2670–2672.

(16) Lee, P. F.; Dai, J. Y.; Wong, K. H.; Chan, H. L.; Choy, C. L. *Appl. Phys. Lett.* **2003**, *82*, 2419–2421.

(17) Ho, M.; Gong, H.; Wilk, G. D.; Busch, B. W.; Green, M. L.; Lin, W. H.; See, A.; Lahiri, S. K.; Loomans, M. E.; Raisanen, P. I.; Gustafsson, T. *Appl. Phys. Lett.* **2002**, *81*, 4218–4220.

(18) Essary, C. R.; Ramani, K.; Craciun, V.; Singh, R. K. *Appl. Phys. Lett.* **2006**, *88*, 182902/1–182902/3.

(19) Zhu, W.; Tamagawa, T.; Gibson, M.; Furukawa, T.; Ma, T. *IEEE Electron. Device Letters*. **2002**, *23*, 649–651.

(20) Marshall, P. A.; Potter, R.; Jones, A. C.; Chalker, P. R.; Taylor, S.; Critchlow, G. W.; Rushworth, S. A. *Chem. Vap. Deposition* **2004**, *10*, 275–279.

(21) Choi, K.; Kim, J.; Yoon, S.; Shin, W. *J. Vac. Sci. Technol., B* **2004**, *22*, 1755–1758.

(22) Kang, C. S.; Cho, H.; Onishi, K.; Nieh, R.; Choi, R.; Gopalan, S.; Krishnan, S.; Han, J. H.; Lee, J. C. *Appl. Phys. Lett.* **2002**, *81*, 2593–2595.

(23) Choi, J.; Puthenkovilakam, R.; Chang, J. P. *J. Appl. Phys.* **2006**, *99*, 053705/1–053705/3.

(24) Umezawa, N.; Shiraishi, K.; Ohno, T.; Watanabe, H.; Chikyow, T.; Torii, K.; Yamabe, K.; Yamada, K.; Kitajima, H.; Arikado, T. *Appl. Phys. Lett.* **2005**, *86*, 143507/1–143507/3.

(25) Wang, S. J.; Chai, J. W.; Dong, Y. F.; Feng, Y. P.; Sutanto, N.; Pan, J. S.; Huan, A. C. *Appl. Phys. Lett.* **2006**, *88*, 192103/1–192103/3.

(26) Guha, S.; Cartier, E.; Gribelyuk, M. A.; Bojarczuk, N. A.; Copel, M. C. *Appl. Phys. Lett.* **2000**, *77*, 2710–2712.

(27) He, W.; Schuetz, S.; Solanki, R.; Belot, J.; McAndrew, J. *Electrochem. Solid-State. Lett.* **2004**, *7*, G131–G133.

(28) Gu, D.; Li, J.; Dey, S. K.; De Waard, H.; Marcus, S. *J. Vac. Sci. Technol., B* **2006**, *24*, 2230–2235.

(29) Copel, M.; Cartier, E.; Ross, F. M. *Appl. Phys. Lett.* **2001**, *78*, 1607–1609.

(30) Stemmer, S.; Maria, J.; Kingon, A. I. *Appl. Phys. Lett.* **2001**, *79*, 102–104.

(31) De Asha, A. M.; Critchley, J. T.; Nix, R. M. *Surf. Sci.* **1998**, *405*, 201–214.

(32) Nieminen, M.; Putkonen, M.; Ninisto, L. *Appl. Surf. Sci.* **2001**, *174*, 155–166.

(33) Cheng, J.; Li, A.; Shao, Q.; Ling, H.; Wu, D.; Wang, Y.; Bao, Y.; Wang, M.; Liu, Z.; Ming, N. *Appl. Surf. Sci.* **2004**, *233*, 91–98.

(34) Triyoso, D. H.; Hegde, R. I.; Grant, J.; Fejes, P.; Liu, R.; Roan, D.; Ramon, M.; Werho, D.; Rai, R.; La, L. B.; Baker, J.; Garza, C.; Guenther, T.; White, B. E.; Tobin, P. J. *J. Vac. Sci. Technol., B* **2004**, *22*, 2121–2127.

(35) Robertson, J. *J. Vac. Sci. Technol., B* **2000**, *18*, 1785-1791.

(36) Lee, J. S.; Chang, S. J.; Chen, J. F.; Sun, S. C.; Liu, C. H.; Liaw, U. H. *Mater. Chem. Phys.* **2002**, *77*, 242–247.

(37) Lau, W. S.; Khaw, K. K.; Han, T.; Sandler, N. P. *Appl. Phys. Lett.* **2006**, *89*, 262901/1–262901/3.

(38) Yamamoto, Y.; Kita, K.; Kyuno, K.; Toriumi, A. *Appl. Phys. Lett.* **2006**, *89*, 032903/1–032903/3.

(39) Zhang, M. H.; Rhee, S. J.; Kang, C. Y.; Choi, C. H.; Akbar, M. S.; Krishnan, S. A.; Lee, T.; Ok, I. J.; Zhu, F.; Kim, H. S.; Lee, J. C. *Appl. Phys. Lett.* **2005**, *87*, 232901/1–232901/3.

(40) Lee, D.; Suh, D.; Pae, Y.; Kim, H.; Cho, M.; Ko, D. *J. Electrochem. Soc.* **2007**, *154*, H708–H712.

(41) Inoue, H.; Utsuno, F.; Yasui, I. *Journal of Non-Crystalline Solids*. **2004**, *349*, 16–21.

(42) Toriumi, A.; Kita, K. In *Dielectric Films for Advanced Microelectronics*; Baklanov, M.; Green, M.; Maex, K. ; John Wiley & Sons: Hoboken, NJ, 2007; p. 297–336.

(43) Lucovsky, G.; Whitten, J. L. In *High Dielectric Constant Materials: VLSE MOSFET Applications*; Huff, H. R.; Gilmer, D. C. ; Springer: New York, 2005; p. 311–358.

(44) Lee, C.; Cho, E.; Lee, H.; Hwang, C. S.; Han, S. *Phys. Rev. B*. **2008**, *78*, 012102/1–012102/4.

(45) Wang, T.; Ekerdt, J. G. *Chem. Mater.* **2009**, *21*, 3096–3101.

(46) Huang, L.; Li, A.; Zhang, W.; Li, H.; Xia, Y.; Wu, D. *Appl. Surf. Sci.* **2010**, *256*, 2496–2499.

(47) Majumder, P.; Jursich, G.; Takoudis, C. *J. Appl. Phys.* **2009**, *105*, 104106/15–104106/6.

(48) Yang, Z. K.; Lee, W. C.; Lee, Y. J.; Chang, P.; Huang, M. L.; Hong, M.; Yu, K. L.; Tang, M.; Lin, B.; Hsu, C.; Kwo, J. *Appl. Phys. Lett.* **2007**, *91*, 202909/1–202909/3.

(49) Cho, M.; Roh, Y. S.; Whang, C. N.; Jeong, K.; Nahm, S. W.; Ko, D.; Lee, J. H.; Lee, N. I.; Fujihara, K. *J. Appl. Phys.* **2002**, *81*, 472–474.

(50) Navrotsky, A. *J. Mater. Chem.* **2005**, *15*, 1883–1890.

Chapter 2: Atomic Layer Deposition of Lanthanum Stabilized Amorphous Hafnium Oxide Thin Films

2.1. INTRODUCTION

As the microelectronic industry transitions from conventional SiO_2 to high-k materials to avoid excessive gate leakage current in the gate dielectric, hafnium dioxide (HfO_2) has attracted considerable attention.[1,2] It is desirable that the gate material remains amorphous throughout the necessary processing treatments because the grain boundaries in polycrystalline gate dielectrics may serve as high-leakage paths.[1] Some as-grown films can be amorphous,[3,4] but HfO_2 readily crystallizes upon annealing. Not only does HfO_2 require a post deposition 450 °C densification anneal,[5] there is a high-temperature dopant activation anneal at ~1000 °C,[6] resulting in polycrystalline films. The polymorphs have different dielectric constants, viz., tetragonal is ~70, cubic is ~29, and monoclinic is about ~16.[7] Different phases often coexist in polycrystalline films,[8] which leads to a spatially varying dielectric constant. Zhao and Vanderbilt have shown that the dielectric constant varies by as much as 50% between different phases,[7] resulting in devices with variable capacitance values among different regions. Therefore, although crystalline HfO_2 has a higher dielectric constant, it is desirable to find methods to stabilize its amorphous phase after annealing. The dielectric constant for amorphous HfO_2 varies from 13 to 20,[9,10] but we may expect that it is close to that for the lowest-energy monocrystaline crystalline phase.

To suppress crystallization, Al_2O_3 and SiO_2 have been incorporated into HfO_2.[11–13] Although $HfSiO_x$ and $HfAlO_x$ show higher crystallization temperatures than HfO_2, their dielectric constants decrease, reducing the advantage of the high-k film. Another choice is La_2O_3, which is also a high-k material, with a dielectric constant of more than

20.[14,15] Incorporating La into HfO_2 has been demonstrated as one method to stabilize an amorphous structure and one can expect this incorporation will not degrade the dielectric constant of the system because of the high-*k* nature of La_2O_3. Lanthana incorporation has been reported using RF cosputtering and aqueous solution precipitation for the purpose of amorphous stabilization.[16,17] It is also reported that crystalline $La_2Hf_2O_7$ can be epitaxially grown on Si(001) by molecular beam epitaxy (MBE),[18] and pulsed laser deposition (LPD).[19] To the best of my knowledge, there is no report on the hafnium-lanthanum system deposited by atomic layer deposition (ALD).

ALD is based on sequential, self-terminating surface reactions, which ensure atomic-level thickness control as the film grows linearly with the number of ALD cycles.[20] At present, ALD is one of the established techniques to grow amorphous as-deposited HfO_2 and La_2O_3 films.[21–25] In this chapter, ALD is used to incorporate La in periodic HfO_2–$HfLa_xO_y$ structures, which are expected to be structurally different from sputtered homogeneous $HfLa_xO_y$ films and epitaxially grown $Hf_2La_2O_7$ or HfO_2–La_2O_3 bilayers.[26] ALD was first demonstrated in the 1970s.[27] The low growth rate for ALD is less of a problem for dielectric growth as ever thinner films are needed in complementary metal–oxide–semiconductor (CMOS) devices and has become an economically feasible method to grow highly conformal thin films for the semiconductor industry.

2.2. EXPERIMENTAL DETAILS

The ALD system consists of a custom built, hot wall stainless steel vessel that is connected to a surface analysis chamber. Substrate samples are 2 × 2 cm^2 and are mounted on a molybdenum stage that can be moved in situ between the ALD chamber and the analysis chamber. The ALD chamber is pumped by a turbomolecular pump to a base pressure of 5×10^{-6} Torr and is connected to an X-ray photoelectron spectroscopy

(XPS) analysis chamber through a load lock with a base pressure of 2×10^{-7} Torr. Films were deposited on n-Si(100) substrates at 250 °C using tetrakis (ethylmethylamino) hafnium $Hf[N(CH_3)(C_2H_5)]_4$, tris[*N*, *N*-bis(trimethylsilyl)-amino] lanthanum $La[N(SiMe_3)_2]_3$ and H_2O; the precursors were held at 85, 150, and 25 °C, respectively. The adsorption of $Hf[N(CH_3)(C_2H_5)]_4$ has been proved to be a self-limiting process at 250 °C.[21] The ALD of La_2O_3 using the same precursor is also reported at the same growth temperature,[23] although there might be a CVD component of the growth due to precursor decomposition.[28] To remove the native oxide from Si(100), we etched Si substrates in a 2% HF solution for 30 s, rinsed in deionized water for 20 s, which redeoxidized the Si(100) surface, and dried with flowing He. The resultant oxide is 10 Å according to spectroscopic ellipsometry (SE). All as-deposited samples were confirmed to be 11 nm (10 nm high-*k* film + 1 nm SiO_2) by SE.

The incorporation of La was achieved by depositing HfO_2 and La_2O_3 in different cycles, and the La level was controlled by varying the ALD cycle ratio of the two oxides. One cycle consists of precursor dosing for 1.5 s, a 15 s purge with Ar, water dosing for 0.05 s, and a 25 s purge with Ar. The growth rate of HfO_2 and La_2O_3 in our ALD system is 0.78 Å/cycle and 0.50 Å/cycle, respectively. To deposit a film of a certain composition, we grow x cycles of HfO_2 plus one cycle of La_2O_3, and then repeat this sequence n times to achieve the desired thickness; films are referenced using $[x\mathrm{Hf} + 1\mathrm{La}] \times n$. Note an ALD layer does not imply a complete monolayer of a particular material, and we refer to an ALD layer as the amount deposited in a single cycle. Film growth always ends with an xHf cycle to minimize adsorption of ambient CO_2 and H_2O on the La_2O_3.[29,30] Due to the layer-by-layer growth nature of ALD, we expect the $[x\mathrm{Hf} + 1\mathrm{La}] \times n$ approach to lead to a periodic structure, with HfO_2 layers separated by $HfLa_xO_y$ layers.

X-ray photoelectron spectroscopy (XPS) with an Al *K*α source at 1486.6 eV was performed using a Physical Electronics 5500 XPS system to determine the film composition. A series of 10 nm films with different La-incorporation levels (metal basis defined as La/(Hf + La)) was deposited by changing the HfO_2:La_2O_3 ALD cycle ratio from 1:1 to 8:1. After growth at 250 °C, samples were cooled to 70 °C in the ALD chamber and were transferred to the XPS chamber through a load lock; the load lock is suspected of introducing some C contamination onto the sample surface since the load lock is repeatedly exposed to the ambient pressure when loading samples. Therefore, Ar^+ sputtering at 3 kV over a 3×3 mm^2 area for 90 s was performed to measure the atomic composition of the films. Approximately 3 nm is removed in this sputtering process.

To investigate the crystallinity of La-incorporated HfO_2 films, grazing incidence X-ray diffraction (GIXRD) was performed at a fixed 0.5° incident angle, and 2θ scan rate of 6°/min. XRD was conducted with a Bruker-AXS D8 Advance Powder Diffractometer using a sealed tube Cu *K*α radiation. Prior to XRD, samples were annealed by rapid thermal annealing at different temperatures for 30 s under a N_2 ambient.

Cross-sectional high resolution transmission electron microscopy (HRTEM) images were obtained to examine the morphology and microstructure of the HfO_2 films at different incorporation levels and different annealing temperatures. The cross sections were prepared using a dicing saw followed by focused ion beam (FIB) milling. The FIB milling was conducted with a FEI Strata DB235 dual beam SEM/FIB system, which combines a scanning electron microscope (SEM) with a Ga ion beam source for nanoscale cutting. The thinning process starts at a rough milling step under 3000 pA, followed by a fine milling step under 300 pA, and finally a cleaning cross-section milling step under 30 pA. TEM images were acquired using a JEOL 2010F high resolution transmission electron microscope with a field emission gun operated at 200 kV.

For preliminary electrical measurements concerning film dielectric constant, metal–insulator–semiconductor (MIS) capacitors were made by depositing TaN using DC sputtering. The area of TaN contact was defined by a shadow mask, and measured with a Zeiss Axioskop 2 MAT optical microscope. The capacitance–voltage (C–V) characteristics were measured using a Keithley 590 CV Analyzer controlled by a Keithley 4200 Semiconductor Characterization System

2.3 RESULTS AND DISCUSSION

2.3.1. Compositional Analysis

Figure 2.1 shows the X-ray photoelectron spectra for La 2p, Si 2s, and Hf 4f of the as-deposited films. As the La-incorporation level increases (smaller x in $[x\text{Hf} + 1\text{La}] \times n$), the La 2p peak intensity increases along with a corresponding decrease in the Hf 4f peak intensity, indicating La has been successfully incorporated into the films. The major impurity is Si from the La precursor, which is commonly observed in ALD grown La_2O_3 using the same precursor.[31] The Si 2s signal is shown instead of the more common Si 2p signal because the latter overlaps with the La 4d peak. The intensity of Si 2s increases simultaneously with increasing La-incorporation level. The peak positions for these three elements do not show any shifts with respect to different La-incorporation level. A very weak N 1s feature appears at 389 eV (not shown), which comes from the Hf precursor. No peak was found for C 1s at 285 eV (not shown) in the films, indicating any C impurities are below the XPS detection limits in the bulk film after sputtering off the topmost surface. The Hf $4f_{7/2}$ peak appears at 18.5 eV, indicating the formation of Hf–O bonding and the Hf^{4+} oxidation state in the bulk film.[32] The La $3d_{5/2}$ core level appears at 836.9 eV, consistent with La_2O_3 or La silicate.[33] The O 1s state appears at 532.1 eV for all La-incorporation levels (bottom inset of Figure 2.2). Considering that the O 1s state of HfO_2 films appears at 532 eV (not shown) in our XPS system, the incorporation of La does not affect the Hf–O bonding significantly.

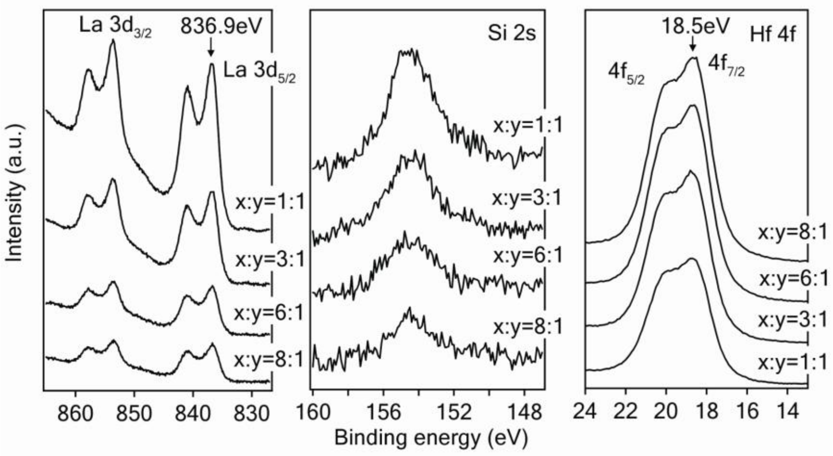

Figure 2.1. XP spectra of La 3d, Si 2p, and Hf 4f at different La-incorporation levels. The *x*:*y* designations refer to the HfO_2:La_2O_3 ALD cycle ratios.

The as-deposited film atomic composition is calculated from the integrated photoemission intensities corrected by their atomic sensitivity factors.[34] The Hf and La atomic concentrations are shown in the top inset of Figure 2.2 and the main plot presents the La-incorporation level on a Si-free metal basis. Figure 2.2 illustrates the La-incorporation level in HfO_2 can be well-controlled by varying the ALD growth cycles of the two oxides. The highest La-incorporation level of 43% was reached for one deposition cycle of HfO_2 followed by one cycle of La_2O_3, i.e., [1Hf + 1La]. At this nominal 50:50 condition, the film contains more Hf than La because the ligands on the La precursor are larger than on the Hf precursor, and the greater steric hindrance can reduce the number of precursor molecules absorbed with every La dosing cycle.

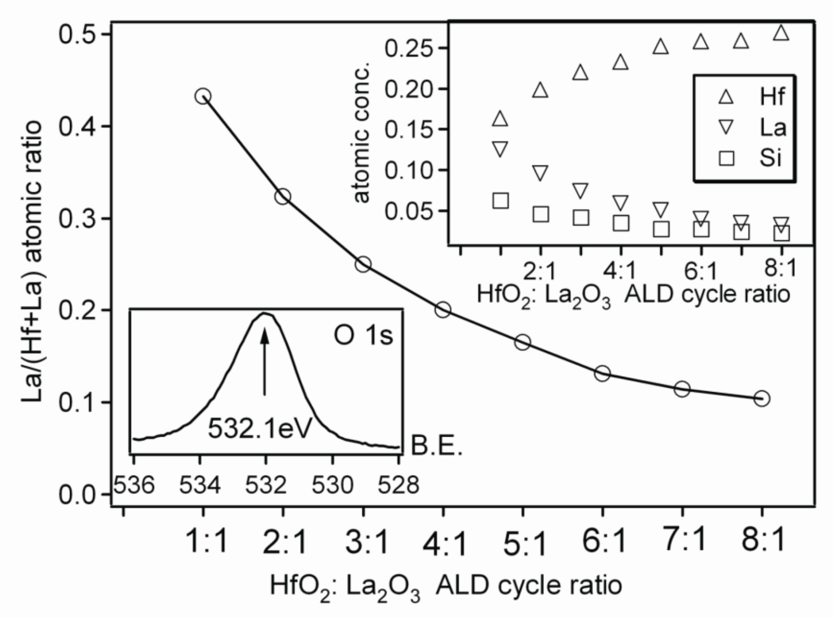

Figure 2.2. Hf, La, and Si atomic concentration (top inset) and La-incorporation level (metal based) as a function of HfO_2:La_2O_3 ALD cycle ratio; bottom inset, O 1s peak for all La-incorporation levels.

2.3.2. Crystallinity and Dielectric Constant

The XRD patterns in Figure 2.3 show that the temperature for the onset of crystallization increases as the La-incorporation level increases. Others have reported that 10 nm HfO_2 films crystallize at 500 °C,[4] and we obtained the same result, as shown in the inset of Figure 2.3. By adding one cycle of La_2O_3 after every 6 cycles of HfO_2 (La/(Hf + La) = 13%), the 10 nm thin film remains amorphous after 800 °C annealing. Increasing the La-incorporation level by depositing one cycle of La_2O_3 after every three cycles of HfO_2 (La/(Hf + La)=25%), enables the 10 nm amorphous film to withstand 900 °C annealing. When HfO_2:La_2O_3 = 1:1, a 10 nm amorphous film can withstand 950 °C annealing, but becomes crystallized after 1000 °C annealing. Because only two peaks are detected in the 10 nm films, it is difficult to distinguish between monoclinic and tetragonal phases. The peaks after crystallization occur at 2θ = 31 and 36°. These two peaks are closed to tetragonal (111) and tetragonal (002) as observed for HfO_2.[35] The calculated *d* spacing is 2.97 Å for t(111), and 2.62 Å for t(002).

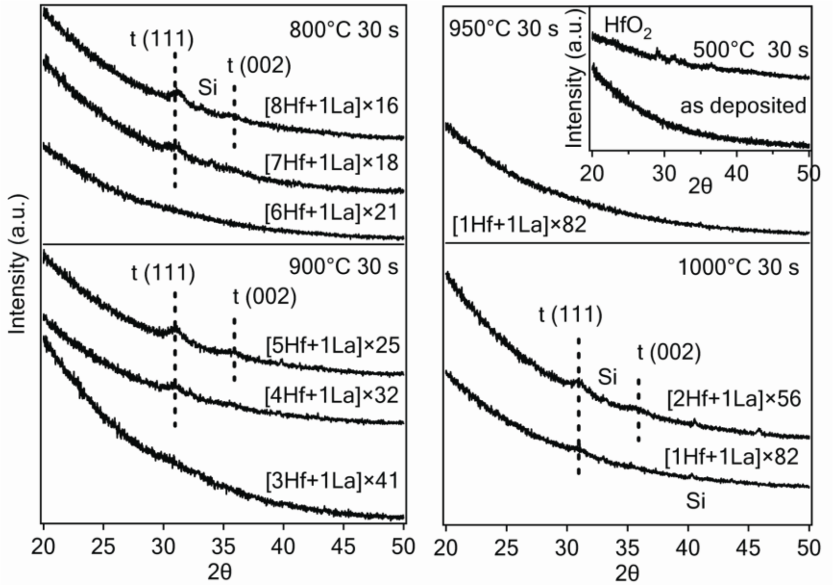

Figure 2.3. XRD spectra of 10 nm $HfLa_xO_y$ films after 30 s annealing in a N_2 ambient; inset, XRD spectra for 10 nm HfO_2.

The HRTEM images in Figure 2.4 show the representative samples at La-incorporation levels necessary to keep the films amorphous at 800 and 900 °C and just below those La-incorporation levels. The total oxide thickness (interfacial SiO_2 + $HfLa_xO_y$) is 11 nm for each sample, consistent with thicknesses predicted by SE. In terms of crystallinity, while a 10 nm [6Hf + 1La] film remains completely amorphous after 800 °C annealing, adding an extra HfO_2 layer leads to a partially crystallized film after annealing at the same temperature (Figure 2.4a). Similarly, a [4Hf + 1La] film changed into a polycrystalline film after annealing at 900 °C, but a [3Hf + 1La] film was still amorphous after annealing at 900 °C (Figure 2.4b). The random orientations of the lattice fringes in the crystallized samples (Figure 2.4) illustrate that the films were polycrystalline. The lattice spacing within the highlighted region is 2.87 Å for the [7Hf + 1La] film, and 2.97 Å for the [4Hf + 1La] film. These results are consistent with XRD results in Figure 3 where the *d* spacing for t(111) is 2.97 Å.

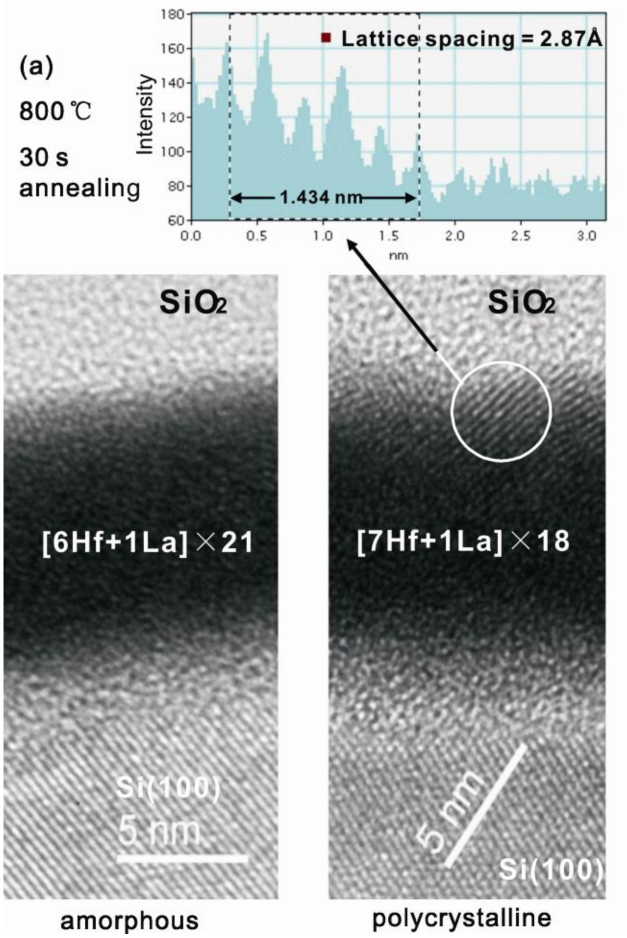

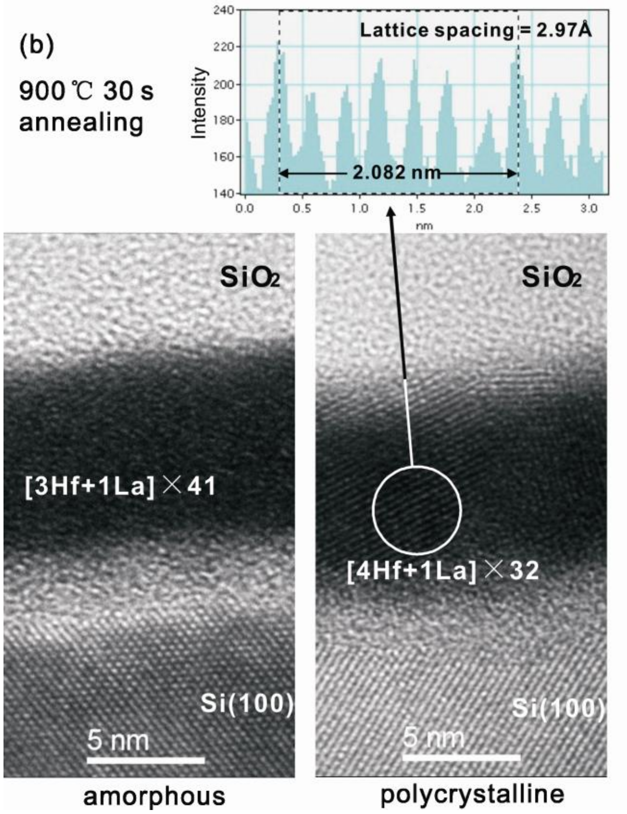

Figure 2.4. Cross-sectional HRTEM images for samples above and below the La-incorporation levels that stabilize an amorphous structure at (a) 800 and (b) 900 °C.

To measure the dielectric constant, MIS capacitors were made. The typical 100 kHz C–V measurements were performed for HfO_2 annealed at 500 °C and 13% La-incorporated [6Hf + 1La] × *n* films annealed at 800 °C. 500 and 800 °C were chosen because at these temperatures HfO_2 films became polycrystalline while [6Hf + 1La] films remained amorphous, which serves to illustrate the comparison between a polycrystalline gate dielectric and an amorphous dielectric that could form under annealing temperatures that mimic the real device fabrication process. The dielectric constant was determined from the slope of capacitance equivalent thickness (CET) versus physical thickness curves, where CET was measured at $V_g = -5$ V of the accumulation capacitance of the C–V curves and physical thickness was measured by SE. From linear fitting in Figure 2.5, HfO_2 films have a dielectric constant of 16.7 ± 0.3, and 13% La-incorporated [6Hf + 1La] × *n* films have a dielectric constant of 16.6 ± 0.4, indicating that La-incorporation will not degrade the film in terms of dielectric constant.

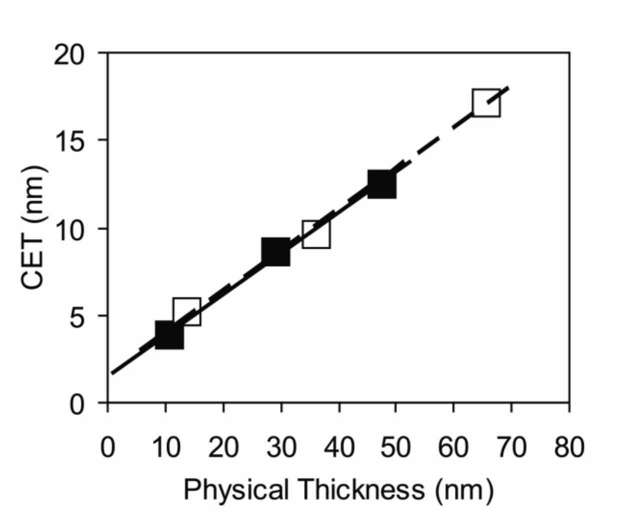

Figure 2.5. CET as a function of physical thickness (measured by SE). HfO_2 films (□) were annealed at 500 °C for 30 s, and [6Hf + 1La] films (■) were annealed at 800 °C for 30 s. The fits for HfO_2 (dash line) and [6Hf + 1La] (solid line) lead to k of 16.7 ± 0.3 and 16.6 ± 0.4, respectively.

2.3.3. Evidence of a Periodic Structure and Its Comparison to Homogeneous Films

Due to the ALD growth mechanism, we expect a periodic film structure composed of repeated $HfLa_xO_y$ layers separated by HfO_2 layers is formed. To verify the existence of periodicity, we performed angle-resolved XPS at small take off angles (angles between sample surface and photoelectron detector) to investigate the topmost overlayers of films. A smaller XPS take off angle means we are detecting photoelectrons from a shallower film overlayer. Figure 2.6 shows the in-situ La 3d and Hf 4f XPS spectra of an as-deposited 10nm [6Hf + 1La] × 21 sample at take off angles of 8, 9, and 10°. The unit of intensity is in counts per second (cps) so that the absolute values of the peak intensity can be compared. While the Hf peak gradually increases with increasing XPS take off angle, La peak abruptly show up at 10°. The absence of La peaks for take off angles smaller than 10° indicates the existence of a top La-free overlayer wholly composed of HfO_2, and an underlying $HfLa_xO_y$ layer corresponding to the La signal when the detection overlayer is deeper than a certain thickness. Therefore, we conclude the existence of a top HfO_2–$HfLa_xO_y$ structure, resulting from the last [6Hf + 1La] ALD sequence, which is different from a homogeneous HfO_2–La_2O_3 mixture. Although it is difficult to characterize the bulk film using the same technique, we believe this film is composed of 21 similar HfO_2–$HfLa_xO_y$ structures because of the layer-by-layer growth nature of ALD.

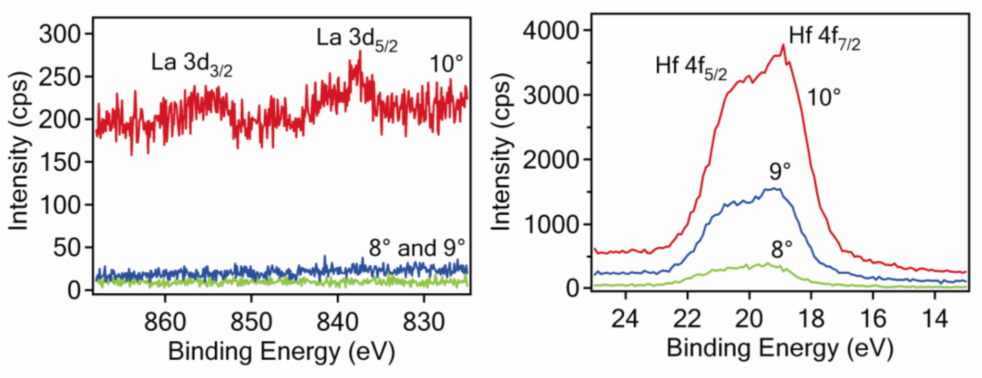

Figure 2.6. XP spectra of La 3d and Hf 4f spectra of a 10 nm [6Hf + 1La] × 21 sample at take off angle = 8, 9, and 10°.

Table 2.1 lists a comparison of the amorphous stabilization effects between 10 nm ALD periodic structure films in this study and 30 nm homogeneous films grown by RF cosputtering in Ref 16. Periodic structure films appear to require lower La-incorporation levels to stabilize the amorphous structure. Overall film thickness can be a contributing factor to amorphous film stabilization. To investigate the impact of overall film thickness in ALD-grown films,, we deposited four films (3, 10, 30, and 50 nm) at a constant 13% La-incorporation level, i.e., [6Hf + 1La]. As shown in Figure 2.7, all four films remained amorphous after 800 °C annealing, and only the ultrathin 3 nm film remained amorphous after annealing at 1000 °C. The Si atomic concentration for a [6Hf + 1La] film and a [3Hf + 1La] film in this study is 2.4 and 3.5%, respectively. The Si impurities may be an additional contributing factor in the stabilization of our films. However, in separate studies a Si incorporation level of 10% was unable to stabilize the amorphous phase after 800 °C annealing.[13]

Table 2.1. Comparison of lowest La-incorporation concentration (metal based) that ALD periodic structure and homogeneous films require to suppress crystallization after 800 and 900 °C annealing.

Annealing Temperate	ALD periodic structure films	homogenous films [16]
800 °C	13% ([6Hf + 1La] film)	20%
900 °C	25% ([3Hf + 1La] film)	40%

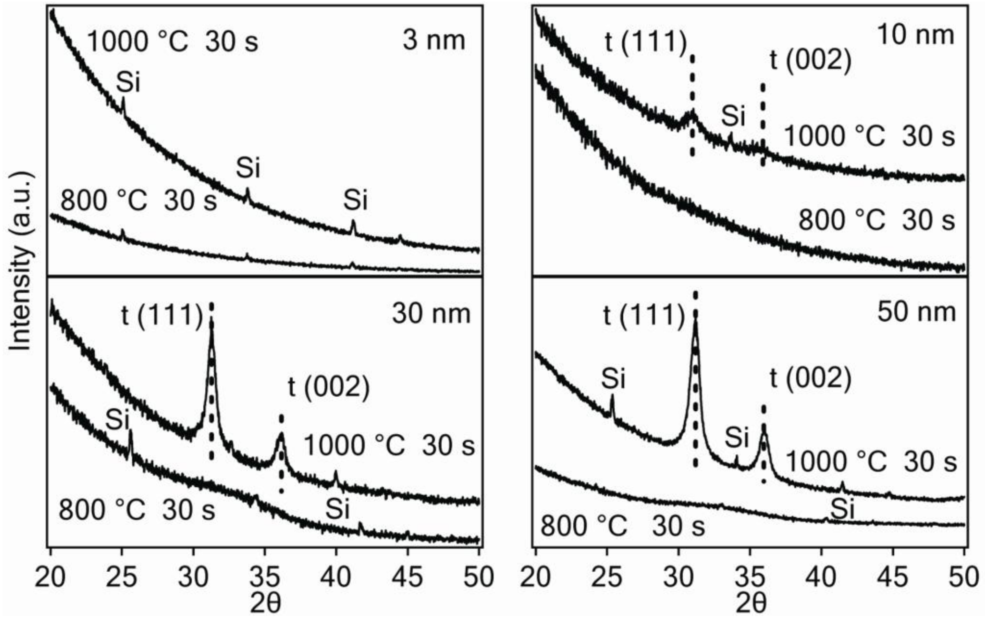

Figure 2.7. XRD spectra of [6Hf + 1La] films of different thickness (3, 10, 30, and 50 nm) after 800 and 1000 °C annealing under a N_2 ambient for 30 s.

The results reported herein illustrate how both the amount of La-incorporated and its location in the film affect its ability to stabilize the amorphous phase. A possible reason for this location effect might be the formation of the HfO_2–$HfLa_xO_y$ periodic structure formed by repeatedly adding one ALD layer of La_2O_3 on *n* layers of HfO_2. As temperature is elevated, HfO_2 between $HfLa_xO_y$ layers is expected to crystallize first while the $HfLa_xO_y$ layers would remain amorphous in the same way as homogeneous $HfLa_xO_y$ films with a high La-incorporation concentration remain amorphous. This interpretation is illustrated in the in Illustration 2.1. If crystals are nucleated within HfO_2, the film has to overcome an extra energy barrier, compared to pure homogenous HfO_2, due to the interfaces between crystallized HfO_2 and amorphous $HfLa_xO_y$ layers.

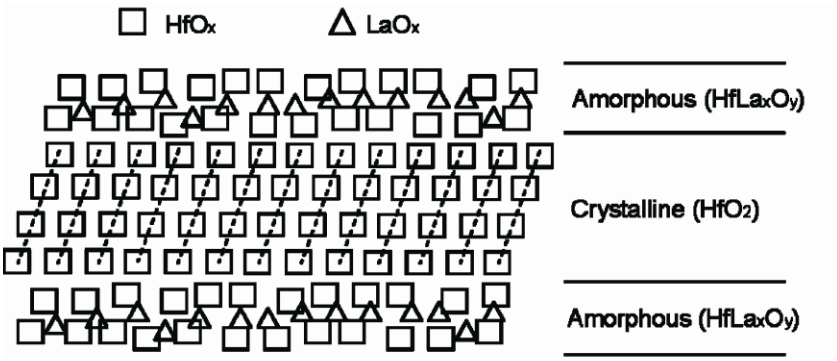

Illustration 2.1. Pictorial presentation of the periodic structure during the intermediate state of the crystallization process

Furthermore, we may expect that the crystallization onset temperature is essentially determined by the thickness of the HfO_2 region between the $HfLa_xO_y$ layers. In this amorphous stabilization model, a lower HfO_2:La_2O_3 ALD cycle ratio (smaller x in $[x\text{Hf} + 1\text{La}] \times n$) does not increase the local La atomic concentration in the $HfLa_xO_y$ layers, but does decrease the thickness of HfO_2 interval layers. The La atomic concentration in $HfLa_xO_y$ layer should remain constant and behave in the same way as homogenous $HfLa_xO_y$ films. The thinner HfO_2 interval layers themselves can withstand higher annealing temperature due to their higher surface-to-volume ratio because amorphous oxide is found to have the smallest surface enthalpy.[36] For thinner HfO_2 layers, the increase of surface enthalpy upon crystallization would be large enough to make the amorphous phase more stable even though the crystalline phase is more thermodynamically favored in bulk films. Therefore, the amorphous stabilization mechanism(s) for homogeneous and ALD periodic structure films can be very different, although both are enhanced by adding more La.

2.4. SUMMARY

In summary, La has been successfully incorporated into HfO_2 using ALD. XPS analysis shows that the La-incorporation level was effectively controlled by varying the HfO_2:La_2O_3 ALD cycle ratio. XRD and cross-sectional HRTEM show that the crystallization temperatures for La-incorporated HfO_2 films have been increased significantly. A 10 nm [6Hf + 1La] × 21 (La/(Hf + La) = 13%) film remains amorphous after 800 °C annealing, a 10 nm [3Hf + 1La] × 41 (La/(Hf + La) = 25%) film remains amorphous after 900 °C annealing, and a 10 nm [1Hf + 1La] × 82 (La/(Hf + La)= 43 %) film remains amorphous after 950 °C annealing. The film dielectric constant was not degraded after La-incorporation. The ALD grown films require a lower La-incorporation level to sustain a certain annealing temperature compared with homogeneous films, probably because a layered HfO_2–$HfLa_xO_y$ periodic structure is formed. Incorporating La into HfO_2 using ALD is a potential method to fabricate high-*k* dielectric gate materials for future CMOS devices.

2.5. REFERENCES

(1) Wilk, G. D.; Wallace, R. M.; Anthony, J. M. *J. Appl. Phys.* **2001,** *89*, 5243–5275.

(2) International Technology Roadmap for Semiconductors, see www.itrs.net.

(3) Chiou, Y.-K.; Chang, C. -H.; Wu, T. -B. *J. Mater. Res.* **2007,** *22*, 1899–1906.

(4) Gusev, E. P.; Cabral, C.; Copel, M.; D'Emic, C.; Gribelyuk, M. *Microelectron. Eng.* **2003**, *69*, 145–151.

(5) Triyoso, D.; Liu, R.; Roan, D.; Ramon, M.; Edwards, N. V.; Gregory, R.; Werho, D.; Kulik, J.; Tam, G.; Irwin, E.; Wang, X.-D.; La, L. B.; Hobbs, C.; Garcia, R.; Baker, J.; White, B. E., Jr.; Tobin, P. *J. Electrochem. Soc.* **2004**, *151*, F220–F227.

(6) Plummer, J. D.; Deal, M. D.; Griffin, P. B. *Silicon VLSI Technology: Fundamentals Practice and Modeling*. Prentice Hall, Upper Saddle River, NJ, **2000**.

(7) Zhao, X.; Vanderbilt, D. *Phys. Rev. B* **2002**, *65*, 233106/1–233106/4.

(8) Mommer, N.; Lee, T.; Gardner, J. A. *J. Mater. Res.* **2000**, *15*, 377–381.

(9) Conley, J. F., Jr.; Ono, Y.; Tweet, D. J.; Zhuang, W.; Solanki, R. *Mat. Res. Soc. Proc.* **2002**, *716*, 73–78.

(10) Kim, H.; Saraswat, K. C.; McIntyre, P. C. *J. Mater. Res.* **2005**, *20*, 3125–3132.

(11) Jones, A. C.; Aspinall, H. C.; Chalker, P. R.; Potter, R. J.; Manning, T. D.; Loo, Y. F.; O'Kane, R.; Gaskell, J. M.; Smith, L. M. *Chem. Vap. Deposition* **2006**, *12*, 83–89.

(12) Wilk, G. D.; Wallace, R. M.; Anthony, J. M. *J. Appl. Phys.* **2000**, *87*, 484–492.

(13) Tomida, K.; Kita, K.; Toriumi, A. *Appl. Phys. Lett.* **2006**, *89*, 142902/1–142902/3.

(14) Guha, S.; Cartier, E.; Gribelyuk, M. A.; Bojarczuk, N. A.; Copel, M. C. *Appl. Phys. Lett.* **2000**, *77*, 2710–2712.

(15) Yeo, Y.-C. King, T.-J.; Hu, C. *Appl. Phys. Lett.* **2002**, *81*, 2091-2093.

(16) Yamamoto, Y.; Kita, K.; Kyuno, K.; Toriumi, A. *Appl. Phys. Lett.* **2006**, *89*, 032903/1–032903/3.

(17) Ushakov, S. V.; Brown, C. E.; Navrotsky, A. *J. Mater. Res.* **2004**, *19*, 693–696.

(18) Dimoulas, A.; Vellianitis, G.; Mavrou, G.; Apostolopoulos, G.; Travlos, A.; Wiemer, C.; Fanciulli, M.; Rittersma, Z. M. *Appl. Phys. Lett*. **2004**, *85*, 3205–3207.

(19) Wei, F.; Tu, H.; Wang, Y.; Yue, S.; Du, J. *Appl. Phys. Lett*. **2008**, *92*, 012901/1–012901/3.

(20) Suntola, T. *Thin Solid Films* **1992**, *216*, 84–89.

(21) Kukli, K.; Ritala, M.; Sajavaara, T.; Keinonen, J.; Leskela, M. *Chem. Vap. Deposition* **2002**, *8*, 199–204.

(22) Hausmann, D. M.; Kim, E.; Becker, J.; Gordon, R. G. *Chem. Mater*. 2002, 14, 4350–4358.

(23) He, W.; Schuetz, S.; Solanki, R.; Belot, J.; McAndrew, *J. Electrochem. Solid-State Lett.* **2004**, *7*, G131–G133.

(24) Triyoso, D. H.; Hegde, R. I.; Grant, J.; Fejes, P.; Liu, R.; Roan, D.; Ramon, M.; Werho, D.; Rai, R.; La, L. B.; Baker, J.; Garza, C.; Guenther, T.; White, B. E., Jr.; Tobin, P. J. *J. Vac. Sci. Technol.*, *B* **2004**, *22*, 2121–2127.

(25) Kukli, K.; Ritala, M.; Pore, V.; Leskela, M.; Sajavaara, T.; Hegde, R. I.; Gilmer, D. C.; Tobin, P. J.; Jones, A. C.; Aspinall, H. C., *Chem. Vap. Deposition* **2006**, *12*, 158–164.

(26) Mavrou, G.; Galata, S.; Tsipas, P.; Sotiropoulos, A.; Panayiotatos, Y.; Dimoulas, A.; Evangelou, E. K.; Seo, J. W.; Dieker, Ch. *J. Appl. Phys*. **2008**, *103*, 014506/1–014506/9.

(27) Suntola, T.; Antson, A. US Pat. 4058430 (1977).

(28) Jones, A. C.; Aspinall, H. C.; Chalker, P. R.; Potter, R. J.; Kukli, K.; Rahtu, A.; Ritala, M.; Leskelae, M. *Mater. Sci. Eng.*, *B* **2005**, *118*, 97–104

(29) Suzuki, M.; Kagawa, M.; Syono, Y.; Hirai, T. *J. Cryst. Growth.* **1991**, *112*, 621–627.

(30) De Asha, A. M.; Critchley, J. T. S.; Nix, R. M. *Surf. Sci*. **1998**, *405*, 201–214.

(31) Triyoso, D. H.; Hegde, R. I.; Grant, J. M.; Schaeffer, J. K.; Roan, D.; White, B. E., Jr.; Tobin, P. J. *J. Vac. Sci. Technol. B* **2005,** *23*, 288–297.

(32) Lay, T. S.; Chang, S. C.; Din, G. J.; Yeh, C. C.; Hung, W. H.; Lee, W. G.; Kwo, J.; Hong, M. *J. Vac. Sci. Technol. B* **2005**, *23*, 1291–1293.

(33) Copel, M.; Cartier, E.; Ross, F. M., *Appl. Phys. Lett.* **2001**, *78*, 1607–1609.

(34) Moulder, J. F.; Stickle, W. F.; Sobol, P. E.; Bomben, K. D. *Handbook of X-ray Photoelectron Spectroscopy*; Physical Electronics, Inc.: Eden Prairie, MN, 1995.

(35) Powder Diffraction File PDF 08–0342; International Center for Diffraction Data: Newtown Square, PA, **2001**.

(36) Navrotsky, A. *J. Mater. Chem.* **2005**, *15*, 1883–1890.

Chapter 3: Subnanoscale Lanthanum Distribution in Lanthanum-Incorporated Hafnium Oxide Thin Films Grown Using Atomic Layer Deposition

3.1 INTRODUCTION

Atomic layer deposition (ALD) is a chemical vapor deposition technique based on self-terminating surface reactions, leading to highly controlled layer-by-layer growth of thin films at the atomic level.[1] In recent years, ALD has become a well-established technique to grow various inorganic thin film materials, including oxides, nitrides, sulphides, selenides, tellurides, pure elements, etc.[2] Because of the unique growth mechanism, ALD grown films can be extremely conformal. Because the precursors are separately supplied to the growth chamber, precursors with high reactivity can be used, enabling relatively low growth temperatures compared with other chemical film deposition techniques.

Incorporating another element is considered as one of the effective ways to modify the properties of a material, such as conductivity, dielectric constant, and crystallization temperature. In terms of ALD grown films, the incorporation can be achieved by repeatedly depositing two materials in alternating cycles, i.e., x ALD layers of the host material followed by one ALD layer of the incorporated material, which defines the incorporation level, and then repeating this sequence to achieve the desired film thickness. For example, Er has been incorporated into Y_2O_3 for optical applications.[3,4] In the field of high-k dielectrics, amorphizers and crystallizers have been added to HfO_2 to change material properties.[5] Specifically, Si, Al, and La have been incorporated into HfO_2 for the purpose of amorphous stabilization,[6–11] and Y has been incorporated to induce the cubic phase.[12]

However, the spatial distribution of the incorporated layer(s) in many ALD-grown systems remains unclear. Unlike homogeneous ternary systems grown by physical vapor deposition (PVD) or chemical vapor deposition (CVD), the incorporated material is more likely to be separated by the host material in an ALD film, thereby forming a layered periodic structure, especially when the ALD cycle ratio of the host material to the incorporated material is high. We have proposed that the existence of this periodic structure may add an extra advantage to stabilize the amorphous phase of high-*k* dielectric thin films after high temperature annealing.[10] For ALD-grown $HfAlO_x$, the films with similar composition but different structure have different crystallization behavior; films deposited by alternating Hf and Al cycles in a 2:1 ratio are found to have a lower degree of crystallization than films deposited by alternating layers in a 4:2 ALD cycle ratio, even though the ratios of Hf and Al are the same.[13] The separation distance between Er ions in Y_2O_3 is also a critical parameter to fabricate high-performance fiber amplifiers.[14,15] In these cases, the ALD-grown ternary system is neither a nanolaminate with clear layer interfaces nor a homogeneous mixture. Further, the distribution of the incorporated material is a critical factor determining the film property. Therefore, it is important to understand how the incorporated material is intermixed with the host.

In this chapter, we use the La-HfO_2 system to study how the two materials might be intermixed. HfO_2 is one of the most promising high-*k* dielectric materials to replace conventional SiO_2 as its physical limit (2 nm) has been reached.[16] But there are some issues remaining to be solved. One of them is HfO_2 crystallizes after annealing at a relatively low temperature (500 °C).[17] Although crystallized HfO_2 has a higher dielectric constant, stabilizing HfO_2 in its amorphous phase is more desirable, because the grain boundaries in the polycrystalline films serve as a charge leakage pathway and the coexistence of cubic, tetragonal, and monoclinic phases in the polymorphs results in different dielectric constants among different regions of the devices.[16,18,19]

Unlike nanolaminate or superlattice structures,[20,21] it is more difficult to characterize the periodicity of these ALD-grown films because the repeated structures can be extremely thin and the films are amorphous. The incorporation concentration has to achieve a certain level to alter the film property. With respect to ALD-grown La-incorporated HfO_2 films, the x value has to be 6 and 3 in order for a 10 nm film to remain amorphous after 800 and 900 °C annealing, respectively.[10] The growth rates of HfO_2 and La_2O_3 are 0.8 and 0.5 Å/cycle, respectively; for a film at a functionally reasonable incorporation level, one [xHf + 1La] sequence is thinner than 6 Å. Therefore any compositional variations will be averaged in normal 45° take off angle X-ray photoelectron spectroscopy (XPS) analysis, since the electron effective attenuation lengths of Hf 4f and La 3d photoelectrons excited by Al $K\alpha$ is calculated to be 26.7 and 16.6 Å, respectively, at a 45° take off angle.[22] Cross sectional transmission electron microscopy, using the instrument at our disposal, a JEOL 2010F, is also unable to characterize such a small periodically distributed difference.

Angle-resolved X-ray photoelectron spectroscopy (AR-XPS) has been shown to be a powerful nondestructive tool to determine the thickness, fractional coverage and concentration depth profile for ultrathin films.[23–25] The XPS signal from the bulk material that is detected at the sample surface is given by

$$I = I_0 \exp(-d/\lambda \sin \theta) \qquad (1)$$

Lambda, λ, is the effective attenuation length (EAL),[22] and a more detailed discussion about EAL is reported elsewhere.[26,27] The angle (θ) between the analyzer and the sample surface is defined as the take off angle. At small take off angles, only photoelectrons from the near surface region are detectable.[25] Although the periodicity of ALD grown La-HfO_2 system is smaller than the EAL, at glancing take off angles, the abrupt presence of the first few $HfLa_xO_y$ layers is expected to be detectable by using the AR-XPS technique.

Ellipsometry is another nondestructive analytical method that can characterize both the microstructure and electronic structure of solids by measuring the change in polarized light upon light reflection from a sample.[28] The complex dielectric function is given by, $\varepsilon = \varepsilon_1 + i\varepsilon_2$, where ε_1 and ε_2 are the real and imaginary parts, respectively. For a thin film, the dispersion of its complex dielectric function, which can be determined from ellipsometry, is strongly connected to the film density.[29] In the process of our previous study (Chapter 2) concerning the amorphous stabilization phenomena of ALD-grown La-HfO_2 systems, we noticed that the thickness reduction for the films after annealing is correlated to the x value in the [xHf + 1La] sequences. Thus ellipsometry can be used as another technique to explore the relationship between HfO_2:La_2O_3 ALD cycle ratio and film structure.

3.2. EXPERIMENTAL DETAILS

3.2.1. Film Deposition

Samples were deposited on n-Si(100) substrates at 250 °C using tetrakis (ethylmethylamino) hafnium $Hf[N(CH_3)(C_2H_5)]_4$, tris[*N*,*N*-bis(trimethylsilyl)-amino] lanthanum $La[N(SiMe_3)_2]_3$ and H_2O; the precursors were held at 85, 150, and 25 °C, respectively. A detailed film deposition procedure is reported elsewhere.[10] The adsorption of $Hf[N(CH_3)(C_2H_5)]_4$ has been proved to be a self-limiting process at 250 °C.[30] The

ALD of La_2O_3 using the same precursor is also reported at the same growth temperature.[31] To remove the native oxide from Si(100), we etched the Si substrates in a 2% HF solution for 30 s, rinsed them in deionized water for 20 s, and then dried them with flowing He. One cycle consists of precursor dosing for 1.5 s, a 15 s purge with Ar, water dosing for 0.05 s, and a 25 s purge with Ar. The ALD system consists of a custom built, hot wall stainless steel vessel that is connected to an XPS chamber. Substrate samples are 2×2 cm^2 and are mounted on a molybdenum stage that can be moved in situ between the ALD chamber and the analysis chamber. The ALD chamber is pumped by a turbomolecular pump to a base pressure of 5×10^{-6} Torr and is connected to the XPS analysis chamber through a load lock with a base pressure of 2×10^{-7} Torr. The growth rate of HfO_2 and La_2O_3 in our ALD system is 0.8 and 0.5 Å/cycle, respectively. The La-incorporation is achieved by growing HfO_2 and La_2O_3 alternately; x cycles of HfO_2 are grown plus one cycle of La_2O_3, and then this sequence is repeated n times to achieve the desired thickness. Films are referenced using $[x\text{Hf} + 1\text{La}] \times n$. Film growth always ends with an xHf cycle to minimize adsorption of ambient CO_2 and H_2O on the La_2O_3.[32,33] All films are confirmed to be 10 ± 0.4 nm by ellipsometry. Note an ALD layer does not imply a complete monolayer of a particular material, and we refer to an ALD layer as the amount deposited in a single ALD cycle.

3.2.2. Cross-Sectional Transmission Electron Microscopy (TEM) and Atomic Force Microscopy (AFM)

TEM images for two as-deposited samples with high and low La-incorporation levels were acquired using a JEOL 2010F high-resolution transmission electron microscope with a field emission gun operated at 200 kV. The cross sections were prepared using a dicing saw followed by focused ion beam (FIB) milling. The FIB milling was conducted with a FEI Strata DB235 dual beam SEM/FIB system, which combines a scanning electron microscope (SEM) with a Ga ion beam source for nanoscale cutting. The AFM images of selected samples are acquired using a Veeco Dimension 3100 Scanning Probe Microscope operated at tapping mode, 1μm^2 scan size and 0.5 Hz scan rate.

3.2.3. X-ray Photoelectron Spectroscopy (XPS)

XPS is conducted using a Physical Electronics 5500 XPS system with a Mg *K*α source at 1253.6 eV and a Al *K*α source at 1486.6 eV. The base pressure of the XPS chamber is 1×10^{-9} Torr. The angle between the X-ray source and the photoelectron analyzer is 54.7°. The normal take off angle (between the analyzer and the sample surface) is 45°, at which XPS is normally performed using the Al source to acquire the averaged overall atomic percentage of Hf, La, and Si. AR-XPS is achieved by tilting the sample in a set of planes perpendicular to the plane defined by the X-ray source and the analyzer. The sample position has been calibrated so that the tilt axis crosses the intersection point of the X-ray and the analyzer. La 3d, Hf 4f, and O 1s photoelectrons are recorded in AR-XPS experiments. O 1s, instead of Hf 4f, is used as the reference for La 3d because the ratio of (La 3d)/(Hf 4f) varies too much with different take off angles, diminishing the features that can be observed at near-grazing take off angles. All XPS measurements are conducted in situ for as-deposited samples.

3.2.4. Ellipsometry

Ellipsometry is conducted using a J. A. Woollam M2000 Spectroscopic Ellipsometer. The ellipsometric data are interpreted using a Cauchy model and an effective medium approximation (EMA) model. The measurements are performed at 1.24−6.5 eV. Cauchy model fitting is limited to 1.24−3.3, 1.24−3.3, and 1.24−3.5 eV for HfO_2, $[x\mathrm{Hf} + 1\mathrm{La}] \times n$, and La_2O_3 films, respectively. The Cauchy model is used to establish film thickness for as-deposited and annealed films. The EMA model is used to interpret changes in the complex dielectric function as HfO_2, La_2O_3 and voids are combined in as-deposited films. In applying the EMA model, the solid component is modeled as a separate EMA material, composed of HfO_2 and La_2O_3 (with Si impurities) with known parameters, i.e., volume fraction and complex dielectric function. The complex dielectric function ($\varepsilon = \varepsilon_1 + i\varepsilon_2$) of 100 nm thick HfO_2 and La_2O_3 (with Si impurities) is measured to describe optical properties of the two constituents in the solid using the point-by-point data inversion method available in the J. A. Woollam software package. The EMA model describing the whole film is modeled by fitting the void fraction and the film thickness at 1.24−5.3 eV. The quality of the fit was assessed by evaluation of the mean-squared error (MSE) function:

$$\mathrm{MSE} = \frac{1}{2N - M} \times \sum_{i=1}^{N} \left[\left(\frac{\psi_i^{\mathrm{mod}} - \psi_i^{\mathrm{exp}}}{\sigma_{\psi,i}^{\mathrm{exp}}} \right)^2 + \left(\frac{\Delta_i^{\mathrm{mod}} - \Delta_i^{\mathrm{exp}}}{\sigma_{\Delta,i}^{\mathrm{exp}}} \right)^2 \right] \tag{2}$$

where N represents the number of (Ψ, Δ) experimental pairs, M is the number of variable parameters in the model, and σ are the standard deviations on the experimental data points. The resultant MSE values from the Cauchy model are < 2. The MSE values for the EMA model are presented in Section 3.3.2.

3.3. RESULTS AND DISCUSSION

In this work, the films are composed of three components, HfO_2, La_2O_3, and SiO_x impurities; Si impurities come from the trimethylsilyl-amino ligands on the La precursor. A periodic structure with repeated HfO_2 separated by La-rich layers is expected due to the ALD layer-by-layer growth process. But the cross-sectional TEM images of two 10 nm samples with high and low La-incorporation levels, [3Hf + 1La] × 41 (Figure 3.1a) and [9Hf + 1La] × 14 (Figure 3.1b), do not show any contrast variation. Both films appear homogeneous with an amorphous structure. This is because the thickness for a [9Hf + 1La] sequence is extremely thin (<1 nm) and one ALD La_2O_3 layer does not form a complete monolayer. Electron energy loss spectroscopy (EELS) mapping also does not work because both Hf and La are heavy atoms and the beam size for our system is 1 nm. Similarly, the atomic concentrations of Hf and La do not vary with increasing sputtering time in XPS depth-profiling analysis since the EALs of Hf 4f and La 3d photoelectrons are longer than the thickness of the repeated structures.

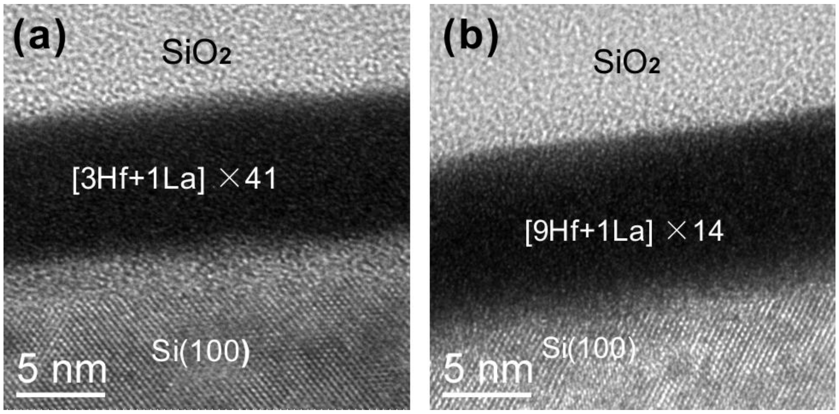

Figure 3.1. Cross-sectional TEM images for two as-deposited samples at (a) high La-incorporation level, [3Hf + 1La] × 41; and (b) low La-incorporation level, [9Hf + 1La] × 14. Both samples are homogeneous in TEM.

To overcome the difficulties in direct analysis methods such as TEM and normal XPS depth-profiling, we used AR-XPS and ellipsometry to reveal the existence of periodic structures. In situ AR-XPS measures the La 3d, Hf 4f, and O 1s signal at different take off angles, which define the sampling depth. The (La 3d)/(O 1s) and (Hf 4f)/(O 1s) signal intensity ratios are expected to vary depending on the sampling depth.

Through AR-XPS analysis, a unique feature associated with $HfLa_xO_y$ layers separated by HfO_2 layers in the near surface region of the films is developed at grazing take off angles for films with real periodic structures. The take off angles marking these features can be used to calculate the relative intermixing degree of the two metal ions. Through ellipsometry analysis, the structural difference of as-deposited [xHf + 1La] films with different x values is characterized by using a model assuming the film is composed of solids and voids. The void fraction shows an abrupt decrease when the number of Hf cycles is $x = 3$, which further illustrates a $HfLa_xO_y$–HfO_2–$HfLa_xO_y$ structure and it takes a finite number of Hf cycles to recover deposition of HfO_2.

3.3.1. Angle-Resolved XPS

The EAL is kinetic-energy-dependent,[34] therefore the Mg $K\alpha$ source at 1253.6 eV, instead of the Al $K\alpha$ source, is used in AR-XPS analysis to reduce the EAL and probe a thinner region near the free sample surface. A 10 nm as-deposited [4Hf + 1La] × 32 sample is used to illustrate the approach. Intense La 3d and Hf 4f peaks are found at the normal detection geometry ($\theta = 45°$) in panels a and b in Figure 3.2, respectively. The unit of intensity is in counts per second (cps) so that the absolute values of the peak intensity can be compared between Hf 4f and La 3d signals at the same take off angles. As the take off angle decreases, the Hf 4f peak intensity decreases because less of the total film is sampled, but the Hf 4f signal is always detectable (Figure 3.2c) because the film is capped with 4 Hf cycles after the final La cycle. Meanwhile, the La 3d signal completely disappears at $\theta = 2°$ (Figure 3.2d), which means at a sampling depth corresponding to $\theta = 2°$ the film is composed wholly of HfO_2. At $\theta = 3°$ (or 4°), the La 3d peak starts to appear as the sampling depth is large enough to reach the first $HfLa_xO_y$ layer.

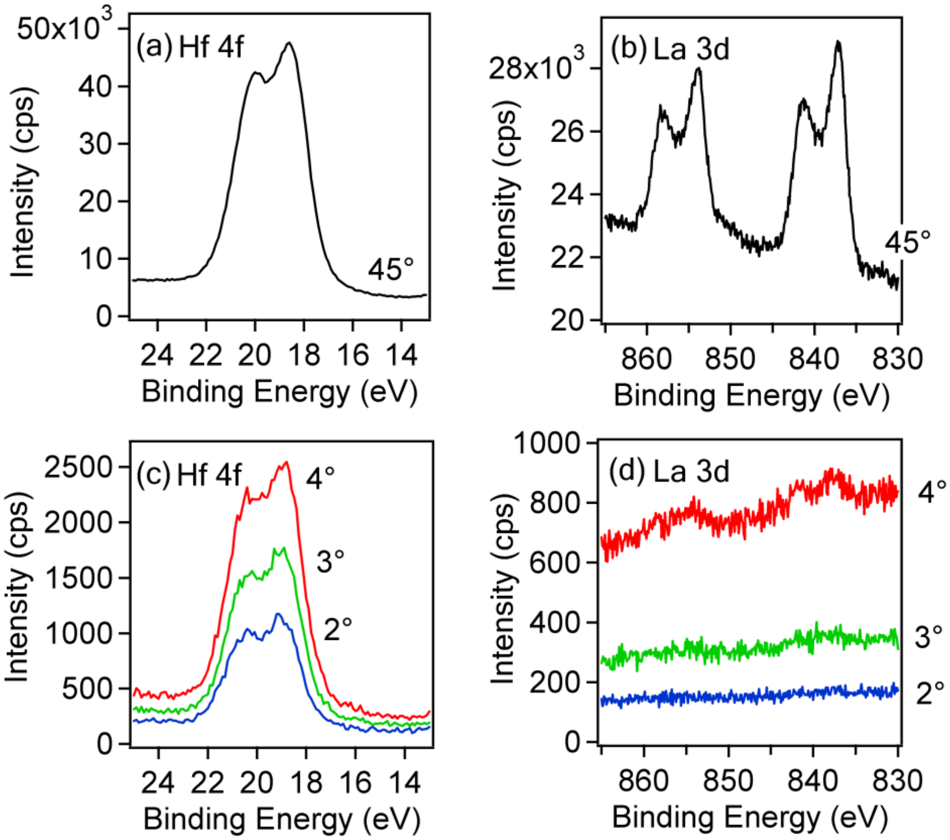

Figure 3.2. X-ray photoelectron spectra of Hf 4f and La 3d of a 10 nm as-deposited [4Hf + 1La] × 32 sample at (a, b)normal 45° take off angle; and at (c, d) near-grazing take off angles.

As the take off angle is gradually increased from near grazing to 45°, the periodicity of a [4Hf + 1La] film will become explicit as EAL × sin θ encounters the first few HfLa$_x$O$_y$ layers. Figure 3.3 shows the (La 3d)/(O 1s) photoelectron intensity ratio of a 10 nm as-deposited [4Hf + 1La] × 32 sample. The curve can be divided into four sections corresponding to different depths in the film. When the take off angle is larger than 2° and smaller than 14°, the (La 3d)/(O 1s) ratio increases rapidly with increasing take off angle, because 2° < θ < 14° corresponds to a sampling depth range that fully includes the first HfO_2 layer from the top and gradually includes the first $HfLa_xO_y$ layer. Within the $2° < \theta < 14°$ range of angles, more and more La from the first $HfLa_xO_y$ layer is sampled, while the O being sampled remains relatively constant since both HfO_2 and La_2O_3 contain O atoms. When the take off angle is increased from 14° to 18° ($14° \leq \theta \leq 18°$), the curve decreases slowly, because the sampling depth includes the entire first HfO_2 and $HfLa_xO_y$ layers, and gradually includes the second HfO_2 layer from the top. Before detecting the second $HfLa_xO_y$ layer, the amount of La being sampled remains constant while more and more O from the second HfO_2 layer is sampled. For take off angles between 18 and 25° ($18° \leq \theta \leq 25°$), the sampling depth fully includes the first HfO_2 and $HfLa_xO_y$ layers and the second HfO_2 layer and starts to gradually include the second $HfLa_xO_y$ layer. The La from the second $HfLa_xO_y$ layer makes the (La 3d)/(O 1s) intensity ratio increase again, but this increase (and rate of increase) is not as big as that for $2° < \theta < 14°$ because La from the first $HfLa_xO_y$ layer is always being sampled. When the take off angle is beyond 25° ($\theta > 25°$), the sampling depth is too deep and the periodicity is averaged for our particular detector.

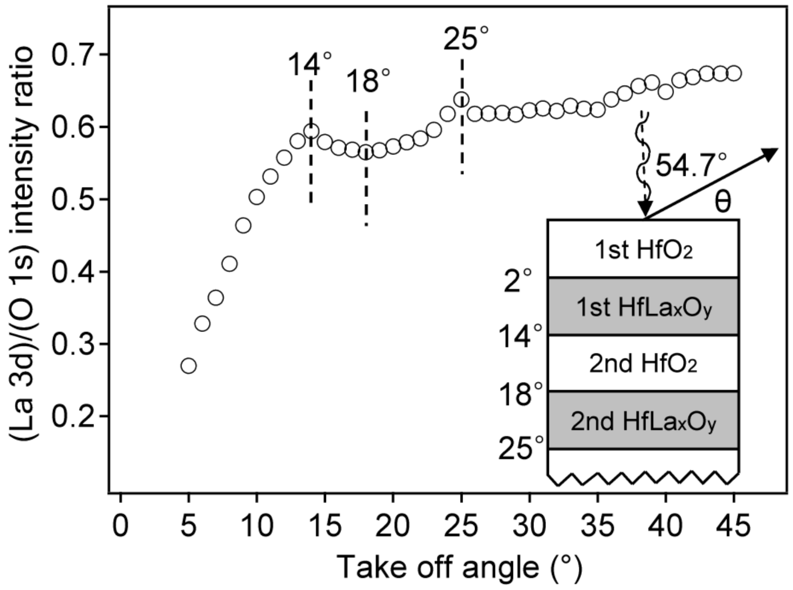

Figure 3.3. (La 3d)/(O 1s) photoelectron intensity ratio of a 10 nm as-deposited [4Hf + 1La] × 32 sample. $14° \leq \theta \leq 18°$ and $18° \leq \theta \leq 25°$ represent the second HfO_2 and $HfLa_xO_y$ layer from the sample surface, respectively.

Applying the same AR-XPS characterization method to a set of 10 nm [xHf + 1La] samples, where x = 2, 3, 4, 6, and 8, a parallel comparison is acquired, illustrating how La is distributed in the growth direction. For x = 2 and 3, only the emergence of the first $HfLa_xO_y$ layer can be observed (Figure 3.4a), ceasing at $\theta = 13°$. After that, the [2Hf + 1La] sample shows no periodicity under AR-XPS analysis, indicating a homogeneous film. The [3Hf + 1La] sample starts to show some variations, but compared with the noticeable feature of the [4Hf + 1La] sample in Figure 3.4b, the [3Hf + 1La] sample is more like a homogeneous film. All three films with lower La-incorporation levels (x = 4, 6, 8) show the same trends in Figure 3.4b, i.e., section I, the first $HfLa_xO_y$ layer emerging through the top (first) HfO_2 layer; section II, the second La-free HfO_2 layer; section III, the second $HfLa_xO_y$ layer; and section IV, the periodicity is averaged. Different sections show up at larger take off angles for films with a larger HfO_2:La_2O_3 ALD cycle ratio, which is caused by thicker La-free HfO_2 layers separating the $HfLa_xO_y$.

To check the reproducibility of this AR-XPS experiment, we conducted five measurements at seven different take off angles (10, 14, 15, 18, 20, 25, 30°) of the [4Hf + 1La] sample to acquire the standard deviation values, which are marked as the error bars at the corresponding data points in Figure 3.4b. As the La 3d signal noise-to-signal ratio is largely reduced at larger take off angles, the standard deviation values are small after 14° and the error bars at 14, 18, and 25° are much smaller than the maximum and minimum values defining the beginnings and endings of section II and III. Thus the existence of a periodic structure in ALD grown La-HfO_2 films is confirmed qualitatively by the features marked by section II and III in Figure 3.4b. For the [3Hf + 1La] sample (Figure 3.4a) to display periodicity, similar section II and III features should appear at 13−25° because any repeated La-free HfO_2 layer, if it exists, has to be thinner than in the [4Hf + 1La] sample. The standard deviations for the measured ratios were checked at 13, 19, and 25° and are shown in Figure 3.4a. The changes in the intensity ratios between 13 and 25° are too close to the standard deviations to permit assigning section II and III features, implying the [3Hf + 1La] sample is more like a homogeneous film. Thus x has to be larger than 3 for La-free HfO_2 interval layers to start forming since [4Hf + 1La] is the lowest HfO_2:La_2O_3 ALD cycle ratio for the feature marked by sections II and III in Figure 3.4b start to develop.

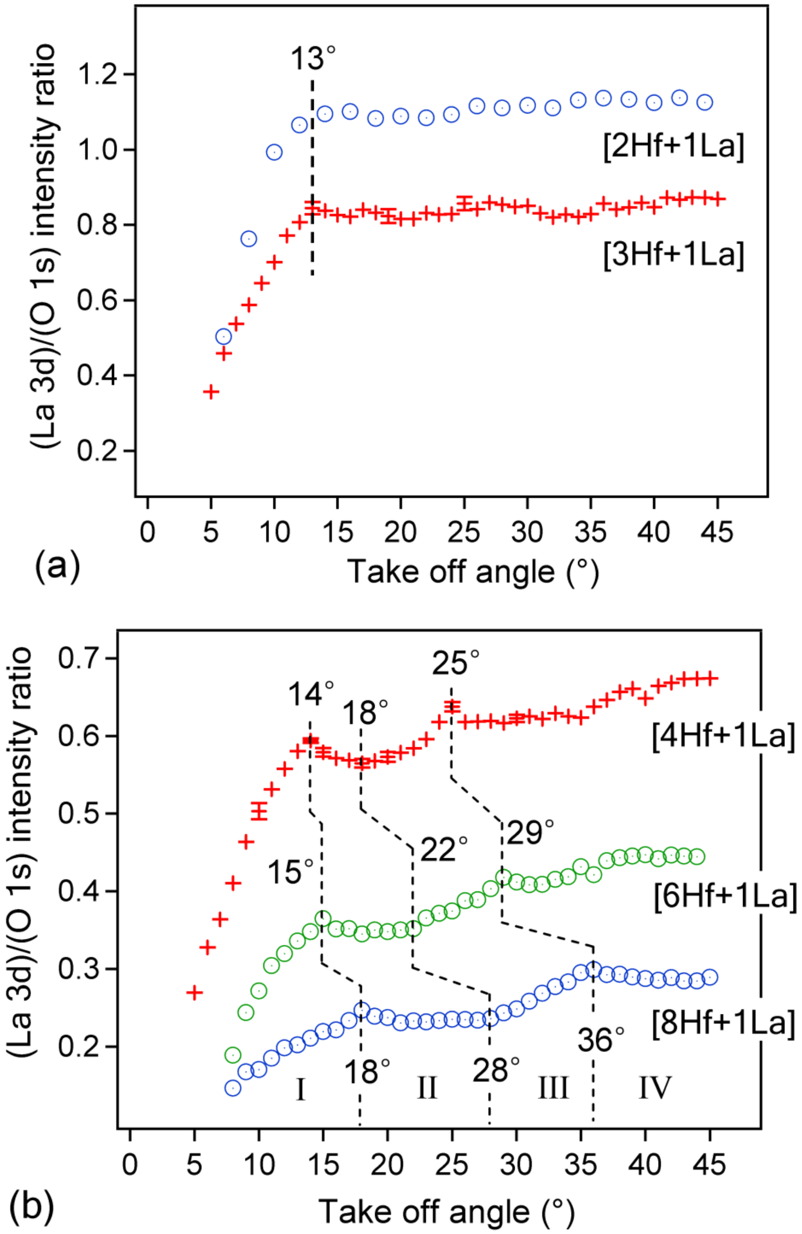

Figure 3.4. (La 3d)/(O 1s) photoelectron intensity ratio of a set of [xHf + 1La] samples. (a) When x = 2, 3, the films are more like homogeneous mixtures; (b) when x = 4, 6, 8, the existence of an $\mathrm{HfLa}_x\mathrm{O}_y$–$\mathrm{HfO}_2$–$\mathrm{HfLa}_x\mathrm{O}_y$ structure is confirmed by the features marked as sections I, II, and III.

To acquire a quantitative comparison among the three samples in Figure 3.4b, the National Institute of the Standards and Technology (NIST) database is used to calculate the practical EALs.[22] The product of the practical EAL and the sine of the take off angle equals to the depth normal to the surface from which a specific layer starts or ends, corresponding to a marked take off angle in Figure 3.4b. Sections II and III are the most informative part of the curves. Within section I, the take off angle is too small and the elastic scattering effect is not negligible so photoelectrons may escape from the surface by an additional path,[35] as shown in Illustration 3.1. The elastic scattering effect is pronounced for photoelectrons produced at deeper depths. This is another contributing factor for the initial (La 3d)/(O 1s) increase in section I. O 1s, with a smaller binding energy compared with La 3d, results in photoelectrons with a bigger kinetic energy, thus EAL(O 1s) > EAL(La 3d). Therefore the elastic scattering effect is more noticeable for O 1s at smaller take off angles, leading to more O detected from a deeper depth, which suppresses the (La 3d)/(O 1s) ratio at decreasing take off angles. The EAL depends on both take off angle and overlayer-film thickness, especially when the take off angle is near grazing,[22] so a set of practical EALs with different overlayer film thicknesses are calculated at different take off angles using the NIST database. A more reliable EAL can be determined by iterating and matching the value of EAL × sin θ and the overlayer film thickness at which the practical EAL is calculated. The final resultant EALs and their corresponding overlayer film thickness and EAL × sin θ at the three take off angles defining sections II and III are listed in Table 3.1 for the three samples.

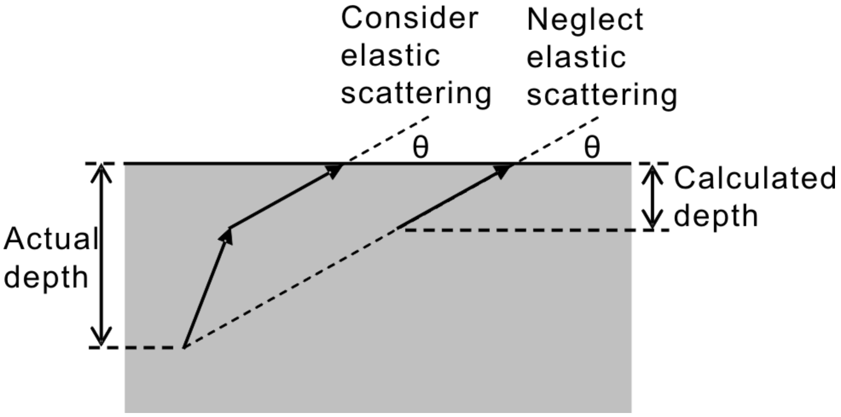

Illustration 3.1. Schematic illustration of elastic scattering at small take off angles. Photoelectrons from a deeper depth may make their way to the sample surface through a shortcut caused by elastic scattering.

Table 3.1. Calculated EALs at the three take off angles that define section II and III; overlayer film thickness at which the corresponding EALs are calculated.

	θ (deg)								
	[4Hf + 1La]			[6Hf + 1La]			[8Hf + 1La]		
	14	18	25	15	22	29	18	28	36
EAL(Å)	7.76	7.62	7.45	7.72	7.51	7.37	7.62	7.39	7.26
Overlayer film thickness (Å)	1.88	2.35	3.15	2.00	2.81	3.58	2.35	3.46	4.28
EAL × sin θ (Å)$^{\alpha}$	1.88	2.36	3.15	2.00	2.81	3.57	2.36	3.47	4.27

$^{\alpha}$value of EAL × sin θ represents the thickness from which the photoelectrons being detected come.

The three values for EAL × sin θ of each sample can be regarded as the depths at which the La 3d signal shows the local compositional variation that defines section II and III. Note that these depth values do not reflect the real thickness, since the take off angle in section II and III are still very small, where the elastic scattering effect as shown in Illustration 3.1 is not negligible. Elastic scattering contributes photoelectrons from deeper depths, which makes the calculated thicknesses smaller than what they should be. However, we still can use EAL × sin θ as a scale to predict the relative position of $HfLa_xO_y$ and La-free HfO_2 layers in the film.

For each sample, the differences of two adjacent EAL × sin θ values in Table 3.1 represent the second La-free HfO_2 layer and the second $HfLa_xO_y$ layer from the top, respectively, as shown in Illustration 3.2. The relative thickness of the second $HfLa_xO_y$ layer of all the three films is about 0.8 Å, indicating the vertical distance of La diffusion and/or dispersion is the same in all three samples. The calculated thickness of the second HfO_2 layer is about 0.5, 0.8, and 1.1 Å for the $x = 4$, 6, and 8, respectively. The relative thickness ratio of ($HfO_2/HfLa_xO_y$) is 0.61, 1.06, and 1.38 for [4Hf + 1La], [6Hf + 1La], and [8Hf + 1La], respectively.

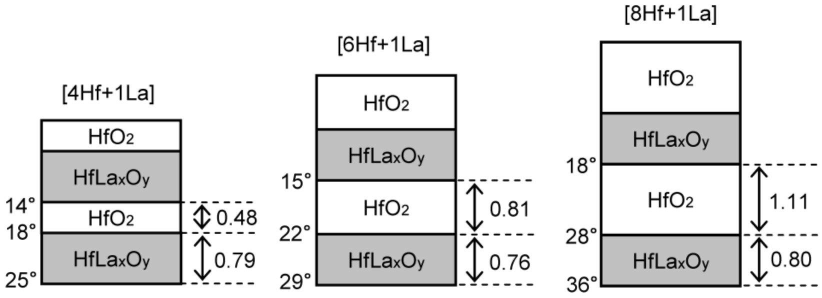

Illustration 3.2. Pictorial presentation of the $HfLa_xO_y$–HfO_2–$HfLa_xO_y$ structure in [4Hf + 1La], [6Hf + 1La], and [6Hf + 1La] films. The relative thickness is calculated from the EAL × sin θ values in Table 3.1.

From the ratios of the relative thicknesses of HfO_2 and $HfLa_xO_y$ for the three samples, we propose that one ALD layer of La_2O_3 interacts with more than two and less than three layers of HfO_2. The as-deposited film thickness measured by ellipsometry are

[4Hf + 1La] × 32 (or 128Hf + 32La) = 10.2 nm; [8Hf + 1La] × 15 (or 120Hf + 15La) = 10.0 nm; and 125 cycles of HfO_2 = 10.1 nm, indicating the thickness contributed by La_2O_3 is negligible compared to HfO_2 for films with large *x* values. For the 4 ALD HfO_2 layers in a [4Hf + 1La] sequence, either 2 or 3 of them are intermixed with the underlying La_2O_3 according to the calculated relative thickness ratio. (Note that we consider only intermixing that happens with the underlying layer, because bidirectional intermixing involves layers both under and above the layer of interest, which gives the same result.) So the La-free HfO_2 is either two or one ALD layers and the ideal relative thickness ratio is 1.0 or 0.33, respectively. The value calculated by relative thickness is 0.61, which is in the middle. For the [6Hf + 1La] sample, the calculated relative thickness ratio value of 1.06 implies 6 ALD layers of HfO_2 are composed of 3 ALD layers of La-free HfO_2 and 3 ALD layers of HfO_2 intermixing with La. For the [8Hf + 1La] sample, the calculated relative thickness ratio value of 1.38 is close to the ratio of 5 ALD layers of La-free HfO_2 and 3 ALD layers HfO_2 intermixing with La (5Hf/3Hf = 1.67). Therefore, more than two and less than three layers of HfO_2 intermix with La_2O_3.

3.3.2. Void Fraction by Ellipsometry

The film thickness, fit by the Cauchy model, decreases differently after the same annealing condition for different HfO_2:La_2O_3 ALD cycle ratios. The thickness of an 11.0 nm [1Hf + 1La] × 84 sample decreases to 8.8 nm after 900 °C 30 s annealing in a N_2 atmosphere; the absolute thickness decrease is 2.2 nm and the reduction is 20%. (A 1 nm SiO_2 interfacial layer forms during deposition,[10] and the thicknesses reported in this paragraph include the interfacial layer.) But for films with larger *x* values, the thickness decrease is much smaller. An 11.2 nm [4Hf + 1La] × 32 sample and an 11.0 nm [8Hf + 1La] × 15 sample both decreased to 10.6 nm after 900 °C 30 s annealing in N_2 (6 and 4%

thickness reduction, respectively). Finally, an 11.1 nm HfO_2 film grown by 125 cycles ($x \rightarrow \infty$) decreases to 10.7 nm after annealing at the same condition (4% reduction). The thickness reductions of pure HfO_2 and [xHf + 1La] with larger x values (4 and 8) in our study are close to HfO_2 films grown at 300 °C from a $HfCl_4$ precursor that have a reported density of 9.6 g/cm^3.[36] The density of a 10 nm HfO_2 film grown in this study was 9.9 g/cm^3, as measured by X-ray reflectometry (XRR). The thickness reduction of [1Hf + 1La] × 84 in our study is even higher than HfO_2 grown at 200 °C in ref 36 that had a density of 8.8 g/cm^3. The thickness decrease differences between [xHf + 1La] with smaller and larger x values suggest that their atom packing arrangement may be different.

The Hf and La precursor ligands differ in size; Hf and La ions differ in both cation radii and coordination number, and the Hf–O and La–O bond lengths differ. So it is reasonable to expect different atom packing arrangements for the La-free HfO_2 and the $HfLa_xO_y$ regions. The packing arrangements determine the thickness decrease for films before and after annealing, as well as the density of the as-deposited films.

When a film is not dense, its complex dielectric function can be represented by the effective medium approximation (EMA) model.[37] The usual interpretation of the EMA theory is that small particles of one material are suspended in a matrix of the host material, voids and solid in this case. The use of void, with optical constants of empty space (or air), is simply a convenient way to raise or lower the dielectric constant of a known material to obtain the dielectric constant for the material of interest. The term should not be taken to imply the presence of small cavities, which could be seen with high-resolution microscopy.[37] In the Bruggeman EMA model, the complex dielectric function of ε is defined as in Eq. 3[38]

$$f_A \cdot \frac{\varepsilon_A - \varepsilon}{\varepsilon_A + 2\varepsilon} + f_B \cdot \frac{\varepsilon_B - \varepsilon}{\varepsilon_A + 2\varepsilon} = 0 \tag{3}$$

where f_A and f_B are the volume fractions of each constituent material, and ε_A and ε_B are their complex dielectric functions. Herein we denote the solid component as A and voids as B. Material A can be described by another EMA model, which is composed of HfO_2 and La_2O_3 with Si impurities ($LaSi_yO_x$), as illustrated in Illustration 3.3.

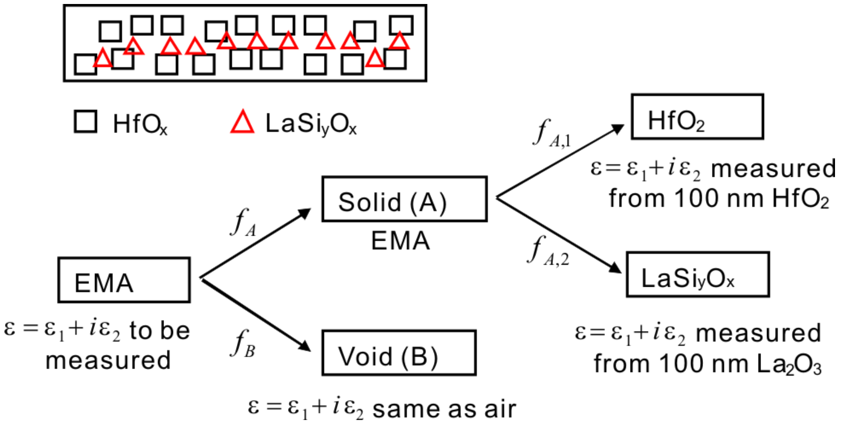

Illustration 3.3. Schematic illustration of a film described by an EMA model, which incorporates a solid (material A) with its separate EMA model and voids (material B). Volume fractions f_A, f_B are fitted to the spectra; volume fractions $f_{A,1}, f_{A,2}$ are calculated from the measured atomic composition. The optical properties of HfO_2 and La_2O_3 are measured from two 100 nm thick samples.

To describe the EMA model (solid A) that represents the solid part in the film, one needs the volume fractions of the two constituents in material A, $f_{A,1}$ and $f_{A,2}$, and their dielectric functions. A 100 nm HfO_2 film and a 100 nm La_2O_3 film (with 9.6% Si impurity) are deposited to determine the optical properties of HfO_2 and $LaSi_yO_x$.

Knowing the density of amorphous HfO_2, La_2O_3 and SiO_2, $f_{A,1}$ and $f_{A,2}$ can be calculated by converting their atomic percentage calculated by XPS to the corresponding volume fractions. Here XPS is conducted using Al Kα at 1486.6 eV and a fixed 45° take off angle to acquire the averaged overall atomic percentage of Hf, La and Si in the bulk film. The atomic percentage is shown in Figure 3.5a and the volume fraction of $LaSi_yO_x$ ($f_{A,2}$) is shown in Figure 3.5b. Both the atomic percentage of La and Si and the volume fraction of $LaSi_yO_x$ decrease gradually with increasing HfO_2:La_2O_3 ALD cycle ratio.

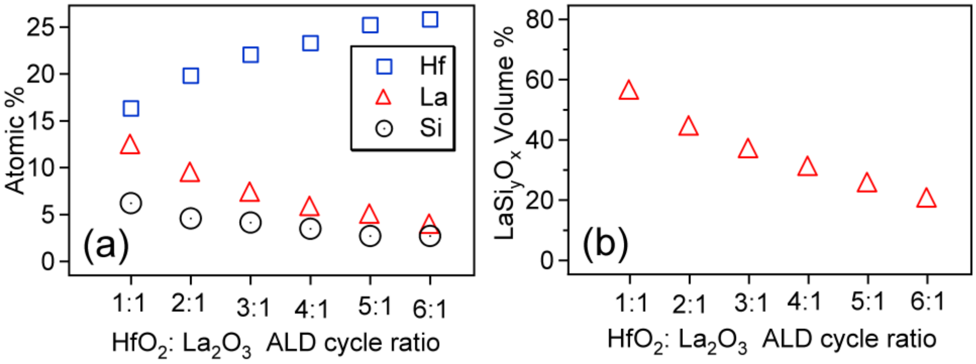

Figure 3.5. (a) Overall atomic percentage of Hf, La, and Si impurities; (b) and volume fraction of $LaSi_yO_x$ ($f_{A,2}$) in solids of a set of 10 nm as-deposited [xHf + 1La] films, where x = 1–6.

Six 10 nm as-deposited (i.e., before annealing) samples with HfO_2:La_2O_3 ALD cycle ratios varying from 1:1 to 6:1 are characterized using the method described above. The fitting is performed for the 70° incident angle data, and at the range of 1.24−5.3 eV, or 234−1000 nm, which is much longer then the film thickness and sample roughness. As shown in images a and b in Figure 3.6, the root-mean-square (rms) roughness of as-deposited 10 nm [2Hf + 1La] × 45 and [6Hf + 1La] × 22 samples are 0.139 and 0.132 nm, respectively. The rms roughness of as-deposited 10 nm HfO_2 is 0.131 nm (image not shown).The samples have smooth surfaces without any distinguishable features, and the morphology does not change with different HfO_2:La_2O_3 ALD cycle ratios. Thus a simple three-phase model consisting of substrate/film(EMA)/ambient is used to fit the data since the surface morphology should not effect the ellipsometry result.

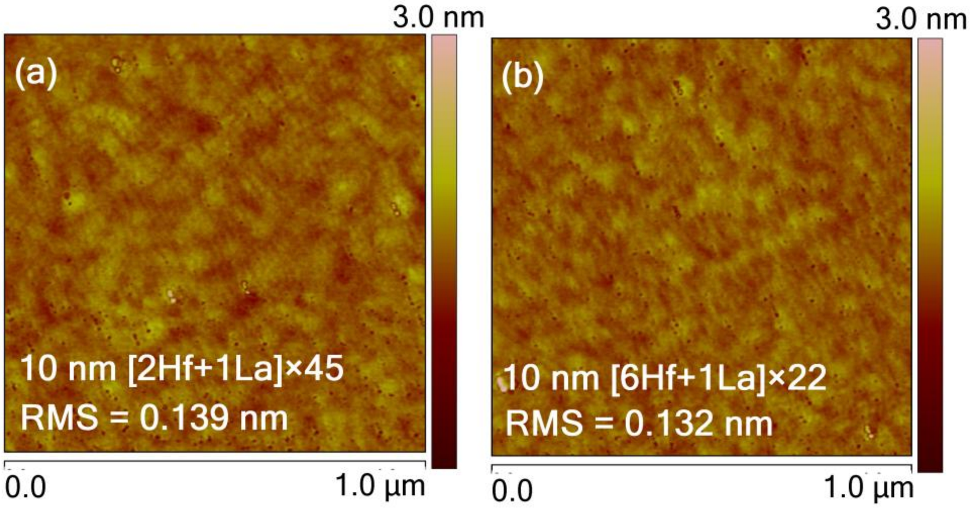

Figure 3.6. AFM images of as-deposited 10 nm (a) [2Hf + 1La] × 45 and (b) [6Hf + 1La] × 22 samples; the rms roughness is (a) 0.139 and (b) 0.132 nm.

The depolarization factor, which is a factor in the EMA model of the J. A. Woollam ellipsometry analysis software WVASE32 describing the shape of the constituents in the host matrix, is fixed to avoid correlation effects. A value of 1/3, corresponding to spherical shaped voids, is used. If a depolarization factor of 0 (needlelike) or 1 (columnar) is used, the calculated void fractions increase ~2% or decrease ~1% for each data point, respectively, whereas the shape of the resultant data curve remains the same. Because the void fraction calculated from the EMA model is more for comparison purposes in this study, the default depolarization factor of 1/3 (spherical) is used.

The calculated void fractions are shown in Figure 3.7 and a typical ellipsometry spectrum of 10 nm as-deposited [1Hf + 1La] × 84 (the 1:1 sample) is presented as the inset. The resultant MSE values for the six samples are 5.9, 5.7, 5.9, 6.0, 6.2, and 6.3 from 1:1 to 6:1, respectively, indicating reasonably good fitting. Unlike Figure 3.5, the trend of the void fraction can be separated into two distinct parts. If the HfO_2:La_2O_3 ALD cycle ratio is 1:1 or 2:1, the void fraction is about 17.2%. When the ratio is 3:1 and above, the void fraction abruptly drops to 14.8% and then decreases very slowly.

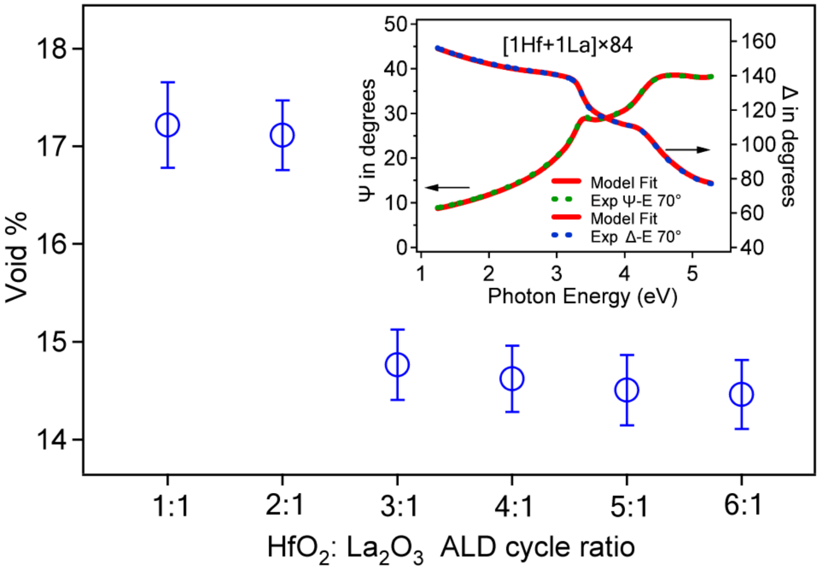

Figure 3.7. Void fractions of six as-deposited 10 nm [*x*Hf + 1La] films, where *x*=1–6; inset, a typical ellipsometry spectrum of as-deposited 10 nm [1Hf + 1La] × 84.

Depolarization may affect the ellipsometry measurements due to incoherent reflections caused by excessive scattering, film thickness inhomogeneity, roughness, etc. Depolarization (or 1.0 – polarization) is mainly a concern when analyzing ellipsometry data from thick and/or inhomogeneous samples with large-scale nonuniformity. For the 6 samples with 1:1 to 6:1 HfO_2:La_2O_3 ALD cycle ratios, the measured depolarization curves from 1.24–5.3 eV are very close and are on the same order as the curve for Si(100) with a native oxide film (figure not shown). Thus depolarization affects all films similarly and there are no obvious differences between low and high x in the [xHf + 1La] films.

The La_2O_3 layer, which is not a complete monolayer, is mismatched dimensionally with HfO_2 and the partial layer is expected to have a different structure. Until Hf precursor molecules adsorb on a continuous HfO_2 film, the effective density of the incremental film that is added in each Hf cycle will be affected by the mismatch between HfO_2 and La_2O_3. The mismatch can also be explained by the retarded chemical adsorption process of the Hf precursor on a heterogeneous surface.[39] If $Hf[N(CH_3)(C_2H_5)]_4$ adsorbs on a Hf–OH surface (as in an ALD cycle of pure HfO_2), the distance between and the number density of –OH sites on the surface should be more uniform. But if $Hf[N(CH_3)(C_2H_5)]_4$ adsorbs on a heterogeneous (OH–Hf + La–OH) surface, the distance and the local number density of the –OH sites on the surface are more likely varied because of the different cation radii and coordination number of Hf and La, leading to a packing mismatch. This could affect the film structure and decreases the film density. The discontinuity in Figure 3.7 suggests that it takes three Hf cycles for HfO_2 to grow on itself, consistent with ~30% monolayer coverage/cycle of HfO_2 grown from the same Hf precursor.[40] After the third ALD layer of HfO_2 is deposited, the heterogeneous surface changes to a continuous Hf–OH surface, enhancing the adsorption of Hf precursors, which leads to a different structure with a different dielectric function and lower void fraction, compared with the La_2O_3–HfO_2 mixture during the deposition of the first three Hf cycles. Stated differently, one ALD layer of La_2O_3 interacts with more than two and less than three ALD layers of HfO_2 by forming a different structure, and the third ALD layer of HfO_2 is sufficient to terminate the interaction.

Both qualitative analysis of (La 3d)/(O 1s) ratios by AR-XPS and void fractions by ellipsometry indicate that La_2O_3 interacts with more than two and less than three ALD layers of HfO_2 in ALD grown La-incorporated HfO_2 films. Thus if $x > 3$ for a $[x\text{Hf} + 1\text{La}] \times n$ film, an $HfLa_xO_y$–HfO_2–$HfLa_xO_y$ structure does exist. Based on this, it is reasonable to conclude that the film is composed of repeated periodic $HfLa_xO_y$-HfO_2-$HfLa_xO_y$ structures because of the layer-by-layer growth mechanism of ALD, which supports what we proposed in the previous work (Chapter 2).[10]

3.4. SUMMARY

In summary, AR-XPS and ellipsometry are used to confirm the existence of a periodic structure of ALD grown La–HfO_2 films. More than two and less than three layers of HfO_2 interact with La_2O_3. From ellipsometry analysis, the interaction is composed of the first two ALD layers of HfO_2 mismatching with La_2O_3, and a third ALD layer that produces a continuous HfO_2 layer, which changes the film structure and lowers the void fraction. The quantitative analysis of (La 3d)/(O 1s) photoelectron intensity ratios acquired at near grazing AR-XPS take off angles indicates the one ALD layer of La_2O_3 interacts with more than two and less than three ALD layers of HfO_2; and the qualitative analysis illustrates at least 4 ALD layers of HfO_2, i.e., [4Hf + 1La], are necessary for La-free HfO_2 interval layers to exist in the film. This AR-XPS-ellipsometry complementary characterization method should be applicable to understand the intermixing phenomena in other ALD-grown periodic structure systems.

3.5. REFERENCES

(1) Suntola, T. *Thin Solid Films* **1992**, *216*, 84–89.

(2) Puurunen, R. L. *J. Appl. Phys.* **2005**, *97*, 121301/1–121301/52.

(3) Van, T. T.; Chang. J. P. *Appl. Phys. Lett.* **2005,** *87*, 011907/1–11907/3.

(4) Van, T. T.; Bargar, J. R.; Chang. J. P. *J. Appl. Phys. 100*, **2006**, 023115/1–023115/8.

(5) Toriumi, A.; Kita, K. In *Dielectric Films for Advanced Microelectronics*; Baklanov, M.; Green, M.; Maex, K. ; John Wiley & Sons: Hoboken, NJ, 2007; p. 297–336.

(6) Wilk, G. D.; Wallace, R. M.; Anthony, J. M. *J. Appl. Phys.* **2000**, *87*, 484–492.

(7) Tomida, K.; Kita, K.; Toriumi, A. *Appl. Phys. Lett.* **2006**, *89*, 142902/1–142902/3.

(8) Ho, M.-Y.; Gong, H.; Wilk, G. D.; Busch, B. W.; Green, M. L.; Lin, W. H.; See, A.; Lahiri, S. K.; Loomans, M. E.; Raisanen, P. I.; Gustafsson, T. *Appl. Phys. Lett.* **2002**, *81*, 4218–4220.

(9) Cho, M.-H.; Chang, H. S.; Cho, Y. J.; Moon, D. W.; Min, K.-H.; Sinclair, R.; Kang, S. K.; Ko, D.-H.; Lee, J. H.; Gu, J. H.; Lee, N. I. *Appl. Phys. Lett.* **2004**, *84*, 571–573.

(10) Wang, T.; Ekerdt, J. G. *Chem. Mater.* **2009**, *21*, 3096–3101.

(11) Park, T. J.; Kim, J. H.; Jang, J. H.; Na, K. D.; Hwang, C. S.; Yoo, J. H. *Electrochem. Solid- State Lett.* **2008**, *11*, H121–H123.

(12) Majumder, P.; Jursich, G.; Takoudis C. *J. Appl. Phys.* **2009**, *105*, 104106/1–104106/6.

(13) Katamreddy, R.; Inman, R.; Jursich, G.; Soulet, A.; Takoudis, C. *Acta Materialia* **2008**, 56, 710–718.

(14) Van, T. T.; Hoang, J.; Ostroumov, R.; Wang, K. L.; Bargar, J. R.; Lu, J.; Blom, H.-O.; Chang, J. P. *J. Appl. Phys.* **2006**, *100*, 073512/1–073512/7.

(15) Desurvire, E. *Erbium-Doped Fiber Amplifiers*; Wiley: New York, 1994.

(16) Wilk, G. D.; Wallace, R. M.; Anthony, J. M. *J. Appl. Phys.* **2001,** *89*, 5243–5275.

(17) Gusev, E. P.; Cabral, C.; Copel, M.; D'Emic, C.; Gribelyuk, M. *Microelectron. Eng.* **2003**, *69*, 145–151.

(18) Mommer, N.; Lee, T.; Gardner, J. A. *J. Mater. Res.* **2000**, *15*, 377–381.

(19) Zhao, X.; Vanderbilt, D. *Phys. Rev. B* **2002**, *65*, 233106/1–233106/4.

(20) Cho, M.-H.; Roh, Y. S.; Whang, C. N.; Jeong, K.; Choi, H. J.; Nam, S. W.; Ko, D.-H.; Lee, J. H.; Lee, N. I.; Fujihara, K. *Appl. Phys. Lett.* **2002**, *81*, 1071–1073.

(21) Adelmann, C.; Kesters, J.; Opsomer, K.; Detavernier, C.; Kittl, J. A.; Van Elshocht, S. *Appl. Phys. Lett.* **2009**, *95*, 091911/1–091911/3.

(22) Powell, C. J.; Jablonski, A. *NIST Electron Effective-Attenuation-Length Database*; Version 1.; National Institute of Standards and Technology: Gaithersburg, MD, 2001.

(23) Champaneria, R.; Mack, P.; White, R.; Wolstenholme, J. *Surf. Interface Anal.* **2003**, *35*,1028–1033.

(24) Mack, P.; White, R. G.; Wolstenholme, J.; Conard, T. *Appl. Surf. Sci.* **2006**, *252*, 8270–8276.

(25) Chang, J. P.; Green, M. L.; Donnelly, V. M.; Opila, R. L.; Eng, J., Jr.; Sapjeta, J.; Silverman, P. J.; Weir, B.; Lu, H. C.; Gustafsson, T.; Garfunkel, E. *J. Appl. Phys.* **2000**, *87*, 4449–4455.

(26) Jablonski, A.; Powell, C. J. *J. Electron Spectrosc. Relat. Phenom.* **1999**, *100*, 137–160.

(27) Vitchev, R. G.; Defranoux, Chr.; Wolstenholme, J.; Conard, T.; Bender, H.; Pireaux, J. J. *J. Electron Spectrosc. Relat. Phenom.* **2005**, *149*, 37–44.

(28) Fujiwara, H. *Spectroscopic Ellipsometry: Principles and Applications*; Wiley: West Sussex, U.K., 2007.

(29) Kimura, H. *Mater. Res. Soc. Symp. Proc.* **2000**, *621*, Q5.7.1–Q.75.7.6.

(30) Kukli, K.; Ritala, M.; Sajavaara, T.; Keinonen, J.; Leskela, M. *Chem. Vap. Deposition* **2002**, *8*, 199–204.

(31) He, W.; Schuetz, S.; Solanki, R.; Belot, J.; McAndrew, J. *Electrochem. Solid-State Lett.* **2004**, *7*, G131–G133.

(32) Suzuki, M.; Kagawa, M.; Syono, Y.; Hirai, T. *J. Cryst. Growth.* **1991**, *112*, 621–627.

(33) De Asha, A. M.; Critchley, J. T. S.; Nix, R. M. *Surf. Sci.* **1998**, *405* (2/3), 201–214.

(34) Seah, M. P.; Dench, W. A. *Surf. Interface Anal.* **1979**, *1*, 2–11.

(35) Kimura, K.; Nakajima, K.; Conard, T.; Vandervorst, W. *Appl. Phys. Lett.* **2007**, *91*, 104106/1–104106/3.

(36) Triyoso, D.; Liu, R.; Roan, D.; Ramon, M.; Edwards, N. V.; Gregory, R.; Werho, D.; Kulik, J.; Tam, G.; Irwin, E.; Wang, X. -D.; La, L. B.; Hobbs, C.; Garcia, R.; Baker, J.; White, B. E., Jr.; Tobin, P. *J. Electrochem. Soc*. **2004**, *151*, F220–F227.

(37) Tompkins, H. G.; McGahan, W. A. *Spectroscopic Ellipsometry and Reflectometry: A User's Guide*; John Wiley & Sons: New York, 1999.

(38) Aspnes, D. E.; Theeten, J. B.; Hottier, F. *Phys. Rev. B* **1979**, *20*, 3292–3302.

(39) Kim, S. K.; Choi, G. J.; Kim, J. H.; Hwang, C. S. Chem. Mater. **2008**, *20*, 3723–3727.

(40) Consiglio, S.; Mo, R. T.; Tai, T. -L.; Krishnan, S. A.; O'Meara, D.; Wajda, C.; Chudzik, M. P. *ECS Trans.* **2007**, *6*, 167–177.

Chapter 4: Optical Properties of La-Incorporated HfO_2 upon Crystallization

4.1. INTRODUCTION

Due to the aggressive scaling of complementary metal-oxide-semiconductor devices, alternative gate dielectrics with higher permittivity values are required to replace conventional SiO_2.[1] For many high-*k* materials under consideration, HfO_2 has attracted considerable attention because of its advantages such as reasonably high dielectric constant (~ 20), relatively wide band gap (5.33–5.9 eV),[2,3] and compatibility with the Si substrate.[4] However, the main drawback of HfO_2 is its low crystallization temperature (~ 500 °C) that results in a polycrystalline phase.[5,6] Since the grain boundaries of the crystallized film may serve as a leakage paths, it is more desirable to stabilize HfO_2 in its amorphous phase.

To stabilize the amorphous phase, SiO_2 and Al_2O_3 have been incorporated into HfO_2.[6–9] But the dielectric constants of these films are lower than HfO_2. Being a high-*k* material with a dielectric constant of more than 20,[10] La_2O_3 is another choice to suppress crystallization, which has been achieved by cosputtering, chemical vapor deposition (CVD) and atomic layer deposition (ALD).[11–13] Introducing 13% La (metal basis) increases the film crystallization temperature of a 10 nm film from 450 °C to 800 °C.[1] Unlike SiO_2 and Al_2O_3, the incorporated of La_2O_3 will not degrade the dielectric constant of La-incorporated HfO_2 (La-HfO_2) films.[11,13]

Despite being a potential high-*k* material that can remain amorphous after high temperature annealing without compromising its dielectric constant, knowledge of the optical properties of La-HfO_2 thin films is still limited and these properties are highly related with the film structure. We have shown (Chapter 3) that La atoms can be periodically distributed in as-deposited La-HfO_2 thin films,[14] but the Hf-La interaction upon annealing is still unclear. In this study, we employed spectroscopic ellipsometry (SE) to investigate the change of La-HfO_2 optical properties with regard to different La-incorporation levels as well as different annealing temperatures, with the purpose of understanding the change of film structure upon crystallization for HfO_2 and La-HfO_2 with different La-incorporation levels.

4.2. EXPERIMENTAL DETAILS

La-HfO_2 thin films are deposited on n-Si(100) substrates by ALD at 250 °C, using tetrakis (ethylmethylamino) hafnium $Hf[N(CH_3)(C_2H_5)]_4$ (TEMAH), tris[*N*, *N*-bis(trimethylsilyl)-amino] lanthanum $La[N(SiMe_3)_2]_3$ and H_2O as precursors, which are held at 85, 150, and 25 °C, respectively. A detailed ALD reactor description is reported elsewhere.[13] Linear growth of HfO_2 and La_2O_3 thin films, 0.78 and 0.50 Å/cycle, respectively, is achieved at the stated condition. According to the X-ray photoelectron spectroscopy (XPS) analysis, HfO_2 films are stoichiometric and carbon free; La_2O_3 films are also carbon free but there is always a 7.9% Si contamination (by atomic percentage), which is commonly observed in La_2O_3 grown using the same precursor.[2] The Si impurities do not show a significant effect on film dielectric constant because only 13% of La (metal basis) is required for a 10 nm La-HfO_2 to remain amorphous after 800 °C annealing, and 7.9% of the La portion constitutes less than 2.5% of the entire film.[13] The La-incorporation is achieved by growing HfO_2 and La_2O_3 alternately; x cycles of HfO_2 are grown plus one cycle of La_2O_3, and then this sequence is repeated n times to achieve the desired thickness. Films growth always ends with an xHf cycle and is referenced as $[x\text{Hf} + 1\text{La}] \times n$. SE is conducted using a J.A. Woollam M2000 Spectroscopic Ellipsometer at 1.24 ~ 6.46 eV and an incident angle of 70°. All as-deposited samples are confirmed to be 11nm (10 nm high-k + 1 nm interfacial SiO_2). Annealing is conducted using the rapid thermal annealing (RTA) process at different temperatures for 30 s in a N_2 environment. The crystallinity of the films is studied using grazing incidence X-ray diffraction (GIXRD) at a 0.5° incident angle.

4.3. RESULTS AND DISCUSSION

It has been shown that the dielectric functions of HfO_2 films change as a function of annealing temperatures, indicating the amorphous to polycrystalline phase transformation in the film.[16] The crystallinity of 10 nm HfO_2 is characterized by XRD, shown as the inset in Figure 4.1a. The as-deposited film is amorphous and crystallizes after 500 °C annealing for 30 s. The diffraction peaks at $2\theta = 24.6$, 28.5, 31.8, and 35.6° can be assigned to the monoclinic phase of HfO_2. The real and the imaginary parts of the complex dielectric constant and the absorption coefficient of the film are extracted from the SE spectra using the point-by-point fitting algorithm described elsewhere.[3,4] The imaginary part (ε_2) of the dielectric constant of 10 nm as-deposited, 500, and 800 °C annealed samples is shown in Figure 4.1a. For the as-deposited amorphous sample, ε_2 exhibits a small absorption tail below the gap. This weak absorption tailing is attributed to the disorder of the amorphous network, which causes non-zero density of states in the band gap, allowing optical transitions between these band tails.[18] Compared with the amorphous sample, ε_2 of the 500 °C 30 s annealed sample, which is shown to be crystallized in XRD (inset of Figure 4.1), exhibits a shoulder at 5.9 eV, as reported by other authors.[16,19,20] Increasing the annealing temperature to 800 °C does not change ε_2 noticeably. The appearance of the shoulder at 5.9 eV is because of singularities in the interband states formed as the film changes structure during annealing. These singularities are caused by the presence of long-range order in materials and can be considered as a sign of crystallization.[16,21]

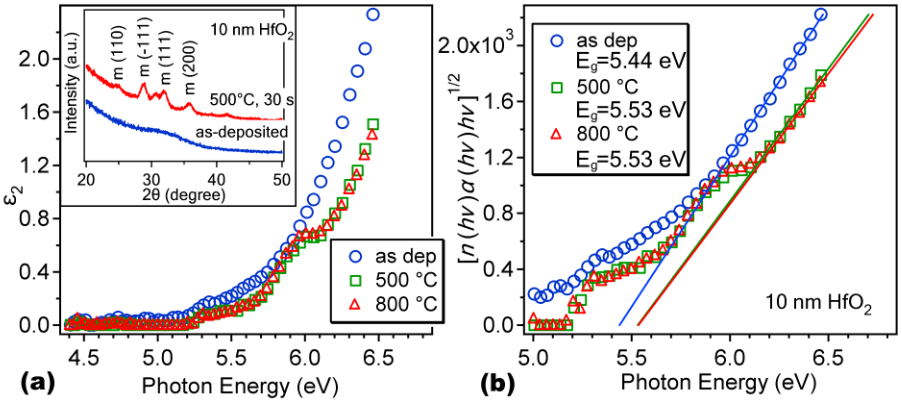

Figure 4.1. (a) ε_2 of the dielectric constant and (b) E_g determined from the Tauc plot for 10 nm HfO_2 films upon different annealing conditions. Inset, XRD spectra of 10 nm HfO_2.

The film crystallinity can also be correlated to the band edge density of states, in particular the bandgap energy (E_g). E_g is given by the Tauc plot,[22] as the empirical expression $[n(hv)\alpha(hv)hv]^{1/2}$ versus hv, where n, α, and hv are the index of refraction, the absorption coefficient, and the photon energy (hv), respectively. It is reported that this expression exhibits a linear relationship with hv near the band edge, and E_g can be accurately determined by extrapolating to zero.[19] As shown in Figure 4.1b, E_g of the amorphous HfO_2 is 5.44 ± 0.06 eV, and the E_g values of the crystallized HfO_2 after 500 and 800 °C annealing are both 5.53 eV, with an uncertainty of 0.08 and 0.07 eV, respectively. E_g of the crystalline phase is higher than that of the amorphous phase because the band edge tailing effect is reduced in crystallized films.[23] For the amorphous film, the density of states in the gap is not zero and transitions between these states will lower the bandgap because of the disorder in the amorphous structure. After high temperature annealing, the crystallization process will reduce these states in the gap as long-range order establishes in the structure.

Figure 4.2a and b compare ε_2 and E_g for 10 nm as-deposited HfO_2 and La-incorporated $[x\text{Hf} + 1\text{La}] \times n$, where $x = 6$ and 1. A value of $x = 6$ leads to periodic structures consisting of La_2O_3-free HfO_2 layers separated by $HfLa_xO_y$ formed by 1 La ALD cycle and 3–4 Hf ALD cycles.[14] A value of $x = 1$ leads to homogeneous-like films.[14] In Figure 4.2a, all as-deposited samples display very similar absorption tails at 5.2 ~ 5.6 eV for HfO_2 and 5.2 ~ 5.8 eV for $x = 6$ and 1 samples before the onset of the conduction band, indicating the disorder in the film structure is similar in these as-deposited amorphous samples, regardless the La-incorporation level or the distribution of La in the films. However, the shape of the band tails for HfO_2 and La-HfO_2 will show a big difference after the film is crystallized (see below). After the onset of the conduction band, samples with higher La-incorporation levels have lower ε_2 because the refractive index of La_2O_3 is smaller than that of HfO_2.

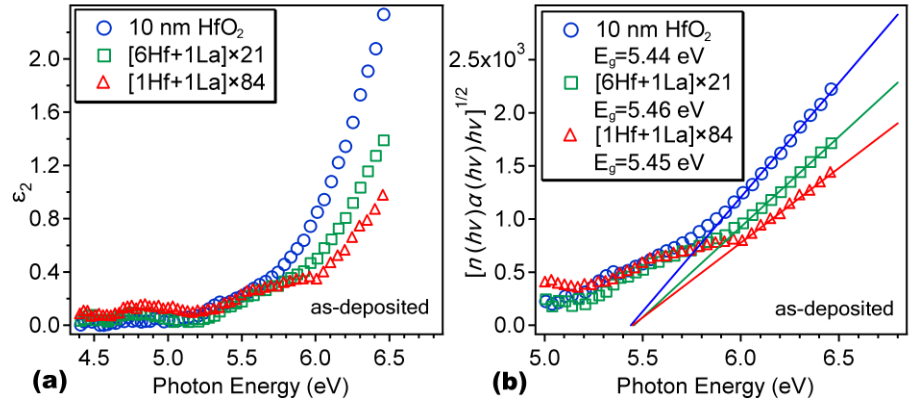

Figure 4.2. (a) ε_2 of the dielectric constant and (b) E_g determined from the Tauc plot for 10 nm as-deposited HfO_2 and $[x\text{Hf} + 1\text{La}] \times n$, where $x = 6$ and 1.

E_g of the samples are extracted from the Tauc plots and three representative curves are shown in Figure 4.2b. The calculated E_g values for as-deposited [xHf + 1La] × n, where $x = 8$, 6, 3 and 1, are 5.44 ± 0.09, 5.46 ± 0.08, 5.47 ± 0.09 and 5.45 ± 0.10 eV, respectively (only three samples are shown in the figure). For different as-deposited samples, E_g remains constant within the experimental uncertainty and is essentially equivalent to HfO_2 ($E_g = 5.44 \pm 0.06$,), indicating La-incorporation up to 43% ([1Hf + 1La] × 84, by XPS, on a metal basis,[13]) does not affect E_g. This is because the E_g of bulk HfO_2 and La_2O_3 are both ~ 6.0 eV.[24] The reported E_g of a 6 nm La_2O_3 thin film grown by rf cosputtering is 5.3 eV.[17]

For La-HfO_2 samples, changes of ε_2 upon annealing differ in comparison with HfO_2. 10 nm [6Hf + 1La] and [3Hf + 1La] films can remain amorphous up to 800 and 900 °C annealing, respectively.[13] Increasing the annealing temperature for an extra 100 °C will lead to crystallization, as illustrated in the insets of Figure 4.3 a and b. Upon crystallization at 900 and 1000 °C, no shoulder-like feature is developed similar to the one at 5.9 eV for HfO_2. Instead, the absorption tail of the two crystallized La-HfO_2 samples are reduced to zero before the onset of the conduction band, indicating the disorder in the amorphous phase is largely reduced in the crystalline phase of La-HfO_2. For the two samples upon 800 and 900°C annealing, the highest temperature for 10 nm [6Hf + 1La] and [3Hf + 1La] films to remain amorphous, respectively, the absorption tails are reduced to some extent compared to as-deposited samples. After crystallization the ε_2 are considerably reduced to zero. The same relationship of ε_2 and film crystallinity is observed for 10 nm [8Hf + 1La], [4Hf + 1La] and [1Hf + 1La] samples (data not shown) Thus, it can be conclude that La-incorporation reduces the interband states, which are formed during the crystallization of pure HfO_2.

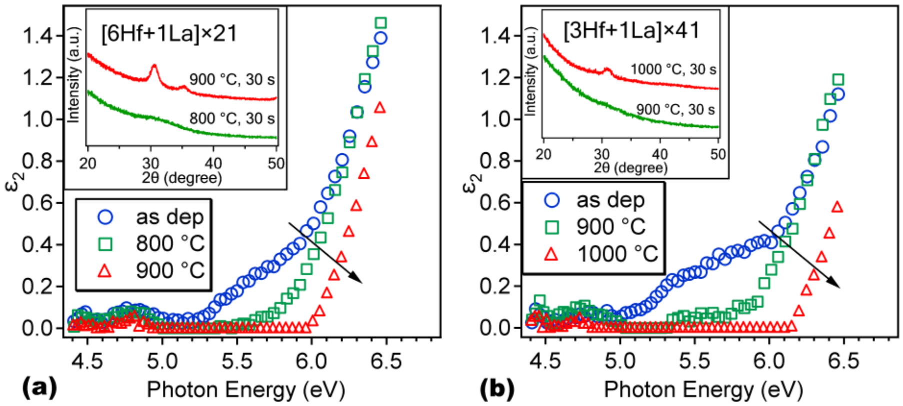

Figure 4.3. ε_2 of 10 nm (a) [6Hf + 1La] and (b) [3Hf + 1La], for as-deposited, and at the highest annealing temperature to remain amorphous (800 and 900 °C, respectively), and at the temperature at which the films crystallize (900 and 1000 °C, respectively).

The Tauc plots of 10 nm [6Hf + 1La] and [3Hf + 1La] films at different annealing conditions are shown in Figure 4.4a and b, respectively. E_g of as-deposited, 800 and 900 °C annealed 10 nm [6Hf + 1La] are 5.46 ± 0.07, 5.64 ± 0.05, and 5.89 ± 0.05 eV, respectively. E_g of as-deposited, 900 and 1000 °C annealed 10 nm [3Hf + 1La] are 5.47 ± 0.09, 5.66 ± 0.08, and 6.02 ± 0.09 eV, respectively. 800 and 900 °C are the highest temperatures for these two films to remain amorphous, respectively. After annealed at these two temperatures, E_g of [6Hf + 1La] and [3Hf + 1La] increase by 0.18 and 0.19 eV compared with the as-deposited films, respectively. After the final annealing at an extra 100 °C (900 and 1000 °C), which leads to crystallization, the E_g values of these two films increase by another 0.25 and 0.36 eV, respectively. The E_g increase during the final 100 °C is much higher than the increase caused by the first 800 and 900 °C. The disorder in the amorphous phase is reduced with increasing annealing temperature, but an amorphous-to-crystalline phase transformation will heal the disorder much more effectively, thus reduce the band tails in the gap and increase E_g.

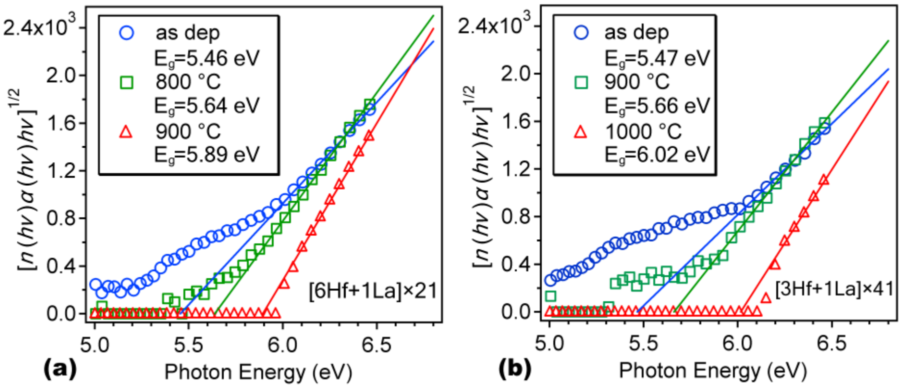

Figure 4.4. E_g determined from the Tauc plot for 10 nm (a) [6Hf + 1La] and (b) [3Hf + 1La], for as-deposited, and at the highest annealing temperature to remain amorphous (800 and 900 °C, respectively), and the temperature at which the film crystallizes (900 and 1000 °C, respectively).

From previous discussion, HfO_2 and La-HfO_2 show some similar optical property changes upon crystallization. For the amorphous phase, ε_2 of both HfO_2 and La-HfO_2 has apparent absorption tails (Figure 4.2a). After crystallization, the absorption tail is reduced and E_g is increased because of the reduction of band tails in the gap, which implies the disorder in the film is reduced upon crystallization. However, there is a major difference between HfO_2 and La-$HfO_{2.}$ ε_2 of 10 nm crystallized HfO_2, [6Hf + 1La] and [3Hf + 1La] are compared in Figure 4.5.

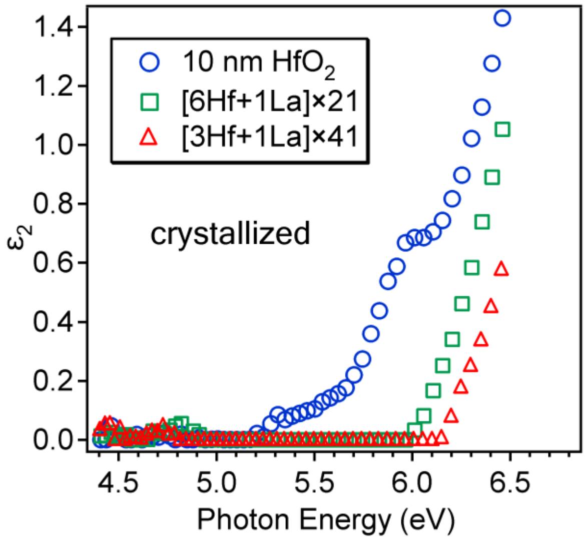

Figure 4.5. ε_2 of 10 nm crystallized HfO_2, [6Hf + 1La], and [3Hf + 1La].

Although long-range order establishes in both HfO_2 and La-HfO_2 after crystallization, ε_2 of pure HfO_2 still has an adsorption tail at ~ 5.5 eV and a shoulder at 5.9 eV, whereas ε_2 of La-HO_2 exhibits an extremely sharp onset of the conduction band. The disorder in thin film HfO_2 cannot be completely fixed when HfO_2 crystallizes into the monoclinic phase. And interband states always forms in crystallized HfO_2 as the shoulder at 5.9 eV has been reported by several authors.[16,19,20] By incorporating La, a new kind of structure almost without disorder is formed in crystallized La-HfO_2. The XRD patterns of crystallized [6Hf + 1La] and [3Hf + 1La] in the insets of Figure 4.3 only show peaks at 2θ = 31 and 36°, which can be assigned to the (111) and (002) planes of tetragonal HfO_2. Crystallized [xHf + 1La] films with variant x values (x = 1 ~ 8) exhibit the same XRD patters: a stronger peak at 31° and a weaker peak at 36°. No monoclinic HfO_2 peaks are found for crystallized [xHf + 1La] films (x = 1 ~ 8). Although the two peaks at 2θ = 31 and 36° for crystallized La-HfO_2 may also be assigned to the cubic phase of HfO_2 and it is difficult to identify between tetragonal and cubic structures only based on the two XRD peaks, the absence of the monoclinic HfO_2 peaks clearly indicates that a phase transformation occurs after the incorporation of La for the crystallized films. Moreover, the fact that as-deposited HfO_2 and La-HfO_2 have similar absorption tails (Figure 4.2a) implies as-deposited La-HfO_2 is more like a mixture of HfO_2 and La_2O_3, rather than an alloy, consistent with the fact that La-incorporation does not change the Hf–O bonding significantly in the as-deposited film.[13] After crystallization, La atoms are forced into the HfO_2 networks, forming a new $HfLa_xO_y$ network with a different structure compared with crystallized HfO_2.

4.4. SUMMARY

In summary, the optical properties of as-deposited and crystallized HfO_2 and La-HfO_2 are studied. As-deposited HfO_2 and La-HfO_2 both have apparent absorption tails in the ε_2 curves, which implies disorder in the amorphous film structure and band tails in the gap. Upon crystallization, the absorption tails are reduced and E_g values are increased for both HfO_2 and La-HfO_2. But disorder still exists and interband states form in pure HfO_2. On the other hand, crystallized La-HfO_2 is almost free of disorder, which might be a result that La atoms are forced into HfO_2 network and a new $HfLa_xO_y$ network is formed after crystallization.

4.5. REFERENCES

(1) Wilk, G. D.; Wallace, R. M.; Anthony, J. M. *J. Appl. Phys.* **2001**, *89*, 5243–5275.

(2) Afanas'ev, V. V.; Stesmans, A.; Chen, F.; Shi, X.; Campbell, S. A. *Appl. Phys. Lett.* **2002**, *81*, 1053–1055.

(3) Buiu, O.; Lu, Y.; Mitrovic, I. Z.; Hall, S.; Chalker, P.; Potter, R. J. *Thin Solid Films* **2006**, *515*, 623–626.

(4) Hubbard, K. J.; Schlom, D. G. *J. Mater. Res.* **1996**, *11*, 2757–2776.

(5) Gusev, E. P.; Cabral, C.; Copel, M.; D'Emic, C.; Gribelyuk, M. *Microelectron. Eng.* **2003**, *69*, 145–151.

(6) Ho, M.; Gong, H.; Wilk, G. D.; Busch, B. W.; Green, M. L.; Lin, W. H.; See, A.; Lahiri, S. K.; Loomans, M. E.; Raisanen, P. I.; Gustafsson, T. *Appl. Phys. Lett.* **2002**, *81*, 4218–4220.

(7) Lee, D.; Suh, D.; Pae, Y.; Kim, H.; Cho, M.; Ko, D. *J. Electrochem. Soc.* **2007**, *154*, H708–H712.

(8) Park, T. J.; Kim, J. H.; Jang, J. H.; Na, K. D.; Hwang, C. S.; Yoo, J. H. *Electrochem. Solid-State. Lett.* **2008**, *11*, H121–H123.

(9) Cho, M.; Chang, H. S.; Cho, Y. J.; Moon, D. W.; Min, K.; Sinclair, R.; Kang, S. K.; Ko, D.; Lee, J. H.; Gu, J. H.; Lee, N. I. *Appl. Phys. Lett.* **2004**, *84*, 571–573.

(10) Yeo, Y.; King, T.; Hu, C. *Appl. Phys. Lett.* **2002**, *81*, 2091–2093.

(11) Yamamoto, Y.; Kita, K.; Kyuno, K.; Toriumi, A. *Appl. Phys. Lett.* **2006**, *89*, 032903/1–032903/3.

(12) Huang, L.; Li, A.; Zhang, W.; Li, H.; Xia, Y.; Wu, D. *Appl. Surf. Sci.* **2010**, *256*, 2496–2499.

(13) Wang, T.; Ekerdt, J. G. *Chem. Mater.* **2009**, *21*, 3096–3101.

(14) Wang, T.; Ekerdt, J. G. *Chem. Mater.* **2010**, *22*, 3798–3806.

(15) Triyoso, D. H.; Hegde, R. I.; Grant, J. M.; Schaeffer, J. K.; Roan, D.; White, B. E.; Tobin, P. J. *J. Vac. Sci. Technol., B* **2005**, *23*, 288–297.

(16) Cho, Y. J.; Nguyen, N. V.; Richter, C. A.; Ehrstein, J. R.; Lee, B. H.; Lee, J. C. *Appl. Phys. Lett.* **2002**, *80*, 1249–1251.

(17) Zhao, Y.; Kita, K.; Kyuno, K.; Toriumi, A. *Appl. Phys. Lett.* **2009**, *94*, 042901/1–042901/3.

(18) Ferlauto, A. S.; Ferreira, G. M.; Pearce, J. M.; Wronski, C. R.; Collins, R. W.; Deng, X.; Ganguly, G. *J. Appl. Phys.* **2002**, *92*, 2424–2436.

(19) Nguyen, N. V.; Davydov, A. V.; Chandler-Horowitz, D.; Frank, M. M. *J. Appl. Phys.* **2005**, *87*, 192903/1–192903/3.

(20) Nguyen, N. V.; Sayan, S.; Levin, I.; Ehrstein, J. R.; Baumvol, I. J.; Driemeier, C.; Krug, C.; Wielunski, L.; Hung, P. Y.; Diebold, A. *J. Vac. Sci. Technol., A* **2005**, *23*, 1706–1713.

(21) Wooten, F. *Optical preoperties of Solids*; Academic: New York, 1972.

(22) Tauc, J. *Amorphous and Liquid Semiconductors*; Plenum: London, 1974; p. 159.

(23) Cohen, M. H.; Fritzsche, H.; Ovshinsky, S. R. *Phys. Rev. Lett.* **1969**, *22*, 1065–1068.

(24) Robertson, J. *Appl. Surf. Sci.* **2002**, *190*, 2–10.

Chapter 5: Structure versus Thermal Stability: the Periodic Structure of ALD-Grown Al-Incorporated HfO_2 Films and Its Effect on Amorphous Stabilization

5.1. INTRODUCTION

In recent years, HfO_2 has attracted considerable attention as a dielectric material to replace conventional SiO_2 because of its high dielectric constant ($k \sim 20$), high bandgap of ~ 5.5 eV and relatively good stability on silicon.[1–5] Unfortunately, amorphous HfO_2 crystallizes after annealing at a relatively low temperature (~ 500 °C).[2] Although crystalline HfO_2 has a higher dielectric constant, stabilizing HfO_2 in its amorphous phase is more desirable because the polycrystalline film grain boundaries serve as a charge leakage pathway and the co-existence of cubic, tetragonal and monoclinic phases results in different dielectric constants among different regions of the device.[1,6,7] Extensive effort has been made to stabilize the amorphous phase of HfO_2, including alloying with Si, Al and La. Sputtering, chemical vapor deposition (CVD), and atomic layer deposition (ALD) have been used to incorporate Si,[8–13] Al,[14–19] and La,[20–22] respectively. Both film thickness and alloy composition need to be considered in evaluating the effectiveness of an alloying element in stabilizing the amorphous phase of HfO_2.

The amorphous nature of HfO_2 is different from SiO_2 in terms of the network structure. Thermally grown SiO_2 has a continuous random network (CRN), while HfO_2 has a random close packed (RCP) structure.[23] The differences between the two types of amorphous structure are related to the molar volume and the coordination number vs. the metal-oxygen (M–O) distance,[24] as well as the electronegativity difference between M and O, and average bond ionicity.[25] Generally speaking, a CRN material is a stronger amorphizer than a RCP material. While forming a CRN structure, each atom in SiO_2 is bonded according to its primary chemical valence and predominantly forms covalent bonds.[25] The Si-O covalent bonds in SiO_2 make SiO_2 a very stable amorphous material. The Hf–O bond in HfO_2 is predominantly ionic,[26] thus O atoms can move around more easily compared with O atoms in SiO_2. Therefore, HfO_2 has a much lower crystallization temperature than SiO_2.

La_2O_3 forms a RCP structure and incorporating La into HfO_2 has been shown to be effective in stabilizing the amorphous phase.[20,21] Although La is a much weaker amorphizer compared with Si, La-incorporation does not decrease the dielectric constant of the alloyed film as found with SiO_2.[20,21] While La_2O_3 and Y_2O_3 are both classified in the RCP group, La is an amorphizer but Y is a crystallizer. Y-incorporation stabilizes the higher dielectric constant cubic HfO_2 phase.[27–29]

According to Zallen's classification, there is a group of modified continuous random network (MCRN) materials between CRN and RCP, in which metal atom ionic bonds disrupt and modify the covalently bonded CRN structure.[25] Al_2O_3 and Ta_2O_5 are examples of MCRNs. Elements forming CRN, MCRN or RCP all show potential to stabilize the amorphous phase of high-k dielectric thin films, thus the choice of incorporating elements involves an optimization/compromise between a stronger amorphizer and a higher dielectric constant. The film crystallization temperatures at a particular alloying element incorporation level are reported,[13,18,30,31] but it is sometimes difficult to compare these temperatures because different film thicknesses were employed.

Thermal stability is closely related to film thickness. Cho et al. reported that while as-deposited 45 Å thick HfO_2 was amorphous, thicker films were grown as a polycrystalline structure of monoclinic or tetragonal phases.[32] Gusev et al. reported the dependence of film crystallization temperature on the thickness of HfO_2 films. The crystallization temperature increased from 430 to 600 °C with thickness decreases from 40 to 5 nm.[2]

The overall energy of a film is determined by the contributions from both the bulk and the surface. Crystalline films have a lower energy than amorphous films. But Navrotsky revealed that the monoclinic HfO_2 and ZrO_2 were found to have the largest surface enthalpy and amorphous HfO_2 and ZrO_2 the smallest.[33] As film thickness decreases, the surface energy of the amorphous phase makes a greater contribution to the total energy, which enables the film to remain amorphous. This is the reason why thinner, as-deposited HfO_2 is generally amorphous while thicker films are generally crystalline.

Physical sputtering, CVD, ALD, and molecular beam epitaxy (MBE) growth are the most commonly used methods to incorporate alloying elements into HfO_2. Our previous work (Chapter 3) showed the existence of a periodic structure resulted from inserting one ALD layer of La_2O_3 between several ALD layers of HfO_2.[34] Less La was required to stabilize an amorphous phase for the $HfLa_xO_y$ system when present in a periodic structure as compared to homogeneous films grown by physical sputtering.[21] Katamreddy et al. report $HfAlO_x$ films grown with 4:2 and 2:1 Hf:Al ALD cycle ratios have different degrees of crystallization after annealing under the same condition, implying the thermal stability is determined by film structure rather than overall Al content.[35] Therefore, the film structure in the growth direction, defined by ALD, shows the potential to be another factor affecting the crystallization temperature of thin films.

In this chapter, Al-incorporated HfO_2 (Al-HfO_2) films are synthesized using ALD to study the relationship between the periodic structure and the film crystallization behavior. The periodic structures are characterized using angle-resolved X-ray photoelectron spectroscopy (AR-XPS). Films are annealed using a rapid thermal annealing (RTA) process. The crystallization of films with comparable compositions and different thickness are studied using grazing incidence X-ray diffraction (GIXRD).

5.2. EXPERIMENTAL DETAILS

Film deposition: Samples are deposited on n-Si(100) substrates at 250 °C using tetrakis (ethylmethylamino) hafnium $Hf[N(CH_3)(C_2H_5)]_4$ (TEMAH), trimethyl aluminum (TMA) and H_2O; the TEMAH is held at 85 °C; TMA and H_2O are at room temperature. A detailed ALD reactor description is reported elsewhere.[21] One cycle consists of metal precursor dosing for 1.5 s (Hf) or 0.75 s (Al), a 25 s purge with Ar, water dosing for 0.05 s, and a 25 s purge with Ar. The growth rate of HfO_2 and Al_2O_3 in our ALD system is 0.78 and 0.90 Å/cycle, respectively. The Si substrates are etched in a 2% HF solution for 30 s, rinsed in deionized water for 20 s, which redeoxidizes the Si(100) surface, and dried with flowing He. The resultant oxide is 10 Å according to ellipsometry. The Al incorporation is achieved by growing HfO_2 and Al_2O_3 alternately; one ALD layer of Al_2O_3 is added after x ALD layers of HfO_2, and then this sequence is repeated n times to achieve the desired thickness. Films are referenced using $[x\mathrm{Hf} + 1\mathrm{Al}] \times n$. Film growth always ends with an xHf cycle. One "ALD layer" does not imply a complete monolayer of a particular material, and we refer to an ALD layer as the amount deposited in a single cycle. Samples of two target thickness are deposited, 10 nm and 40 nm. The as-deposited samples are confirmed to be 11 or 41 nm (10 or 40 nm high-k film + 1 nm interfacial SiO_2) by ellipsometry.

X-ray photoelectron spectroscopy (XPS): After cooling down in the ALD chamber, the as-deposited samples are transferred to a Physical Electronics 5500 XPS system through a load lock with a base pressure of 2×10^{-7} Torr. In situ XPS and AR-XPS are performed using a Mg $K\alpha$ source at 1253.6 eV to investigate the overall film composition and depth composition variation. The angle between the X-ray source and the photoelectron analyzer is 54.7°. The normal take off angle (between the analyzer and the sample surface) is 45°, at which XPS is normally performed. AR-XPS is achieved by tilting the sample in a set of planes perpendicular to the plane defined by the X-ray source and the analyzer. The sample position has been calibrated so that the tilt axis crosses the intersection point of the X-ray and the analyzer.

The XPS raw data are smoothed using the PeakFit (Version 4) to find the starting and ending points for integration; the peak area of the raw data is calculated using the Igor Pro software package. The XPS data are presented as ratios of the (Al 2p)/(O 1s) peak areas. Al 2p XPS raw data smoothing is most difficult at very small take off angles where the signal-to-noise ratios are low, because the choice of the starting and ending points for the integration lead to variations large enough to affect the calculated (Al 2p)/(O 1s) area ratios. To check the reproducibility of the analysis method, five measurements at five different take off angles (7, 12, 18, 22, and 26°) were performed for the [4Hf + 1Al] sample. The error bars are presented (in Figure 5.3c) and after 12° the signal-to-noise ratios for Al 2p and O 1s are such that the error bars are smaller than the vertical segment of the data point symbols.

Annealing and X-ray diffraction (XRD): To find the film crystallization temperature, samples are annealed by rapid thermal annealing (RTA) at different temperatures for 30 s under a N_2 environment. Grazing incidence X-ray diffraction (GIXRD) is performed using a Bruker-AXS D8 Advance Powder Diffractometer with a sealed tube Cu $K\alpha$ radiation, at a fixed 0.5° incident angle and 2θ scan rate of 6°/min.

5.3. RESULTS AND DISCUSSION

5.3.1. Amorphous Stabilization of 10 nm ALD-Grown Al-HfO$_2$ Films

Only Hf, Al, O, and C peaks are observed in the X-ray photoelectron spectra of Al-HfO$_2$ samples. Carbon contamination is introduced to the samples within the load lock during in situ sample transfer. No C signal is detected after Ar$^+$ sputtering at 3 kV over a 3 × 3 mm^2 area for 40 s, which removes ~ 2 nm of the sample surface, indicating the C impurities in the bulk film are below the XPS detection limits (< 1%). The as-deposited film composition is calculated from the integrated Hf 4f, Al 2p and O 1s peaks corrected by their atomic sensitivity factors.[36] Figure 5.1 shows the Al-incorporation level of a series of 10 nm, as-deposited films at different Hf:Al ALD cycles ratios.

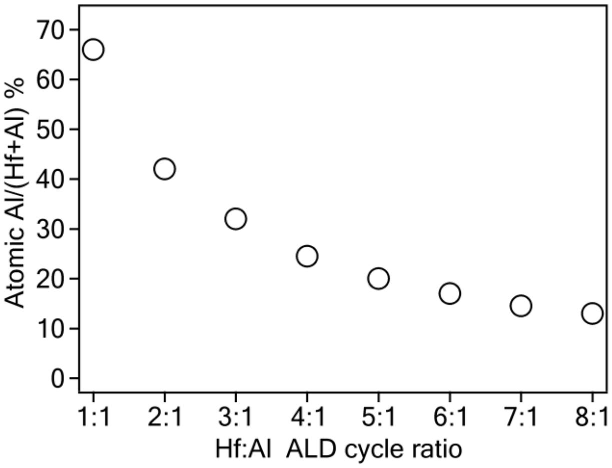

Figure 5.1. The Al-incorporation level of as-deposited Al-HfO$_2$ films versus Hf:Al ALD cycle ratio.

Consistent with previous studies,[18, 19] Al is successfully incorporated into HfO$_2$ using ALD, and the Al concentration can be easily controlled by changing the Hf:Al ALD cycle ratios. When the Hf:Al ALD cycle ratio is 1:1, the Al incorporation concentration is 66% on a metal basis, indicating more Al precursors than Hf precursor adsorbed onto the sample surface during the metal precursor dosing step as expected because the TMA molecule is about three times smaller than TEMAH. When the Hf:Al ALD cycle ratio is 8:1, the Al incorporation level is about 13%.

To investigate the stabilization effects of Al-incorporation, another set of 10 nm Al-HfO_2 films with various Al-incorporation levels were deposited, and then annealed. XRD measurements illustrate the minimum Al-incorporation levels that are needed to stabilize the amorphous phase after 800 and 900 °C annealing, respectively. By inserting one ALD Al_2O_3 layer after every eight ALD HfO_2 layers ($Al/(Hf + Al) = 13\%$), the 10 nm [8Hf + 1Al] × 14 film remains amorphous after 800 °C annealing. Adding one more ALD layer of HfO_2 in every [xHf + 1Al] sequence while keeping the same 10 nm film thickness, the [9Hf + 1Al] × 12 film crystallizes at 800 °C as indicated by the two peaks at $2\theta = 31$ and 36° in the XRD spectrum (Figure 5.2a). These two peaks are close to tetragonal (111) and tetragonal (002) for HfO_2. Similarly, a 10 nm [3Hf + 1Al] × 28 ($Al/(Hf + Al) = 32\%$) remains amorphous as high as 900 °C, but a 10 nm [4Hf + 1Al] × 22 film crystallizes after annealing at the same temperature (Figure 5.2b).

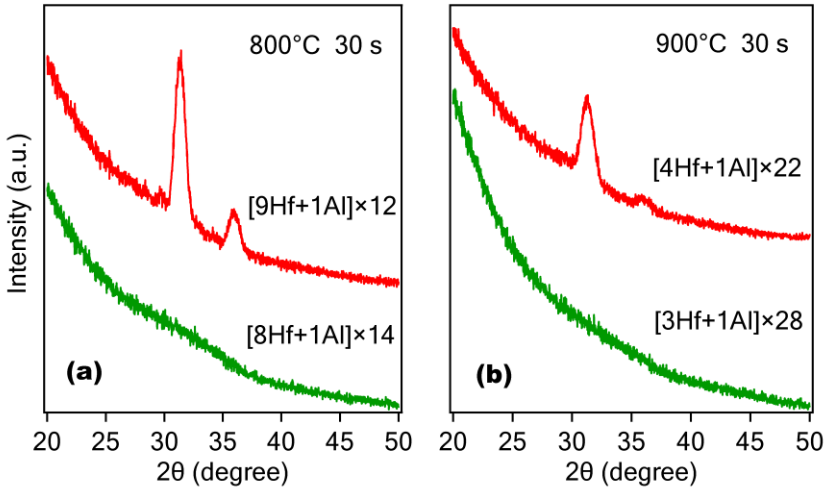

Figure 5.2. XRD spectra showing the minimum Al-incorporation levels for 10 nm Al-HfO_2 films to remain amorphous after 800 and 900 °C annealing for 30 s in a N_2 environment.

Generally, a higher Al-incorporation level increases the thermal stability of Al-HfO_2 films,[18,37] which is related to the changes in the Al–O and Hf–O bonding characteristics during the incorporation of Al_2O_3 into HfO_2.[19] In our case, 13% ([8Hf + 1Al]) and 32% ([3Hf + 1Al]) Al-incorporation stabilizes the amorphous phase up to 800 °C and 900 °C, respectively, using a RTA process for 30 s under a N_2 environment. It is widely reported that Al-HfO_2 can remain amorphous at an annealing temperature higher than 900 °C,[18,31,37] which is high enough for the dopant activation annealing in the fabrication process of self-aligned gate.[38]

5.3.2. Periodicity of ALD-Grown Al-HfO_2 Films

Unlike ALD-grown HfO_2-Al_2O_3 nanolaminates, which are composed of thicker HfO_2 and Al_2O_3 stacks in the thickness of several angstroms,[39,40] it is more difficult to characterize the periodicity of the films used herein since only one ALD layer of Al_2O_3 is inserted and this will not form a complete monolayer of Al_2O_3. AR-XPS has been shown to be a powerful non-destructive tool to determine the thickness, fractional coverage and concentration depth profile for ultrathin films.[41–43] The detected XPS signal is given by $I = I_0\exp(-d/\lambda\sin\theta)$. Lambda, λ, is the effective attenuation length (EAL),[44] and θ is the take off angle between the analyzer and the sample surface. At small take off angles, only photoelectrons from the near surface region are detectable.[43] Although the periodicity of ALD-grown Al-HfO_2 films is smaller than the EAL, at glancing take off angles, the abrupt presence of the first few $HfAl_xO_y$ layers is expected to be detectable using the AR-XPS technique.

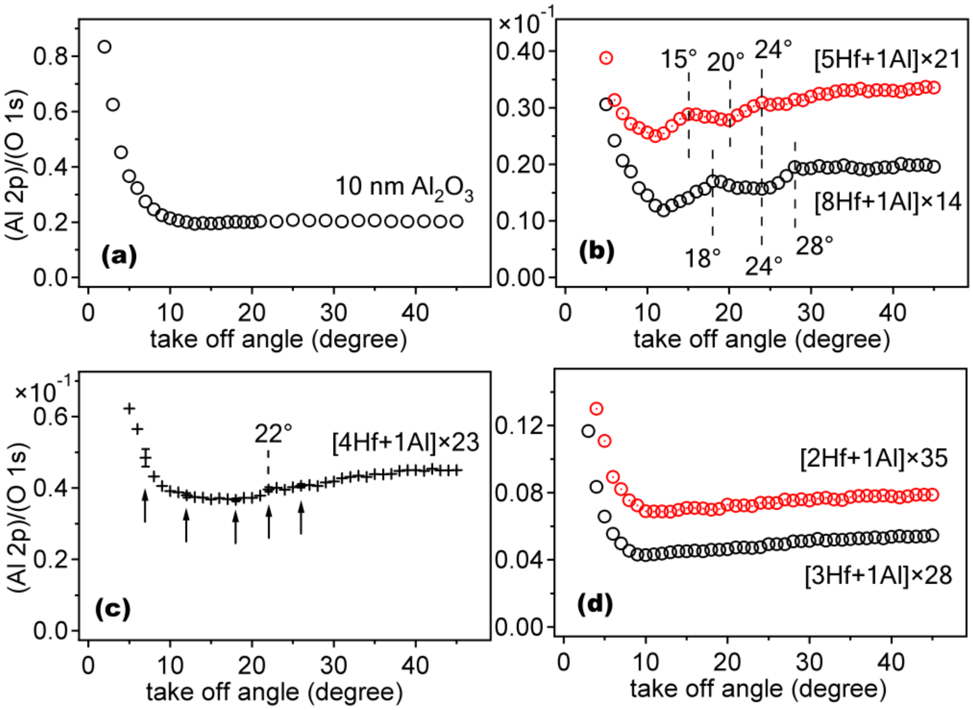

Figure 5.3. (Al 2p)/(O 1s) photoelectron intensity ratios of (a)10 nm Al_2O_3; (b) [8Hf + 1Al] × 14 and [5Hf + 1Al] × 21; (c) [4Hf + 1Al] × 23; (d) [3Hf + 1Al] × 28 and [2Hf + 1Al] × 35 films; error bars at 7, 12, 18, 22, and 26° for the [4Hf + 1La] × 23 sample are shown at the corresponding data points, respectively.

For each sample, AR-XPS is conducted from near grazing to 45° take off angles. Figure 5.3a shows the result of a 10 nm pure Al_2O_3 film. The (Al 2p)/(O 1s) value is high initially because of the scattering effects of the photoelectrons. At near grazing take off angles, photoelectrons may escape from the surface by a shortcut, enabling signals from deeper depths to be detected.[45] This effect is more significant for Al 2p as the EAL(Al 2p) > EAL(O 1s). After 12°, the take off angle is large enough and the scattering effects no longer play an important role, so the (Al 2p)/(O 1s) ratio remains reasonably constant as the film is wholly composed of Al_2O_3.

Figure 5.3b shows AR-XPS results for samples with high Hf:Al ALD cycle ratios (8:1 and 5:1). For the [8Hf + 1Al] × 14 sample, the (Al 2p)/(O 1s) curve shows the same initial decrease as did pure Al_2O_3 (Figure 5.3a) below 12°, which is caused by the scattering effects at near grazing take off angles. After 12°, the (Al 2p)/(O 1s) curve does not remain constant as found for pure Al_2O_3. The curve increases at $12° < \theta < 18°$, then slowly decreases at $18° < \theta < 24°$, followed by another increase at $24° < \theta < 28°$. After 28° the features become too small to identify. The increase at $12° < \theta < 18°$ indicates that more and more Al is sampled in this depth region, illustrating the existence of an Al-rich $HfAl_xO_y$ layer different from the layer defined by $18° < \theta < 24°$ region. From 18° to 24°, the (Al 2p)/(O 1s) ratio decreases because no more Al is detected in this depth region, defining an Al-free HfO_2 region. The increase at $24° < \theta < 28°$ implies another Al-rich $HfAl_xO_y$ layer under the Al-free HfO_2 layer. After 28° the trend of the curve becomes unresolvable because the probing depth (EAL × sin θ) is too deep that the periodicity is averaged. The (Al 2p)/(O 1s) curve for a 10 nm [5Hf + 1Al] × 21 shows the same trend as the 8:1 sample after 12°. The only difference is that the features appear over smaller angle ranges and move to the left because the repeated structure is thinner in this sample. The two increase segments at $11° < \theta < 15°$ and $20° < \theta < 24°$ represent two Al-rich

$HfAl_xO_y$ layers, separated by an Al-free HfO_2 layer that is represented by the decrease at $15° < \theta < 20°$. Inserting one ALD layer of Al_2O_3 after every five ALD layers of HfO_2 still ensures a periodic structure. Therefore the features after 12° in Figure 5.3b reveal a nonuniform structure composed of an Al-free HfO_2 layer sandwiched between two $HfAl_xO_y$ layers. Although the features disappear when the take off angle is too large, it is reasonable to conclude these two films possess periodic structures considering the layer-by-layer nature of ALD growth.

For the 10 nm [4Hf + 1Al] × 23 sample in Figure 5.3c, no apparent features are developed similar to those in Figure 5.3b. The curve does show some inflections, such as the increase around 22°. The error bars are significant at 7° and are smaller than the vertical line segments of the data symbols for take off angles ≥ 12°. Thus the feature at 22° represents an (Al 2p)/(O 1s) curve increase, which implies an Al concentration increase along the film growth direction. Compared with the two samples in Figure 5.3b, the [4Hf + 1Al] sample has thinner repeated layers, therefore its features on the (Al 2p)/(O 1s) curve should be compressed over smaller angle ranges and move to the left even more than [5Hf + 1Al]. The increase around 22° for the [4Hf + 1Al] sample might be the same feature as the increase shown at $20° < \theta < 24°$ and $24° < \theta < 28°$ for the [5Hf + 1Al] and [8Hf + 1Al] sample, respectively. Other possible features, which are the counterpart to the $11° < \theta < 15°$ feature for the [5Hf + 1Al] sample and the $12° < \theta < 18°$ feature for the [8Hf + 1Al] sample, are shifted to the left and abut the scattering-effect-dominant region and become unresolved. The increase at 22° implies periodic structures start to develop in the [4Hf + 1Al] × 23 sample, but have not completely formed.

Figure 5.3d shows the (Al 2p)/(O 1s) curves for the 10 nm [3Hf + 1Al] × 28 and [2Hf + 1Al] × 35 samples. No feature is observed except the initial decrease due to the scattering effects, implying these two samples are more like homogenous films. Based on this AR-XPS analysis, we conclude that Al-free HfO_2 layers start to develop when the Hf:Al ALD cycle ratio is four, and complete formation when the ratio equals five or larger, indicating the existence of periodic structures; while those smaller than four are more like homogeneous films.

5.3.3. Structure versus Thermal Stability

Knowing structural periodicity exists in films with high Hf:Al ALD cycles ratios ($\geq$ 5:1), the relationship between film structure and thermal stability was studied. The crystallization behavior of thin (10 nm) and thick (40 nm) pure HfO_2 films are shown in Figure 5.4. 10 nm HfO_2 is amorphous as deposited at 250°C, and remains amorphous up to 450 °C, and crystallizes into the monoclinic phase between 450°C and 500°C. The diffraction peaks at 2θ = 24.6, 28.5, 31.8, 35.6° can be assigned to the monoclinic phase, as marked in Figure 5.4a. With increasing thickness, HfO_2 is much easier to crystallize as the surface enthalpy contributes less to the total film energy. A 40 nm HfO_2 film crystallized into the monoclinic phase during growth at 250 °C. Annealing at 400 °C does not change the film phase, as shown in Figure 5.4b.

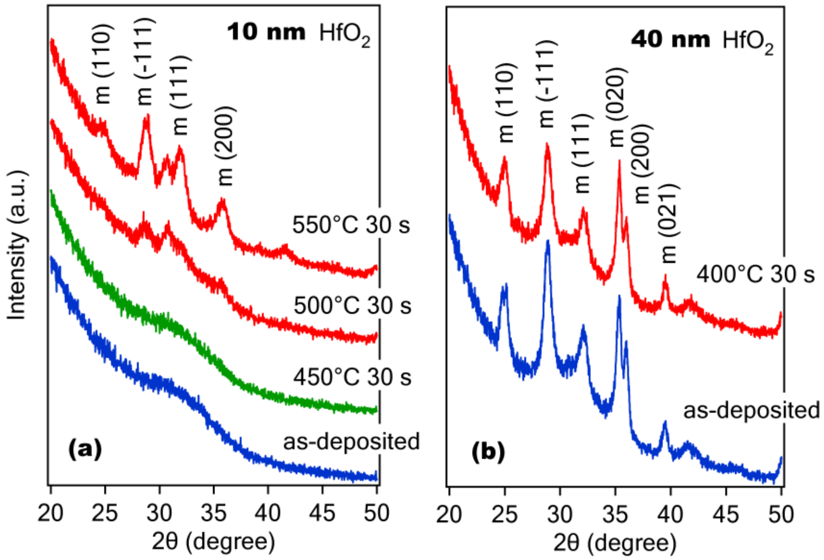

Figure 5.4. XRD spectra of (a) 10 nm as-deposited HfO_2 and HfO_2 annealed at 450, 500, and 550 °C; (b) 40 nm as-deposited HfO_2 and HfO_2 annealed at 400 °C.

For ALD-grown Al-HfO_2 films with a structure more like homogeneous films, the film thermal stability is highly affected by alloy composition and film thickness. The 10 nm and 40 nm [3Hf + 1Al] films show thickness dependent crystallization characteristics. The 10 nm [3Hf + 1Al] remains amorphous after 900 °C 30 s annealing, and crystallizes at 950 °C, as shown in Figure 5.5a. A 40 nm thick film with the same [3Hf + 1Al] composition loses its thermal stability after 900 °C 30 s annealing, as shown in Figure 5.5b. Similarly, a 10 nm [2Hf + 1Al] film is amorphous at 960 °C and crystallizes at 1000 °C; where as a 40 nm [2Hf + 1Al] film crystallizes at 960 °C (figure not shown).

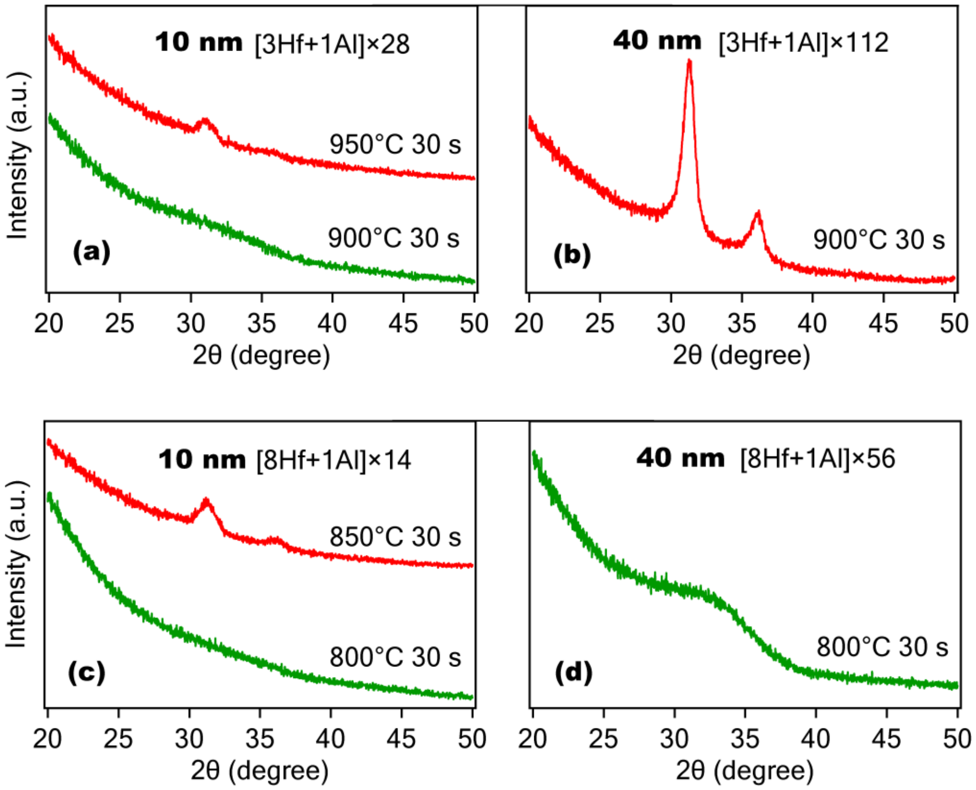

Figure 5.5. XRD spectra of (a) 10 nm and (b) 40 nm [3Hf + 1Al] films annealed at 900 °C (10 nm [3Hf + 1Al] is annealed at 950 °C for comparison); (c) 10 nm and (d) 40 nm [8Hf + 1Al] films annealed at 800 °C (10 nm [8Hf + 1Al] is annealed at 850 °C for comparison).

However, for films with a periodic structure, the thermal stability becomes independent of thickness up to 40 nm. A 10 nm [8Hf + 1Al] × 14 film remains amorphous after 800 °C 30 s annealing (Figure 5.5c), and this temperature is close to the critical temperature at which this film crystallizes. Unlike [3Hf + 1Al] films, a 40 nm [8Hf + 1Al] × 14 remains amorphous after 800 °C 30 s annealing, as shown in Figure 5.5d. This illustrates that, in addition to composition and thickness, the film structure also influences film thermal stability. ALD-grown films with periodic structures can withstand high temperature annealing for the thicker films, compared with homogeneous films.

This structure dependent amorphization effect is not limited to the Al-HfO_2 system; ALD-grown La-HfO_2 (La-incorporated HfO_2) films change their phase in the same way, as shown in Figure 5.6. Similar AR-XPS analysis shows that the [6Hf + 1La] films are composed of periodic $HfLa_xO_y$ and HfO_2 layers, while [3Hf + 1La] films are more like homogeneous films.[34] The 10 nm [3Hf + 1La] × 41 film remains amorphous after 900 °C 30 s annealing, but the 40 nm [3Hf + 1La] × 160 film crystallizes after annealing under identical conditions (Figure 5.6a and b). While both the 10 nm [6Hf + 1La] × 22 and the 40 nm [6Hf + 1La] × 84 films can withstand a 800 °C 30 s annealing (Figure 5.6c and d).

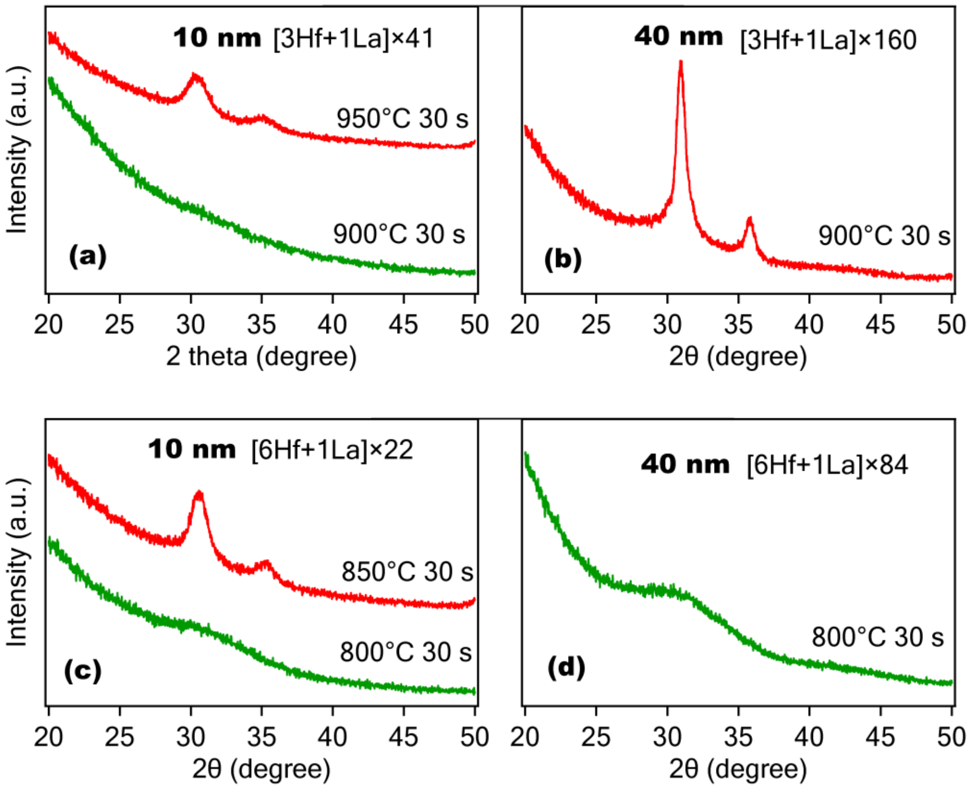

Figure 5.6. XRD spectra of (a) 10 nm and (b) 40 nm [3Hf + 1La] films annealed at 900 °C (10 nm [3Hf + 1La] is annealed at 950 °C for comparison); (c) 10 nm and (d) 40 nm [6Hf + 1La] films annealed at 800 °C (10 nm [6Hf + 1La] is annealed at 850 °C for comparison).

For homogeneous HfO_2-based ternary oxide thin films, there are two factors determining the film thermal stability: incorporated elements and overall film thickness. For instance, incorporating SiO_2, Al_2O_3, and La_2O_3 into HfO_2 is an effective method to increase the crystallization temperature,[8–22] and the crystallization temperature increases with higher incorporation levels. But for a fixed incorporated element concentration, thinner films have stronger thermal stability. In bulk materials, the crystalline phase is always thermodynamically more stable than the amorphous phase. However, amorphous phases usually have lower surface and interfacial energies in nanoparticles and thin films below some critical particle dimension or film thickness.[27,46,47] As homogeneous or homogeneous-like films (e.g., HfO_2, [3Hf + 1Al], [3Hf + 1La]) are made thinner, the surface energy contribution leads to a higher crystallization temperature, which makes the amorphous phase more stable. In other words, both film composition and overall film thickness affects the film thermal stability for homogeneous films.

One the other hand, thermal stability of an ALD-grown film with periodic structure tends to be independent of overall film thickness. A periodic structure can be considered as a stack composed of repeated ultrathin HfM_xO_y–HfO_2 layers (M stands for the incorporated element). In this study, the Al-HfO_2 films with high Hf:Al ALD cycle ratios are likely composed of repeated $HfAl_xO_y$–HfO_2 ultrathin layers since one ALD layer of Al_2O_3 only interacts with a limited number ALD layers of HfO_2, introducing numerous extra interfaces in the film. Although the surface enthalpy value of these interfaces may be different from that of the sample-air surface, the bulk energy may contribute less to the total energy in this case and the surface-to-volume ratio of an ultrathin layer is independent of film overall thickness. Thus the crystallization temperature may be independent of total film thickness.

Ultrathin HfO_2 layers may become another factor determining film thermal stability for periodic films. Ultrathin HfO_2 can withstand a higher annealing temperature than thick HfO_2 films, maybe even thick HfO_2 incorporated with a weak amorphizer. Knowing that one ALD Al_2O_3 layer interacts with a limited number of ALD HfO_2 layers (about four layers by AR-XPS in this study), it is safe to conclude that varying Hf:Al ALD cycle ratio will only change the thickness of HfO_2 ultrathin layers in repeated $HfAl_xO_y$–HfO_2 structures, while the local Al concentration in the $HfAl_xO_y$ ultrathin layers remains relatively constant, as long as the Hf:Al ALD cycle ratio is in the range ensuring the existence of the $HfAl_xO_y$–HfO_2 periodic structure. Thus the different crystallization temperatures of ALD-grown Al-HfO_2 films with different incorporation levels may essentially be determined by different thicknesses of ultrathin HfO_2 layers for periodic films, because HfO_2 layers are more likely to initiate the crystallization while $HfAl_xO_y$ layers tend to block the growth of the crystalline phase. As the thickness of $HfAl_xO_y$ and local Al concentration are fixed in all periodic [xHf + 1Al] films, we believe the different thicknesses of ultrathin HfO_2 layers in two periodic films, e.g. 10 nm [8Hf + 1Al] × 14 and [5Hf + 1Al] × 21, are the reason why the two films have different thermal stability. Therefore, tuning the thickness of the ultrathin host material in repeated layers might be an additional method to change the film crystallization temperature in various ALD-grown systems with a periodic structure.

5.4. SUMMARY

The relationship between the thermal stability and the film structure of ALD-grown Al-HfO_2 films are studied. 10 nm Al-HfO_2 films with 8:1 and 3:1 AL:Hf ALD cycle ratios can remain amorphous after 800 and 900 °C annealing, respectively. Films with an Al:Hf ALD cycle ratio larger than four are found to be composed of periodic $HfAl_xO_y$–HfO_2 structures; the films are more like homogeneous mixtures when this ratio is equal or less than three. For a [3Hf + 1Al] structure, increasing film thickness lowers the thermal stability since the film is more homogeneous-like and the surface energy, which prefers the amorphous phase, plays less contribution to the total energy in the thicker film than it does in the thinner film. For a [8Hf + 1Al] structure, the crystallization temperature is independent of film thickness because the surface-to-volume ratio remains constant as film thickness changes, which is caused by $HfAl_xO_y$–HfO_2 periodic structure. Therefore the periodically repeated structure in an ALD-grown film is also an important factor determining the film thermal stability.

5.5. REFERENCES

(1) Wilk, G. D.; Wallace, R. M.; Anthony, J. M. *J. Appl. Phys.* **2001,** *89*, 5243–5275.

(2) Gusev, E. P.; Cabral, C.; Copel, M.; D'Emic, C.; Gribelyuk, M. *Microelectron. Eng.* **2003**, *69*, 145–151.

(3) Kukli, K.; Aarik, J.; Uustare, T. Lu, J.; Ritala, M. Aidla, A.; Pung, L.; Harsta, A.; Leskela, M.; Kikas, A. Sammelselg, V. *Thin Solid Films* **2005**, *479*, 1–11.

(4) Kukli, K.; Pilivi, T.; Ritala, M.; Sajavaara, T.; Lu, J.; Leskela, M. *Thin Solid Films* **2005**, *491*, 328–338.

(5) Hausmann, D. M.; Kim, E.; Becker, J.; Gordon, R. G. *Chem. Mater.* **2002**, *14*, 4350–4358.

(6) Mommer, N.; Lee, T.; Gardner, J. A. *J. Mater. Res.* **2000**, *15*, 377–381.

(7) Zhao, X.; Vanderbilt, D. *Phys. Rev. B* **2002**, *65*, 233106/1–233106/4.

(8) Wilk, G. D.; Wallace, R. M.; Anthony, J. M. *J. Appl. Phys.* **2000**, *87*, 484–492.

(9) Tomida, K.; Kita, K.; Toriumi, A. *Appl. Phys. Lett.* **2006**, *89*, 142902/1–142902/3.

(10) Lehn, J.-S. M.; Javed, S.; Hoffman, D. M. *Chem. Vap. Deposition* **2006**, *12*, 280–284.

(11) Ohshita, Y.; Ogura, A.; Ishikawa, M.; Kada, T.; Hoshino, A.; Suzuki, T.; Machida, H.; Soai, K. *Chem. Vap. Deposition* 2006, *12*, 130–135.

(12) Park, T. J.; Kim, J. H.; Jang, J. H.; Na, K. D.; Hwang, C. S.; Yoo, J. H. *Electrochem. Sol. State. Lett.* 2008, *11*, H121–H123.

(13) Lee, D.; Suh, D.; Pae, Y.; Kim, H.; Cho, M.-H.; Ko, D.-H. *J. Electrochem. Soc.* **2007**, *154*, H708–H712.

(14) Sivasubramani, P.; Kim, J.; Kim, M. J.; Gnade, B. E.; Wallace, R. M. *J. Appl. Phys.* **2007**, *101*, 114108/1–114108/4.

(15) Hoppe, E. E.; Aita, C. R. *Appl. Phys. Lett.* **2008**, *92*, 141912/1–141912/3.

(16) Marshall, P. A.; Potter, R. J.; Jones, A. C.; Chalker, P.R.; Taylor, S.; Critchlow, G. W.; Rushworth, S. A. *Chem. Vap. Deposition* **2004**, *10*, 275–279.

(17) Song, M.-K.; Kang, S.-W.; Rhee, S.-W. *J. Electrochem. Soc.* **2005**, *152*, C108–C112.

(18) Ho, M. –Y.; Gong, H.; Wilk, G. D.; Busch, B. W.; Green, M. L.; Lin, W. H.; See, A.; Lahiri, S. K.; Loomans, M. E.; Raisanen, P. I.; Gustafsson, T. *Appl. Phys. Lett.* **2002**, *81*, 4218–4220.

(19) Cho, M.-H.; Chang, H. S.; Cho, Y. J.; Moon, D. W.; Min, K.-H.; Sinclair, R.; Kang, S. K.; Ko, D.-H.; Lee, J. H.; Gu, J. H. Lee, N. I. *Appl. Phys. Lett.* **2004**, *84*, 571–573.

(20) Yamamoto, Y.; Kita, K.; Kyuno, K.; Toriumi, A. Appl. Phys. Lett. 2006, 89, 032903/1–032903/3.

(21) Wang, T.; Ekerdt, J. G. *Chem. Mater.* **2009**, *21*, 3096–3101.

(22) Huang, L.-Y.; Li, A.-D.; Zhang, W.-Q.; Li, H.; Xia, Y.-D.; Wu, D. *Appl. Surf. Sci.* **2010**, *256*, 2496–2499.

(23) Toriumi, A.; Kita, K. Material Engineering of High Gate Dielectrics. In *Dielectric Films for Advanced Microelectronics;* Baklanov, M., Green, M., Maex, K., Eds.; John Wiley & Sons, 2007; Chapter 7, pp 321–324.

(24) Inoue, H.; Utsuno, F.; Yasui, I. *J. Non-Cryst. Solids.* **2004**, *349*, 16–21.

(25) Lucovsky, G.; Whitten, J. L. Electronic Structure of Alternative High-*k* Dielectrics. In *High Dielectric Constant Materials: VLSE MOSFET Applications*; Huff, H. R., Gilmer, D. C., Eds.; Springer, 2005; Chapter 11, pp 322–327.

(26) Lee, C.-K.; Cho, E.; Lee, H.-S.; Hwang, C. S.; Han, S. *Phys. Rev. B* **2008**, *78*, 012102/1–012102/4.

(27) Ushakov, S. V.; Brown, C. E.; Navrotsky, A. *J. Mater. Res.* **2004**, *19*, 693–696.

(28) Yang, Z. K.; Lee, W. C.; Lee, Y. J. Chang, P.; Huang, M. L. Hong, M. *Appl. Phys. Lett.* **2007**, *91*, 202909/1–202909/3.

(29) Majumder, P.; Jursich, G.; Takoudis, C. *J. Appl. Phys.* **2009**, *105*, 104106/1–104106/6.

(30) Craciun, D.; Socol, G.; Axente, E.; Calca, A.-C.; Singh, R.; Craciun, V. Mater. Res. Soc. Proc. 2008, 1074, 1074–I03–18.

(31) Essary, C. R.; Ramani, K.; Craciun, V.; Singh, R. K.; *Appl. Phys. Lett.* **2006**, *88*, 182902/1–182902/3.

(32) Cho, M.-H.; Roh, Y. S. Whang, C. N.; Jeong, K.; Nahm, S. W.; Ko, D.-H.; Lee, J. H.; Lee, N. I.; Fujihara, K. *Appl. Phys. Lett.* **2002**, *81*, 472–474.

(33) Navrotsky, A. *J. Mater. Chem.* **2005**, *15*, 1883–1890.

(34) Wang, T.; Ekerdt, J. G. *Chem. Mater.* **2010**, *22* , 3798–3806.

(35) Katamreddy, R.; Inman, R.; Jursich, G.; Soulet, A.; Takoudis, C. *Acta Mater.* **2008**, *56*, 710–718.

(36) Moulder, J. F.; Stickle, W. F.; Sobol, P. E.; Bomben, K. D. *Handbook of X-ray Photoelectron Spectroscopy*; Physical Electronics, Inc.: Eden Prairie, MN, 1995.

(37) Zhu, W. J.; Tamagawa, T.; Gibson, M.; Furukawa, T.; Ma, T. P. *IEEE Electron. Device. Lett*. **2002**, *23*, 649–651.

(38) Streetman, B. G.; Banerjee, S. K. *Solid State Electronic Devices*; 6th Editio.; Prentice Hall: Upper Saddle River, NJ, 2006; p. 154–168, 269–270.

(39) Cho, M.-H.; Roh, Y. S.; Whang, C. N.; Jeong, K.; Choi, H. J.; Nam, S. W.; Ko, D.-H.; Lee, J. H.; Lee, N. I.; Fujihara, K. *Appl. Phys. Lett.* **2002**, *81*, 1071–1073.

(40) Toriumi, A.; Iwamoto, K.; Ota, H.; Kadoshima, M.; Mizubayashi, W.; Nabatame, T.; Ogawa, A.; Tominaga, K.; Horikawa, T.; Satake, H. *Microelectronic Engineer.* **2005**, *80*, 190–197.

(41) Champaneria, R.; Mack, P.; White, R.; Wolstenholme, J. *Surf. Interface Anal.* **2003**, *35*,1028–1033.

(42) Mack, P.; White, R. G.; Wolstenholme, J.; Conard, T. *Appl. Surf. Sci.* **2006**, *252*, 8270–8276.

(43) Chang, J. P.; Green, M. L.; Donnelly, V. M.; Opila, R. L.; Eng, J., Jr.; Sapjeta, J.; Silverman, P. J.; Weir, B.; Lu, H. C.; Gustafsson, T.; Garfunkel, E. *J. Appl. Phys.* **2000**, *87*, 4449–4455.

(44) Powell, C. J.; Jablonski, A. *NIST Electron Effective-Attenuation-Length Database*-Version 1.0, National Institute of Standards and Technology: Gaithersburg, MD, 2001.

(45) Kimura, K.; Nakajima, K.; Conard, T.; Vandervorst, W. *Appl. Phys. Lett.* **2007**, *91*, 104106/1–104106/3.

(46) Molodetsky, I.; Navrotsky, A.; Paskowitz, M. J.; Leppert, V. J.; Risbud, S. H. *J. Non-Cryst. Solids* **2000**, *262*, 106–113.

(47) Pitcher, M. W.; Ushakov, S. V.; Navrotsky, A. *J. Amer. Cer. Soc.* **2005**, *88*, 160–167.

Chapter 6: The Relationship between Film Structure and Enhanced Thermal Stability of Ta_2O_3-Incorporated HfO_2 Grown by Atomic Layer Deposition

6.1. INTRODUCTION

Extensive effort has been made to stabilize the amorphous phase of HfO_2, which is a potential high-*k* dielectric material to replace conventional SiO_2 because of its high dielectric constant (~ 20), high bandgap (~ 5.5 eV) and relatively good stability on silicon.[1–5] As-deposited amorphous HfO_2 tends to crystallize at a relatively low temperature (~ 500 °C),[2] introducing grain boundaries in the film that may serve as charge leakage paths, and the coexistence of monoclinic and tetragonal phases in a polycrystalline film may lead to a spatially varying dielectric constant.[6] Thus it is desirable to find methods to stabilize the amorphous phase of HfO_2 under high temperature annealing conditions in the device fabrication process, although crystalline HfO_2 has a higher dielectric constant.

Incorporating a robust amorphous oxide into HfO_2 has been shown to effectively enhance the thermal stability of the dielectric film. The most well-researched HfO_2-based ternary oxides are $HfSi_xO_y$[7–10] and $HfAl_xO_y$.[11–16] But the dielectric constant of these films decreases, although SiO_2 and Al_2O_3 are very strong amorphizers. To retain the high-*k* nature of the film, oxides with higher dielectric constants, such as La_2O_3,[17–20] and Ta_2O_5,[21,22] are looked to as amorphizers for HfO_2. Ta_2O_5 has a *k* value of ~ 27,[23] which is even higher than that of amorphous and monoclinic HfO_2 (~ 16).[24] Thus we expect Ta-incorporated HfO_2 films with an enhanced thermal stability will eventually have an increased dielectric constant.

The concentration of the incorporated element is a well-known factor determining the film crystallization temperature in HfO_2-based ternary oxides. However, the distribution (in the growth direction) of the incorporated element might be another important factor to stabilize the amorphous phase, which has been rarely studied because most ternary films grown by techniques such as chemical vapor deposition (CVD) or cosputtering naturally lead to homogeneous films.

Atomic layer deposition (ALD), which ensures atomic-level thickness control as the film grows linearly with the number of ALD cycles, has emerged as a promising method to grow high quality ternary thin films.[25] Besides thickness control, as-deposited ALD-grown ternary films may have another favorable characteristic when compared with CVD-grown or sputtered films. One ALD cycle will not grow a complete monolayer of materials. For example, the coverage rate of ALD-grown HfO_2 is about 30% monolayer coverage/cycle.[26] When applying ALD to grow a ternary oxide, one ALD layer of the incorporated oxides can be inserted between a particular number of ALD host oxide layers to achieve the target overall incorporation level.[19,27] In this case, the film is neither a homogeneous mixture nor a true nanolaminate with clear layer interfaces, especially when the ALD cycle ratio of the host oxide to the incorporated oxide is high. We have shown that ALD-grown La (Chapter 3) and Al-incorporated HfO_2 (Chapter 5) with low overall La and Al concentrations are composed of repeated HfO_2–$HfLa_xO_y$ and HfO_2–$HfAl_xO_y$ structures, where ultrathin HfO_2 layers are sandwiched between $HfLa_xO_y$ or $HfAl_xO_y$ layers.[28,29] We believe the film structure, namely the existence of extra HfO_2–HfM_xO_y (M = incorporated element) interfaces and ultrathin HfO_2 layers, may add extra influences on the film thermal stability, in addition to the overall amorphizer incorporation concentration.

In this study, Ta-incorporated HfO_2 (Ta-HfO_2) films are grown by repeatedly inserting one ALD layer of Ta_2O_5 into a particular number of ALD HfO_2 layers, to explore the thermal stability enhancement of Ta-incorporation, and evaluate the electric properties of ALD-grown Ta-HfO_2 films. Nanolaminate films composed of clearly defined HfO_2–$HfTa_xO_y$ structures (known thickness for HfO_2 and $HfTa_xO_y$ layers and known local Ta concentration in $HfTa_xO_y$) are grown to study the relationship between film structure and thermal stability, and determine whether crystallization starts from the HfO_2 layers or the $HfTa_xO_y$ layers. Since Ta-HfO_2 with one inserted ALD Ta_2O_5 layer are likely composed of HfO_2–$HfTa_xO_y$ structures when the ALD layers of HfO_2 between every Ta_2O_5 are large enough, the crystallization mechanism can be analytically understood when compared with the crystallization of nanolamiante films.

6.2. EXPERIMENTAL DETAILS

Samples are deposited on n-Si(100) substrates at 250 °C using tetrakis (ethylmethylamino) hafnium $Hf[N(CH_3)(C_2H_5)]_4$, tris(diethylamino)(ethylimino) tantalum, $Ta(NC_2H_5)(N(C_2H_5)_2)_3$ and H_2O; the precursors are held at 85, 95, and 25 °C, respectively. A detailed ALD reactor description is reported elsewhere.[19] One ALD cycle consists of metal precursor dosing for 1.5 s (Hf or Ta), a 25 s purge with Ar, water dosing for 0.06 s, and a 25 s purge with Ar. The adsorption of both $Hf[N(CH_3)(C_2H_5)]_4$ and $Ta(NC_2H_5)(N(C_2H_5)_2)_3$ have been proved to be self-limiting processes at 250 °C.[30,31] HfO_2 and Ta_2O_5 both grow linearly with the number of ALD cycles in our ALD system, with the growth rate of 0.78 and 0.49 Å/cycle, respectively. The Si substrates are etched in a 1% HF solution for 40 s to remove native oxide, then rinsed in deionized water for 30 s, which reoxidizes the Si(100) surface, and dried with flowing He. The resultant oxide is 10 Å according to ellipsometry.

The Ta-incorporation is achieved by growing HfO_2 and Ta_2O_5 alternately; one ALD layer of Ta_2O_5 is added after x ALD layers of HfO_2, and then this sequence is repeated n times to achieve the desired thickness. Films are referenced using [xHf + 1Ta] × n. Film growth always ends with an xHf cycle. One "ALD layer" does not imply a complete monolayer of a particular material, and we refer to an ALD layer as the amount deposited in a single cycle. To study the influence of film structure on film thermal stability, HfO_2–$HfTa_xO_y$ nanolaminate is also grown. The local Ta concentration in the $HfTa_xO_y$ layer is fixed as all $HfTa_xO_y$ are grown with repeated [1Hf + 1Ta] sequences.

The compositional, thermal, and electrical properties of selected [xHf + 1Ta] × n films and HfO_2–$HfTa_xO_y$ nanolaminates are studied using X-ray photoelectron spectroscopy (XPS), X-ray diffraction (XRD), and C–V/I–V measurements. In situ XPS is performed for as-deposited [xHf + 1Ta] × n samples using a Physical Electronics 5500 XPS system with an Al $K\alpha$ source at 1486.6 eV. To investigate the crystallinity of sample after annealing, grazing incidence XRD (GIXRD) is performed at a fixed 0.5° incident angle, using a Bruker-AXS D8 Advance Powder Diffractometer with a sealed tube Cu $K\alpha$ radiation. Prior to XRD, samples are annealed under a rapid thermal annealing (RTA) process at different temperatures for 30 s under a N_2 environment. Metal-insulator-semiconductor (MIS) capacitors are made by sputtered TaN. The area of TaN contact is defined by a shadow mask, and measured with a Zeiss Axioskop 2 MAT optical microscope. Film dielectric constant is determined by the accumulation capacitance from 100 kHz C–V measurements, and the film leakage current density is measured from the I–V measurements, using a Keithley 590 CV Analyzer and a Keithley 4200 Semiconductor Characterization System.

6.3. RESULTS AND DISCUSSION

6.3.1. XPS Analysis of As-Deposited 10 nm [*x*Hf + 1Ta] Films

Figure 6.1 shows the XP spectra of Ta 4f, O 1s, and Hf 4f peaks for as-deposited 10 nm [*x*Hf + 1Ta] × *n* (*x* = 1, 4, and 8), Ta_2O_5, and HfO_2. Baseline subtraction is carried out using PeakFit (Version 4) software for Ta 4f and Hf 4f, and all spectra are referenced to C 1s peak at 285 eV. The C contamination is introduced to the film surface when transferring the as-deposited samples from the ALD chamber to the XPS analysis chamber through a load lock. After a 5 kV Ar^+ sputtering over a 2 × 2 mm^2 area for 40 s, which removes about 2 nm of topmost surface, no C 1s peak is detected in the bulk film.

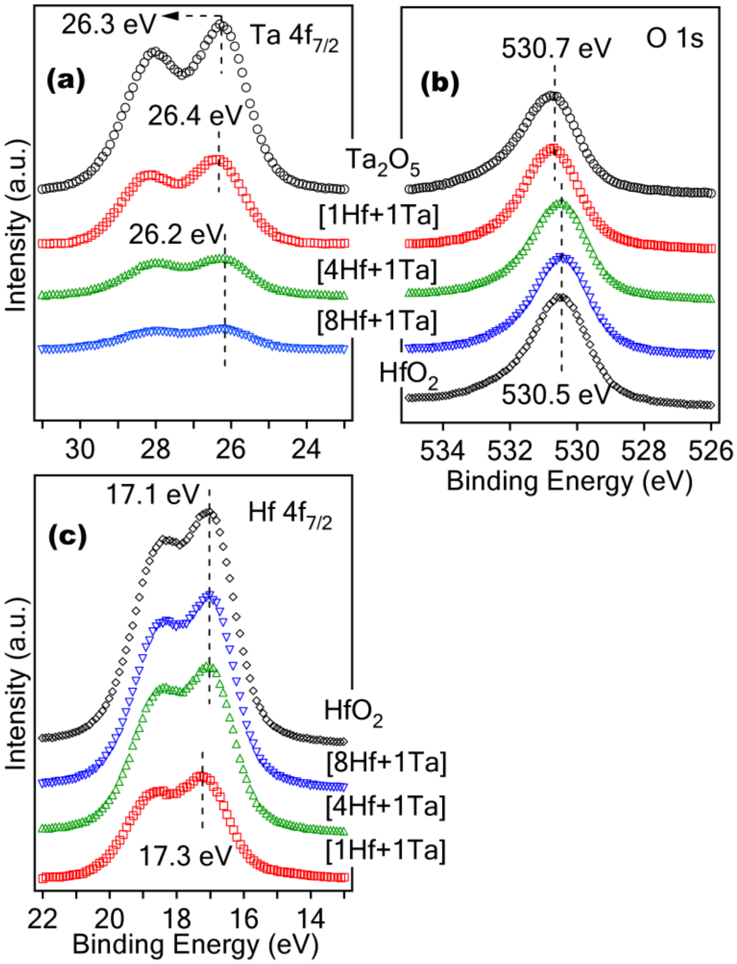

Figure 6.1. XP spectra of Ta 4f, O 1s, and Hf 4f peaks for as-deposited 10 nm [*x*Hf + 1Ta] × *n* (*x* = 1, 4, and 8), Ta_2O_5, and HfO_2.

As shown in Figure 6.1a, the Ta $4f_{7/2}$ peak of Ta_2O_5 appears at 26.3 eV, which is typical for fully-oxidized stoichiometric Ta_2O_5.[32–34] For [*x*Hf + 1Ta] × *n* (*x* = 1, 4, and 8) samples, the Ta 4f peaks are located at 26.3 ± 0.1 eV, indicating that the incorporated Ta is fully oxidized in the [*x*Hf + 1Ta] × *n* films. The O 1s peaks in Figure 6.1b are located at 530.5 eV for HfO_2, [8Hf + 1Ta] and [4Hf + 1Ta], and at 530.7 eV for [1Hf + 1Ta] and Ta_2O_5. The two positions are close to the binding energy of O 1s in HfO_2 (530.4 eV) and

Ta_2O_5 (530.6 eV) bulk materials,[35] and are commonly observed for thin films of HfO_2 and Ta_2O_5.[34,36–38] In Figure 6.1c, the Hf $4f_{7/2}$ peaks are located at 17.1 and 17.3 eV, with a 0.2 eV shift from the HfO_2 and lower-incorporated [8Hf + 1Ta] and [4Hf + 1Ta] films to higher-incorporated [1Hf + 1Ta] films. The location of the Hf $4f_{7/2}$ peaks agree with fully oxidized HfO_2.[36] The 0.2 eV shift to the higher binding energy can be attributed to the presence of dissimilar metals in mixed metal oxides,[39] where the cation of the more ionic metal (Hf^{4+} in this case) becomes more ionic. A similar shift of Hf $4f_{7/2}$ is reported for Ta-HfO_2 grown by cosputtering.[22]

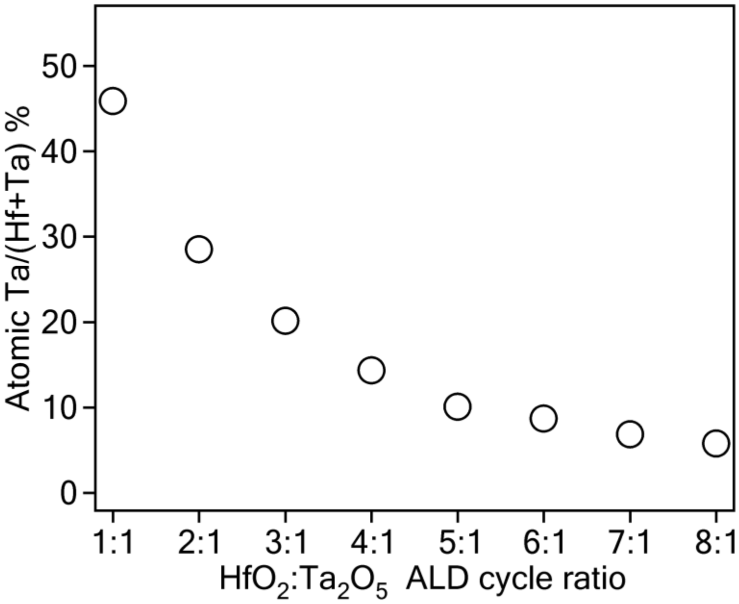

Figure 6.2. Atomic Ta-incorporation concentration of as-deposited Ta-HfO_2 versus HfO_2:Ta_2O_5 ALD cycle ratio.

The atomic Ta-incorporation concentrations, Ta/(Hf + Ta), for as-deposited 10 nm [*x*Hf + 1Ta] × *n* (*x* = 1–8) films are calculated from the peak area of Ta 4f and Hf 4f, corrected by their corresponding atomic sensitivity factors.[40] The Ta-incorporation concentration can be effectively controlled by varying the HfO_2:Ta_2O_5 ALD cycle ratio, from 46 to 5.8% when x increases from 1 to 8. Ta-incorporation of 46% in the [1Hf + 1Ta] sample indicates that less $Ta(NEt)(NEt_2)_3$ precursor molecules are adsorbed onto the surface than $Hf[N(CH_3)(C_2H_5)]_4$ during each metal precursor dosing step because of the greater steric hindrance of the Ta precursor molecules.

The atomic Ta/(Hf + Ta) concentration of the [4Hf + 1Ta] sample is 14.3%. The Hf $4f_{7/2}$ peak in a homogeneous Ta-HfO_2 film grown by cosputtering with a lower Ta-incorporation level (Ta/(Hf + Ta) = 10%) shows a 0.2 eV shift with regard to HfO_2, whereas the [4Hf + 1Ta] in this study does not show any Hf $4f_{7/2}$ shift (Figure 6.1c). We have shown that La_2O_3 and Al_2O_3 interact with a limited number of ALD HfO_2 layers in ALD-grown La-HfO_2 and Al-HfO_2.[28,29] Similarly, it is possible that not all 4 ALD HfO_2 layers are intermixed with Ta_2O_5 in an as-deposited [4Hf + 1Ta] film and is not as true an alloy as the film grown by cosputtering. Thus the binding energy shifting is less significant in as-deposited ALD-grown Ta-HfO_2 films.

6.3.2. Thermal Stability of 10 nm [*x*Hf + 1Ta] Films

The crystallization onset temperatures of 10 nm HfO_2 and Ta_2O_5 are illustrated in Figure 6.3a and b. The 10 nm HfO_2 film can remain amorphous up to 450 °C, and crystallizes after the 500 °C annealing for 30 s in a N_2 ambient. The diffraction peaks at $2\theta = 24.6, 28.5, 31.8, 35.6°$ can be assigned to the monoclinic phase, as marked in Figure 6.3a. The peak at 30.7° can be assigned to tetragonal (111) of HfO_2, which is a metastable phase at room temperature, but may be stabilized by film stress and/or grain size effects.[41,42] The tetragonal (111) peak can not be observed for a 40 nm crystallized film grown at the same condition (figure not shown). Thus 10 nm HfO_2 crystallizes mainly into the monoclinic phase, with a portion of the tetragonal phase, between 450 and 500 °C. The relatively low crystallization temperature of HfO_2 can be attributed to the fact that amorphous HfO_2 forms a random close packed (RCP) structure, which is basically determined by the oxygen atom packing.[43] Ta_2O_5 forms a modified continuous random network (MCRN) structure, in which metal atom ionic bonds disrupt and modify the covalently bonded continuous random network (CRN) structure,[44] and has a higher thermal stability compared with HfO_2. The as-deposited 10 nm ALD-grown Ta_2O_5 film is amorphous, and can withstand 750 °C RTA process for 30 s, as shown in Figure 6.3b. After annealing at 800 °C for 30 s, Ta_2O_5 crystallizes into the orthorhombic (β-Ta_2O_5) phase,[45–48] and the three peaks can be assigned to orthorhombic (001), (200), and (201), respectively, as marked in Figure 6.3b.

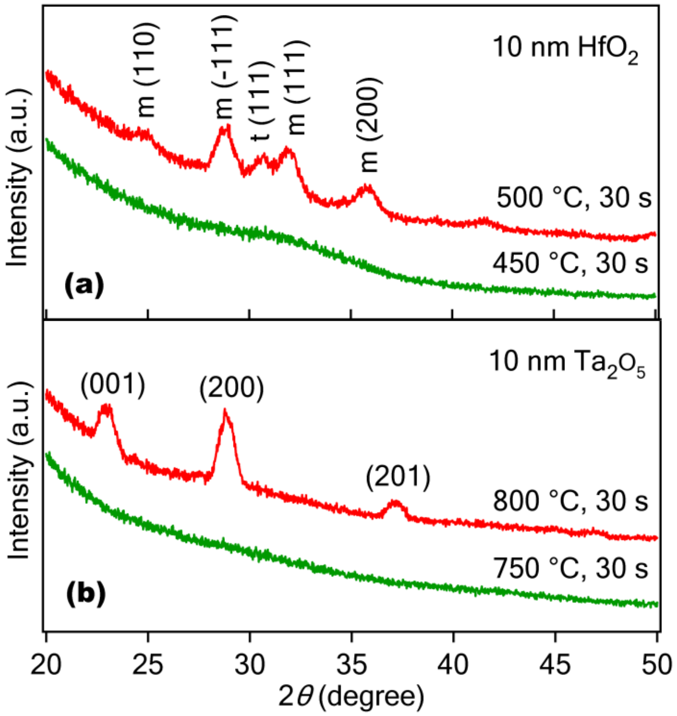

Figure 6.3. XRD spectra of 10 nm (a) HfO_2 annealed at 450 and 500 °C, and (b) Ta_2O_5 annealed at 750 and 800 °C for 30 s in a N_2 ambient.

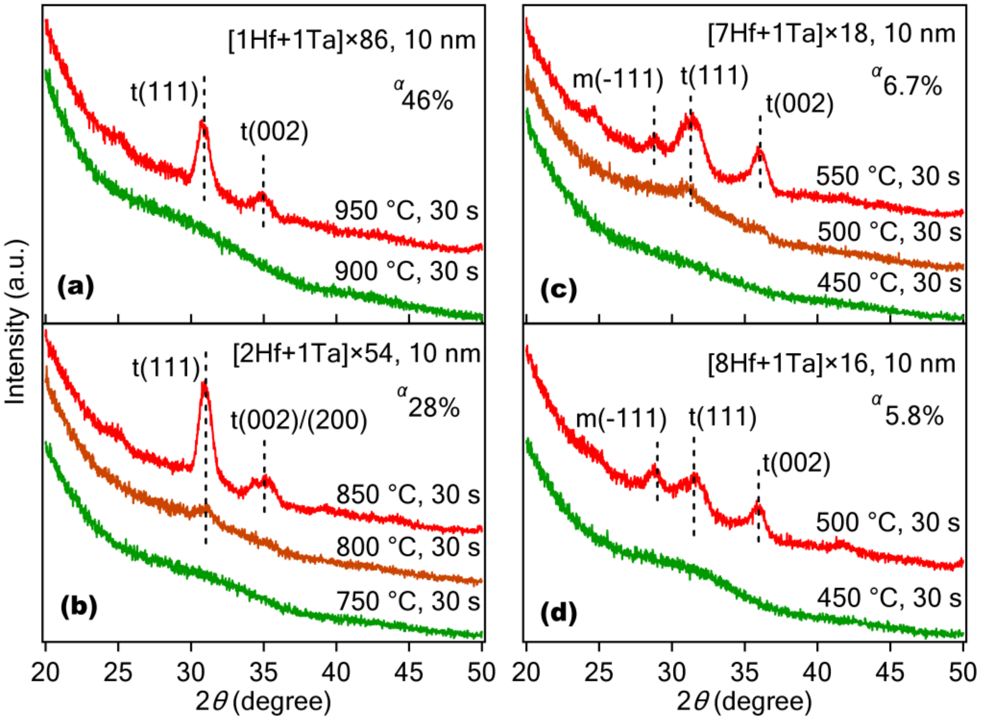

Figure 6.4. XRD spectra of 10 nm [*x*Hf + 1Ta] (x = 1, 2, 7, and 8 from (a) to (d), respectively, after various annealing temperatures for 30 s in a N_2 ambient. $^{\alpha}$Atomic Ta/(Hf + Ta)%.

Figure 6.4 shows the XRD patterns of four representative 10 nm [*x*Hf + 1Ta] (x = 1, 2, 7, and 8) samples annealed around their crystallization onset temperatures. In Figure 6.4a, a 10 nm [1Hf + 1Ta] film remains amorphous up to 900 °C, and crystallizes at 950°C. In Figure 6.4b, a 10 nm [2Hf + 1Ta] film remains amorphous up to 750°C, and slightly crystallizes at 800 °C, where a weak XRD peak at $2\theta = 30.9°$ is detected. After an 850 °C 30 s annealing, the 10 nm [2Hf + 1Ta] film is fully crystallized. Crystallized [1Hf + 1Ta] and [2Hf + 1Ta] films show a stronger and a weaker peak at 2θ = 30.9 and 35.0°, respectively, which can be assigned to the (111) and (002) planes for tetragonal HfO_2. The cubic phase of HfO_2 shows two similar peaks at around 31 and 35°.[49]

Although definite phase identification is not possible because only two peaks are clearly visible in the XRD pattern, theoretical calculations based on density functional methods predicts that Ta-incorporation stabilizes the tetragonal phase over the cubic phase.[50] Moreover, the double-peaked structure around 35° of the 10 nm [2Hf + 1Ta] film under 850 °C 30 s annealing (top curve in Figure 6.4b) suggests a (200)/(002) splitting, confirming the presence of the tetragonal phase rather than the cubic phase.[51]

For fully crystallized 10 nm [xHf + 1Ta] with $x = 1–4$ (Ta/(Hf + Ta) = 46–13%), all the samples have similar XRD patterns at $2\theta = 31$ and 35°. But for $x = 5–8$ (Ta/(Hf + Ta) = 10–5.8%), the crystallized 10 nm [xHf + 1Ta] films display the diffraction feature at $2\theta = 30.9$ and 36.0°, which can also be assigned to tetragonal (111) and (002) for HfO_2. With lower Ta-incorporation concentration (larger x value), the tetragonal (002) peak shows a 1.0° shift towards larger 2θ values, which implies the reduction of the lattice parameter according to Bragg's law. Such a noticeable peak shift was not observed for La and Al-incorporated HfO_2 in our previous studies (Chapter 2 and 5),[19,29] where the XRD peaks of the crystallized [xHf + 1La] film with $x = 2–8$ (La/(Hf + La) = 32–10%) and the crystallized [xHf + 1Al] film with $x = 4–9$ (Al/(Hf + Al) = 25–12%) always appear at $2\theta = 31$ and 36°.

A third peak appears at $2\theta = 28.8°$ for fully crystallized [7Hf + 1Ta] and [8Hf + 1Ta], as shown in Figure 6.4c and d, respectively. This peak can be assigned to monoclinic (-111) for HfO_2, the strongest peak of HfO_2 grown in our system, as shown in Figure 6.3a. Thus [xHf + 1Ta] films with lower La-incorporation levels ($x = 7$ and 8) crystallize into a mixture of tetragonal and monoclinic phases, whereas the higher-incorporated films crystallize in into the tetragonal phase.

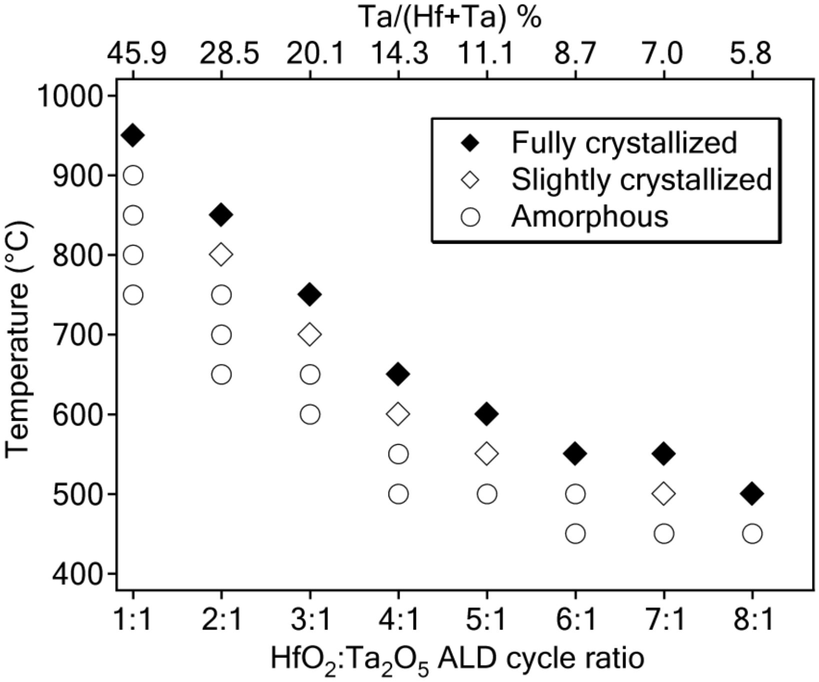

Figure 6.5. Crystallization onset temperatures for 10 nm [*x*Hf + 1Ta] × *n* samples (x = 1–8).

Figure 6.5 shows the summary of crystallization onset temperatures for a set of 10 nm [*x*Hf + 1Ta] × *n* samples (*x* =1–8) determined from XRD, with 50 °C heating increments. For XRD patterns like 800 °C annealed [2Hf + 1Ta] (Figure 6.4b) and 500 °C annealed [7Hf + 1Ta] (Figure 6.4c), the samples are classified as slightly crystallized (marked as open diamond) because an extra 50 °C annealing will result in clearer XRD patterns, indicating fully crystallization (marked as closed diamond). The crystallization onset increases with higher Ta-incorporation concentration (smaller *x*) from the 8:1 ratio sample to the 1:1 ratio sample, and the thermal stability of a 10 nm [1Hf + 1Ta] film (Ta/(Hf + Ta) = 46%) is higher than both 10 nm HfO_2 and Ta_2O_5.

6.3.3. Dielectric Constant and Leakage Current Density of [2Hf + 1Ta] Films

The dielectric constant (*k*) of as-deposited [2Hf + 1Ta] films is calculated from the slope of capacitance equivalent thickness (CET) versus physical thickness curve in Figure 6.6. (This film was selected for study since it remained amorphous up to 750 °C for a 10 nm film). The CET is determined from the accumulation capacitance of the C–V curves (not shown) and the physical thickness is measured by ellipsometry (including the interfacial layer). From linear fitting, the dielectric constant of as-deposited [2Hf + 1Ta] is 21.5 ± 0.4. The HfO_2 films grown in our previous study (Chapter 2) had a dielectric constant of 16.7.[19] Ta_2O_5 has a reported *k* value of ~ 27.[23] Thus ALD-grown Ta-HfO_2 film has a higher dielectric constant than HfO_2, at a Ta concentration of 28% (metal basis) for [2Hf + 1Ta].

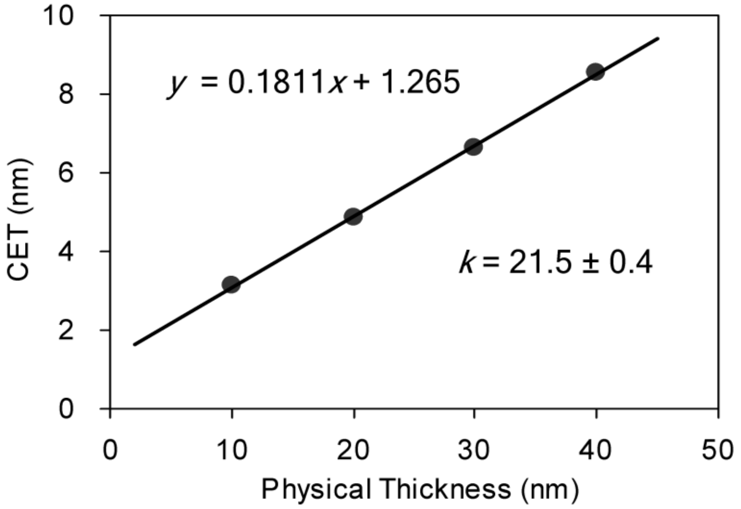

Figure 6.6. CET as a function of as-deposited [2Hf + 1Ta] film thickness. The solid line is the linear fit.

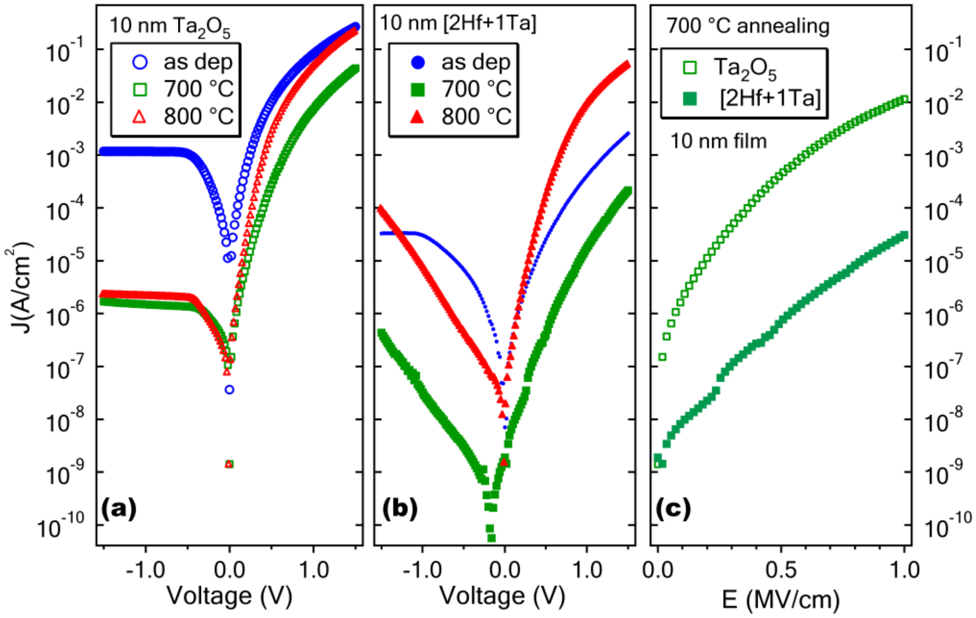

Figure 6.7. Leakage current density (*J*) versus voltage of (a) 10 nm Ta$_2$O$_5$ and (b) 10 nm [2Hf + 1Ta], as-deposited, after 700 and 800 °C 30 s annealing; (c) leakage current density (*J*) versus electric filed (*E*) of 10 nm Ta$_2$O$_5$ and [2Hf + 1Ta] after 700 °C 30 s annealing.

Figure 6.7a and b compare the leakage current density of 10 nm Ta$_2$O$_5$ and [2Hf + 1Ta] on an n-Si substrate. Both 10 nm Ta$_2$O$_5$ and [2Hf + 1Ta] films can remain amorphous up to 750 °C (Fugure 6.3b and 6.4b). The high leakage current density of as-deposited Ta$_2$O$_5$ has been associated with oxygen vacancies and/or impurities in the film,[47,52] which can be reduced using various post deposition annealing processes.[47,48,52,53] Ellipsometry revealed that Ta$_2$O$_5$ and [2Hf + 1Ta] films decreased from 10.3 nm to 10.1 nm and from 10.0 nm to 9.5 nm, respectively, for annealing at 800 °C. After a 700 °C RTA process in N$_2$ for 30 s, the leakage current density of Ta$_2$O$_5$ decreases because of the likely densification of the amorphous film. Similarly, the leakage current density of an as-deposited [2Hf + 1Ta] film deceases after a 700 °C RTA process. After an 800 °C RTA process, the leakage current density in 10 nm Ta$_2$O$_5$ increases somewhat because of a film phase change as crystallization introduces grain boundaries that may serve as leakage paths. In contrast, the [2Hf + 1Ta] sample crystallizes after the 800 °C RTA process and the leakage current density is greater than a nonannealed film (Figure 6.7b).

The leakage current density of the [2Hf + 1Ta] film is always lower than that of the Ta_2O_5 film. Figure 6.7c compares the leakage current density versus electric field for amorphous 10 nm Ta_2O_5 and [2Hf + 1Ta] films after a 700 °C RTA process. At 1 MV/cm, the leakage current density of the [2Hf + 1Ta] film is about three orders of magnitude lower than the Ta_2O_5 film. The leakage current density of a 10 nm amorphous HfO_2 film after a 400 °C RTA process (not shown) is lower than the 700 °C RTA-processed [2Hf + 1Ta] film, with values of 5.9×10^{-6} and 3.1×10^{-5} A/cm^2 at 1 MV/cm field, respectively. We suggest that the [2Hf + 1Ta] film out-performs the Ta_2O_5 film in Figure 6.7c because the HfO_2 properties are dominant at this composition.

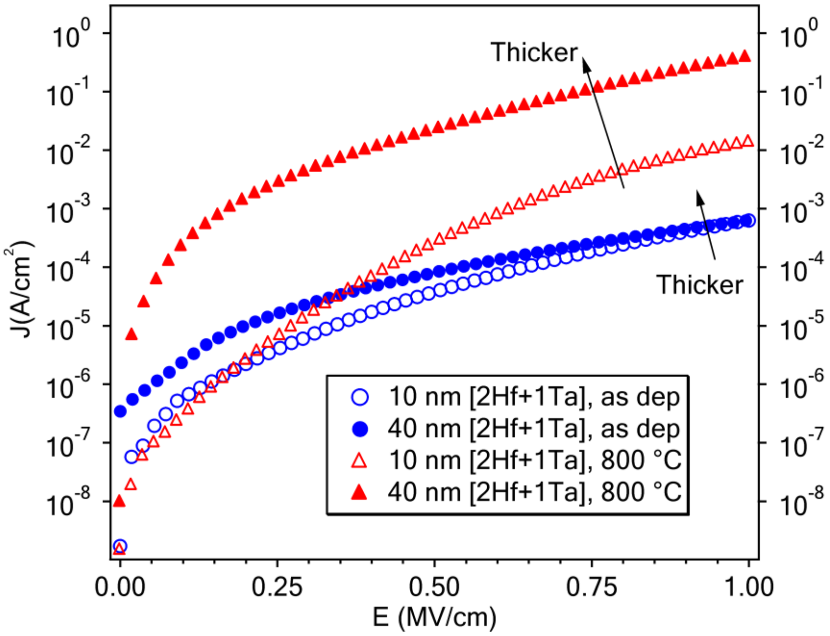

Figure 6.8. Leakage current density (J) versus electric filed (E) of as-deposited thinner (10 nm) and thicker (40 nm) [2Hf + 1Ta], and 800 °C annealed thinner (10 nm) and thicker (40 nm) [2Hf + 1Ta].

It has been found that overall film thickness affects the thermal stability of HfO_2-based oxide films containing homogeneously incorporated amorphizing elements. Generally, thicker films crystallize at a lower temperature. 10 nm [3Hf + 1Al] and [3Hf + 1La] films can remain amorphous after 900 °C 30 s annealing. Upon increasing film thickness to 40 nm, both [3Hf + 1Al] and [3Hf + 1La] crystallize during 900 °C annealing for 30 s.[29] The thermal stability of [2Hf + 1Ta] films, which are more like homogeneous mixtures, show the same thickness dependent characteristic; a 10 nm-thick film is slightly crystallized (Figure 6.4b) and a 40 nm-thick film is fully crystallized (not shown) after 800 °C RTA processing. Figure 6.8 presents leakage current density versus electric field for 10 and 40 nm amorphous and slightly/fully crystallized [2Hf + 1Ta] films. The amorphous films have a similar leakage current density at a 1 MV/cm field. The leakage current density increases with the increasing degree of crystallization for the 800 °C RTA-processed films. Therefore, annealing [2Hf + 1Ta] to a temperature below the onset of crystallization (Figure 6.7b) improves the leakage properties, whereas the introduction of crystalline domains negatively impacts the leakage properties.

6.3.4. Relationship between Film Structure and Thermal Stability

We have shown an ALD-grown amorphous [6Hf + 1La] × 21 film with a periodic structure requires a lower La-incorporation level to sustain 800 °C annealing compared with homogeneous film grown by cosputtering.[19] The periodic structure here refers to a layered film with HfO_2-only layers separated by $HfLa_xO_y$ or $HfTa_xO_y$ layers. To explore the relationship between film structure and thermal stability, we grew a series of periodic and nanolaminate structures with equivalent compositions. We also change the film designation to facilitate presenting the results. A {5Hf + [1Hf + 1Ta] × 5} × 10 film refers to 5 Hf-only cycles and a growth sequence of 5 [1Hf + 1Ta] ALD cycles, i.e., 1 Hf cycle followed by 1 Ta cycle to produce a homogeneous-like layer, repeated 10 times.

Three 10 nm films ([2Hf + 1Ta] × 54, {5Hf + [1Hf + 1Ta] × 5} × 10, and {10Hf + [1Hf + 1Ta] × 10} × 5) with identical overall Ta atomic concentration of 28% were grown; The overall HfO_2:Ta_2O_3 ALD cycle ratio is 2:1, but the distribution of Ta atoms differs in the three samples. In the [2Hf + 1Ta] × 54 film, Ta can be regarded as homogeneously distributed because the Hf coverage rate is about 30% monolayer coverage/cycle.[26] In {5Hf + [1Hf + 1Ta] × 5} × 10 and {10Hf + [1Hf + 1Ta] × 10} × 5 nanolaminate films, Ta is confined in $HfTa_xO_y$ layers grown using the [1Hf + 1Ta] sequence, which are periodically separated by HfO_2 layers, as shown in the illustrations in Figure 6.9. Not all 5 Hf ALD layers lead to HfO_2 because there is likely a transition from $HfTa_xO_y$ in the [1Hf + 1Ta] × 5 layer to the HfO_2-only layer as illustrated in the qualitative presentation in the inset of Figure 6.9. Considering the relative thickness of the [1Hf + 1Ta] layers in nanolaminate films (in comparison with the $HfTa_xO_y$ layers in [xHf + 1Ta] periodic films), we ignore the finite Hf layers needed to realize HfO_2-only layers. The two nanolaminate films have the same local Ta concentration in the [1Hf + 1Ta] × 5 or 10 layers and the same HfO_2-to-$HfTa_xO_y$ thickness ratio, but the {5Hf + [1Hf + 1Ta] × 5} × 10 film has a thinner thickness of the repeated layers, or higher periodicity.

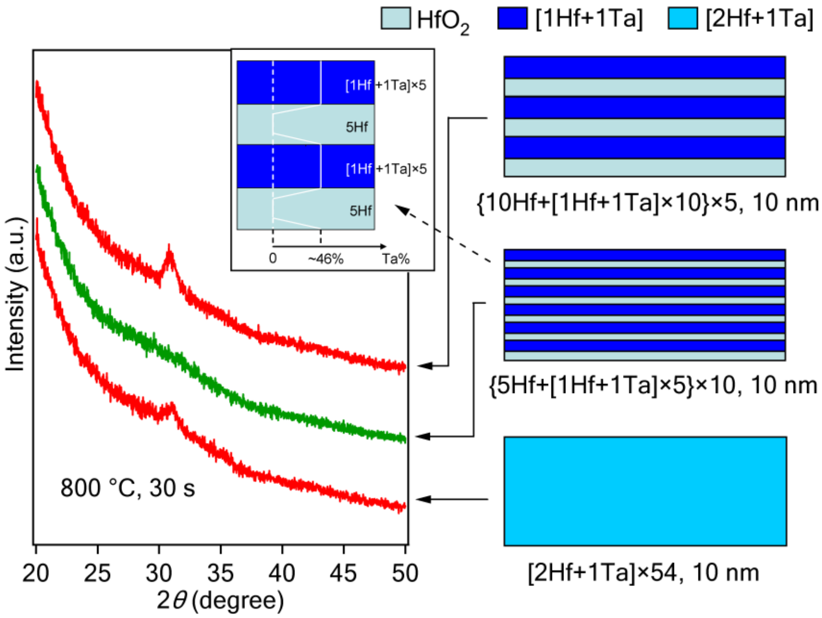

Figure 6.9. XRD spectra of 10 nm [2Hf + 1Ta] × 54, {5Hf + [1Hf + 1Ta] × 5} × 10, and {10Hf + [1Hf + 1Ta] × 10} × 5 after 800 °C annealing, and their corresponding illustrations. Ta can be regarded as homogeneously distributed in [2Hf + 1Ta] and [1Hf + 1Ta]. Inset: qualitative presentation of La% distribution in different layers, highlighting the transition from $HfTa_xO_y$ in the [1Hf + 1Ta] × 5 layer to the HfO_2-only layer.

After the same 800 °C 30 s annealing, the 10 nm [2Hf + 1Ta] × 54, which is more like a homogenous film, has started crystallizing as shown in Figure 6.9, whereas the {5Hf + [1Hf + 1Ta] × 5} × 10 nanolaminate film is still amorphous. With the same overall Ta concentration, the nanolaminate with 10 repeated HfO_2–$HfTa_xO_y$ structures and importantly thinner nanolaminate repeat sections has a higher thermal stability. Doubling thickness for both HfO_2 and $HfTa_xO_y$, and halving the periodicity to remain the same overall film thickness, the {10Hf + [1Hf + 1Ta] × 10} × 5 nanolaminate is crystallized after the 800 °C 30 s annealing.

There are ten ultrathin HfO_2 layers in the {5Hf + [1Hf + 1Ta] × 5} × 10 nanolaminate. The crystallization temperature for 10 nm HfO_2 is between 450 and 500 °C, as shown in Figure 6.3a. Thinner HfO_2 films have higher thermal stability,[2,54] because monoclinic HfO_2 was found to have the largest surface enthalpy and amorphous HfO_2 the smallest surface enthalpy.[55] As film thickness decreases, the surface energy of the amorphous phase makes a greater contribution to the total energy, which enables the film to remain amorphous. The ultrathin HfO_2 layers in {5Hf + [1Hf + 1Ta] × 5} × 10 will remain amorphous above the crystallization temperature for a 10 nm HfO_2 film.

Moreover, ten HfO_2–$HfTa_xO_y$ interfaces are introduced into {5Hf + [1Hf + 1Ta] × 5} × 10 compared with [2Hf + 1Ta] × 54. Crystallization is more likely to initiate from the HfO_2 layers, rather than the $HfTa_xO_y$ layers. When crystallization tends to occur, ten crystalline-amorphous interfaces tend to form, which are thermodynamically unfavorable. Thus the film would remain amorphous to prevent the formation of crystalline-amorphous interfaces, until the temperature is high enough for the crystalline phase to grow through the more stable $HfTa_xO_y$ layers. Both ultrathin HfO_2 layers and the existence of HfO_2–$HfTa_xO_y$ interfaces likely increase the thermal stability of the {5Hf + [1Hf + 1Ta] × 5} × 10 nanolaminate.

Upon comparing the {5Hf + [1Hf + 1Ta] × 5} × 10 and {10Hf + [1Hf + 1Ta] × 10} × 5 results in Figure 6.9, there are likely two inversely related factors determining the film thermal stability: (1) thicker HfO_2 and [2Hf + 1Ta] ultrathin layers are both easier to crystallize by themselves and (2) thicker [2Hf + 1Ta] can block the growth of crystalline phase more effectively given our hypothesis that crystallization starts from the ultrathin HfO_2 layers. To better understand the crystallization mechanism of nanolaminate as well as [xHf + 1Ta] periodic films, it is necessary to test whether crystallization starts from HfO_2 ultrathin layers or $HfTa_xO_y$ layers.

For HfO_2–$HfTa_xO_y$ nanolaminate films with the same overall thickness, there are three factors determining the crystallization temperature (T_c): (1) local Ta concentration, (2) thickness of the HfO_2 ultrathin layers, and (3) thickness of the $HfTa_xO_y$ ultrathin layers. We choose [1Hf + 1Ta] as the $HfTa_xO_y$ layer composition, and grew {10Hf + [1Hf + 1Ta] × 10} × 5 as the standard (Figure 6.10a). Two comparisons are performed to identify which layer starts the crystallization process. One comparison is decreasing factor (2), while holding factor (1) and (3) constant, shown as (b)→(a)→(c) in Figure 6.10. The other comparison is decreasing factor (3), while holding (1) and (2) constant, shown as (d)→(a)→(e) in Figure 6.10. The local Ta concentration in all $HfTa_xO_y$ layers should be around 46%, which is close to the 10 nm [1Hf + 1Ta] × 86 film. The growth rate of HfO_2 and [1Hf + 1Ta] is 0.78 Å/cycle and 1.16 Å/sequence. In the standard film (a), 10 ALD layers of HfO_2 give 0.78 nm, and [1Hf + 1Ta] × 10 gives 1.16 nm. Theoretically the {10Hf + [1Hf + 1Ta] × 10} × 5 is 9.7 nm. The measured as-deposited film thickness is 9.5 nm by ellipsometry. The as-deposited overall film thickness for all the five samples are 10.1 ± 0.6 nm (1 nm interfacial SiO_2 excluded). In sample (d), {11Hf + [1Hf + 1Ta] × 22} is used instead of {10Hf + [1Hf + 1Ta] × 20}, because the latter deposition sequence can not grow a film close to 10 nm.

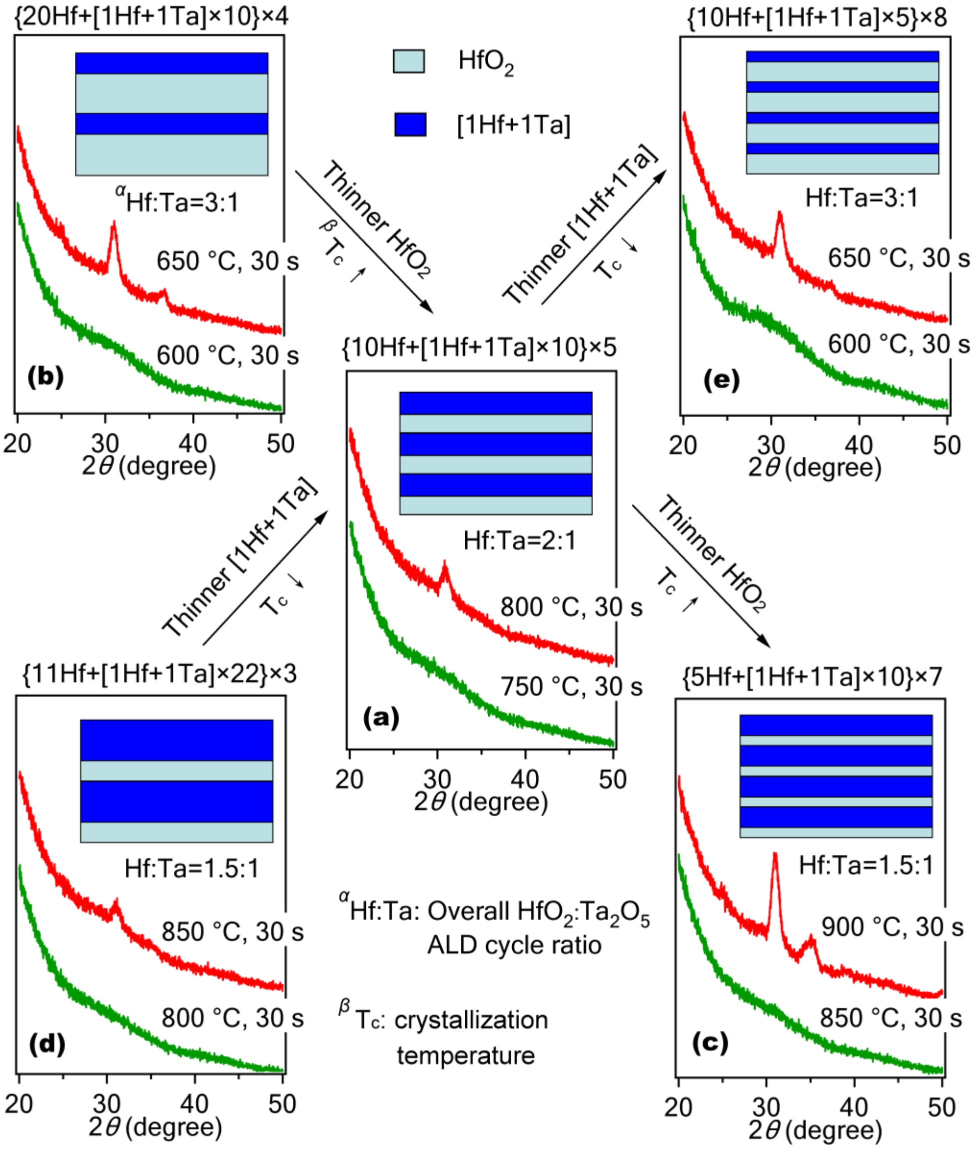

Figure 6.10. Crystallization temperatures and structure illustrations of 10 nm HfO$_2$-HfTa$_x$O$_y$ nanolaminate films for two comparisons. First comparison: fixed HfTa$_x$O$_y$ layer thickness with thinner HfO$_2$, (b)→(a)→(c); second comparison: fixed HfO$_2$ layer thickness with thinner HfTa$_x$O$_y$, (d)→(a)→(e). Sample (a) is the standard and HfTa$_x$O$_y$ layers are grown as [1Hf + 1Ta].

Recall that T_c should increase with decreasing film thickness. In the first comparison, all [1Hf + 1Ta] layers are fixed at 1.16 nm. Assuming the 20Hf, 10Hf, and 5Hf ALD cycles result in HfO_2, i.e., ignoring the finite Hf layers needed to realized Hf depositing only on HfO_2, the HfO_2 decreases from 1.56→0.78→0.39 nm, for (b)→(a)→(c). T_c of these three sample increases from (600 ~ 650)→(750 ~ 800)→(850 ~ 900) °C, supporting the hypothesis that crystallization is initiated from within the HfO_2 layers. In the second comparison, all HfO_2 layers are fixed at 0.78 nm. With [1Hf + 1Ta] decreasing from 2.55→1.16→0.58 nm, for (d)→(a)→(e), T_c of these three sample decreases from (800 ~ 850)→(750 ~ 800)→(600 ~ 650) °C, which should not happen if crystallization starts from within the [1Hf + 1Ta] layers. Moreover, if crystallization starts from within the [1Hf + 1Ta] layers, T_c of sample (d), (a), and (e) should be higher than 900 °C, because T_c of a 10 nm [1Hf + 1Ta] × 86 is (900 ~ 950) °C, as shown in Figure 6.4a. The 10 ALD layers of HfO_2 (0.78 nm) in (d), (a), and (e) is thick enough that [1Hf + 1Ta] × 22, [1Hf + 1Ta] × 10, and [1Hf + 1Ta] × 5 can be regarded as separated ultrathin [1Hf + 1Ta] layers, with even higher T_c compared with [1Hf + 1Ta] × 86.

In the second comparison [(d)→(a)→(e)], the HfO_2 layers in all the three nanolaminates have the same ability to induce crystallization and the nanolaminate crystallization temperature decreases as the $HfTa_xO_y$ layer thins. Although crystallization tends to start from within the HfO_2 layers, if a nanolaminate film crystallizes, the entire film stack crystallized. A repeated crystalline-amorphous multilayer structure is thermodynamically unstable, and such a film should be composed of monoclinic HfO_2 and amorphous $HfTa_xO_y$. But we never observe an XRD pattern that only shows the monoclinic peaks without the tetragonal peaks with 10 °C annealing increments. For the crystallization process to proceed, the temperature has to be high enough to allow the HfO_2-induced crystallization to penetrate across the entire film. Thus the role of $HfTa_xO_y$

layers in the nanolaminate crystallization process is to block the growth of the crystalline phase, which explains why sample (d) has the highest T_c in the second comparison.

Sample (c) and (d) have the same overall HfO_2:Ta_2O_5 ALD cycle ratio, 1.5:1; sample (b) and (e) have the same overall HfO_2:Ta_2O_5 ALD cycle ratio 3:1. Notice that samples with a higher overall La concentration (smaller overall HfO_2:Ta_2O_5 ALD cycle ratio) always have a higher T_c. One possibility is that HfO_2 and $HfTa_xO_y$ layers are intermixed prior to the start of the crystallization process, so T_c is only determined by the overall Ta concentration in the intermixed homogeneous film. However, if intermixing occurs before crystallization, sample (c) and (d), which have the same overall Ta concentration, should have the same T_c. In fact, sample (c) with 7 repeated HfO_2–$HfTa_xO_y$ structures has a higher T_c than sample (d) with only 3 repeated HfO_2–$HfTa_xO_y$ structures, the same relationship as the two nanolanimates in Figure 6.9. Increased thermal stability for the film with more repeated HfO_2–$HfTa_xO_y$ structures implies periodicity still exists at the onset of crystallization. If the film is still a nanolaminate at the beginning of the crystallization process, crystallization has to have a preference for either the HfO_2 or the [1Hf + 1Ta] layers. From the discussion in the previous paragraph, we conclude that crystallization starts from within the HfO_2 layers and the role of the [1Hf + 1Ta] layers is to block the penetration of the crystalline phase over the entire film.

The results (Figure 6.10) and general observations are not limited to the Ta–HfO_2 system. Similar comparisons were conducted for Al-HfO_2 nanolaminate films, which are composed of repeated HfO_2–$HfAl_xO_y$ structures, as shown in Figure 6.11. The $HfAl_xO_y$ layers are grown as [2Hf + 1Al]. The overall film thickness for the five samples is 10.1 nm ± 0.4 nm (1 nm interfacial SiO_2 excluded). [2Hf + 1Al] has been found to be more like a homogeneous film by angle-resolved XPS analysis,[29] and the local Al

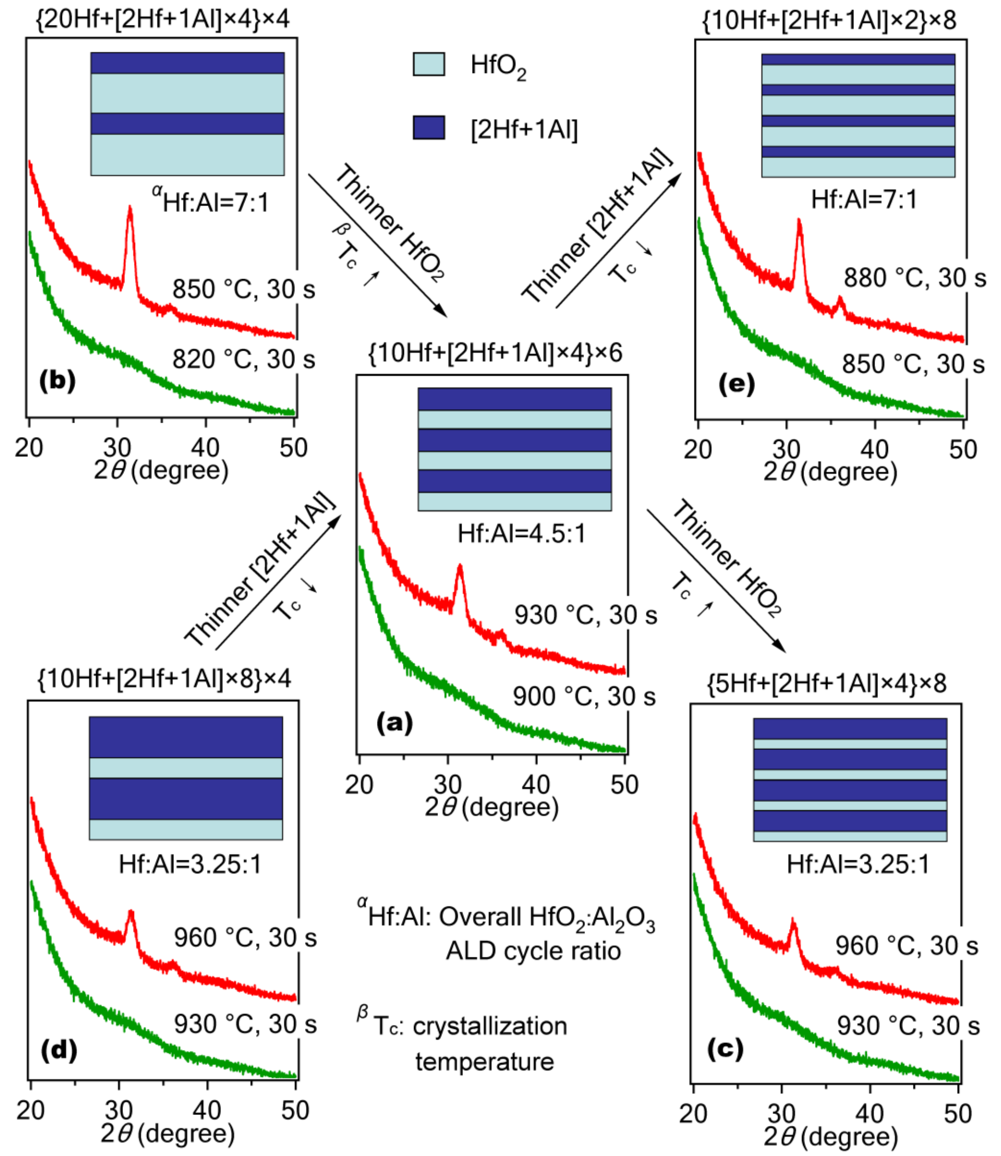

Figure 6.11. Crystallization temperatures and structure illustrations of 10 nm HfO$_2$-HfAl$_x$O$_y$ nanolaminate films for two comparisons. First comparison: fixed HfAl$_x$O$_y$ layer thickness with thinner HfO$_2$, (b)→(a)→(c); second comparison: fixed HfO$_2$ layer thickness with thinner HfAl$_x$O$_y$, (d)→(a)→(e). Sample (a) is the standard and HfAl$_x$O$_y$ layers are grown as [2Hf + 1Al].

concentration in [2Hf + 1Al] is 42%. {10Hf + [2Hf + 1Al] × 4} × 6 is used as the standard, shown as (a) in figure 6.11. The growth rate of HfO$_2$ and [2Hf + 1Al] is 0.78

Å/cycle and 2.26 Å/sequence, respectively. In the standard film (a), 10 ALD layers of HfO_2 give 0.78 nm, and [2Hf + 1Ta] × 4 gives 0.90 nm. The thickness of HfO_2 and [2Hf + 1Al] layers in the four other films can be calculated similarly.

In the first comparison [(b)→(a)→(c)], all [2Hf + 1Al] layers are fixed at 0.90 nm. With HfO_2 decreasing from 1.56→0.78→0.39 nm, T_c increases from (850 ~ 820)→(900 ~ 930)→(930 ~ 960) °C, confirming that crystallization starts from within HfO_2 layers. In the second comparison [(d)→(a)→(e)], all HfO_2 layers are fixed at 0.78 nm. With [2Hf + 1Al] decreasing from 1.81→0.90→0.45 nm, T_c decreases from (930 ~ 960)→(900 ~ 930)→(850 ~ 880) °C, confirming that [2Hf + 1Al] layers block the growth of the crystalline phase in the crystallization process. Again, sample (b) and (e) have the same overall HfO_2:Al_2O_3 ALD cycle ratio (the same overall Al concentration), but the film with more repeated HfO_2–$HfAl_xO_y$ structures has a higher thermal stability. The degree of periodicity still affects T_c for sample (b) and (e) around 820 ~ 880 °C, indicating at the beginning of the crystallization process they are still nanolaminates, rather than homogeneous mixtures.

Comparing the two standard samples in Figure 6.10 and 6.11, the overall film thickness is 9.5 and 10.1 nm, respectively. One {10Hf + [1Hf + 1Ta] × 10} and {10Hf + [2Hf + 1Al] × 4} sequence is 1.90 and 1.68 nm, respectively. [1Hf + 1Ta] × 10 and [2Hf + 1Al] × 4 is 1.16 and 0.90 nm, respectively. The local Ta and Al concentrations are 46 and 42%, respectively. Thus these two nanolaminate films have very similar film structures, except that the incorporated elements are different. Both amorphous Ta_2O_5 and Al_2O_3 form MCRN networks, but the electronegativity difference between Al and O in Al_2O_3 is smaller than that between Ta and O in Ta_2O_5, and the average bond ionicity of Al–O is smaller than that of Ta–O,[44] indicating amorphous Al_2O_3 is more like the CRN structure of SiO_2, so Al_2O_3 is a stronger amorphizer than Ta_2O_5. With the similar film structure, a nanolaminte film incorporated with a stronger amorphizer has a higher thermal stability. Thus, the factors determining the thermal stability of a HfO_2–HfM_xO_y nanolaminate can be concluded as: the species M, local M concentration, thickness of the HfO_2 layer, and thickness of the HfM_xO_y layer.

Knowing the factors determining the thermal stability of HfO_2–HfM_xO_y nanolaminates, the crystallization mechanism of $[x\text{Hf} + 1\text{M}] \times n$ periodic films can be understood. We have shown that HfO_2–HfM_xO_y periodic structure exists in $[x\text{Hf} + 1\text{M}] \times n$ films when x is greater than a certain number. For example, when $x \geq 3$,[28] and 5,[29] periodic structure exists in $[x\text{Hf} + 1\text{La}] \times n$ and $[x\text{Hf} + 1\text{Al}] \times n$ films, respectively. If x is too small and the film is more like a homogeneous mixture, the ALD-grown $[x\text{Hf} + 1\text{M}] \times n$ film should have the same crystallization mechanism as homogeneous films, where the thermal stability is determined by the species M, the M concentration, and the overall film thickness. On the other hand, if x is big enough to ensure the existence of periodic structures, HfO_2 ultrathin layers would exist and affect the crystallization onset temperature. So the thickness of HfO_2 ultrathin layers can be used as an extra factor to control the film thermal stability. When $[x\text{Hf} + 1\text{M}] \times n$ forms a HfO_2–HfM_xO_y periodic structure, the incorporated M atoms only interacts with a limited ALD layers of the host HfO_2 in the as-deposited film. Although it is difficult to calculate the precise local M concentration and the thickness of HfM_xO_y, these two factors should remain constant with different x values, i.e., the x here refers to $[x\text{Hf} + 1\text{M}]$, as long as x is large enough to ensure the existence of the HfO_2–HfM_xO_y periodic structure. Thus $[x\text{Hf} + 1\text{M}] \times n$ with periodic structure can be considered analogous to HfO_2–HfM_xO_y nanolaminate with fixed local M concentration and HfM_xO_y layer thickness. The thickness of HfO_2 ultrathin layers would affect the film thermal stability in the same way as (b)→(a)→(c) nanolaminates in Figure 6.10 and 6.11.

Therefore, the factors determining the thermal stability of a [xHf + 1M] × n film with periodic structure is only the species of M and thickness of the HfO_2 ultrathin layer. The overall film thickness is less important because it is found that the thermal stability of [8Hf + 1Al] and [6Hf + 1La] films are independent of film thickness up to 40 nm.[29] With an appropriately designed periodic structure, ALD-grown films may have a stronger thermal stability compared with the homogeneous film with the same incorporated element concentration. This extra thermal stability may disappear when the repeated HfO_2 ultrathin layers are too thick, because thicker HfO_2 ultrathin layer may initiate the crystallization process more easily.

To sum up, in HfO_2–HfM_xO_y nanolaminates and [xHf + 1M] × n films with HfO_2–HfM_xO_y periodic structures, crystallization starts from the HfO_2 ultrathin layers, and the HfM_xO_y layers block the growth of the crystalline phase. T_c of HfO_2–HfM_xO_y nanolaminates is determined by the species M, local concentration of M, thickness of HfO_2, and thickness of HfM_xO_y. T_c of [xHf + 1M] × n films with HfO_2–HfM_xO_y periodic structures is only determined by the species M and thickness of the HfO_2 ultrathin layer, because the local M concentration and HfM_xO_y thickness is defined by the degree of intermixing between HfO_2 and M oxide in the as-deposited film, which is not a controllable factor. For a fixed M species and overall M concentration, films with an appropriately high periodicity would have an extra thermal stability. For a fixed total thickness, when the periodicity is too high (too small x and too large n in [xHf + 1M] × n), the film becomes a homogeneous mixture, and when the periodicity is to low (too large x and too small n), the film thermal stability decreases because thicker HfO_2 ultrathin layers tend to crystallize at a lower temperature.

6.4. SUMMARY

Ta_2O_5 is incorporated into HfO_2 as [*x*Hf + 1Ta] × *n* periodic films using ALD to study the thermal stability enhancement of Ta-incorporation. HfO_2–$HfTa_xO_y$ nanolaminates are compared with periodically-structured [*x*Hf + 1Ta] × *n* films to explore the relationship between film structure and thermal stability. A 10 nm [1Hf + 1Ta] × 86 film can remain amorphous up to 900 °C, which is higher than both 10 nm HfO_2 and Ta_2O_5. A 10 nm [2Hf + 1Ta] × 54 film can remain amorphous up to 750 °C, with a dielectric constant of 21.5. Both the dielectric constant and leakage current density of the [2Hf + 1Ta] film are intermediate between HfO_2 and Ta_2O_5. For HfO_2–$HfTa_xO_y$ nanolaminates and periodically-structured [*x*Hf + 1Ta] × *n* films, crystallization starts from the HfO_2 ultrathin layers, and the $HfTa_xO_y$ layers block the growth of the crystalline phase. T_c of HfO_2–$HfTa_xO_y$ nanolaminate increases with higher local Ta concentration, thinner HfO_2 layers, and thicker of $HfTa_xO_y$ layers, whereas T_c of [*x*Hf + 1Ta] × *n* periodic films increases only with thinner HfO_2 ultrathin layers. For a fixed overall amorphizer concentration, a higher thermal stability can be achieved by tuning the periodic structure in a film.

6.5. REFERENCES

(1) Wilk, G. D.; Wallace, R. M.; Anthony, J. M. *J. Appl. Phys.* **2001**, *89*, 5243–5275.

(2) Gusev, E. P.; Cabral, C.; Copel, M.; D'Emic, C.; Gribelyuk, M. *Microelectron. Eng.* **2003**, *69*, 145–151.

(3) Kukli, K.; Aarik, J.; Uustare, T.; Lu, J.; Ritala, M.; Aidla, A.; Pung, L.; Harsta, A.; Leskela, M.; Kikas, A.; Sammelselg, V. *Thin Solid Films* **2005**, *479*, 1–11.

(4) Kukli, K.; Pilvi, T.; Ritala, M.; Sajavaara, T.; Lu, J.; Leskela, M. *Thin Solid Films* **2005**, *491*, 328–338.

(5) Hausmann, D. M.; Kim, E.; Becker, J.; Gordon, R. G. *Chem. Mater.* **2002**, *14*, 4350–4358.

(6) Mommer, N.; Lee, T.; Gardner, J. A. *J. Mater. Res.* **2000**, *15*, 377–381.

(7) Wilk, G. D.; Wallace, R. M.; Anthony, J. M. *J. Appl. Phys.* **2000**, *87*, 484–492.

(8) Tomida, K.; Kita, K.; Toriumi, A. *Appl. Phys. Lett.* **2006**, *89*, 142902/1–142902/3.

(9) Ohshita, Y.; Ogura, A.; Ishikawa, M.; Kada, T.; Hoshino, A.; Suzuki, T.; Machida, H.; Soai, K. *Chem. Vap. Deposition* **2006**, *12*, 130–135.

(10) Lee, D.; Suh, D.; Pae, Y.; Kim, H.; Cho, M.; Ko, D. *J. Electrochem. Soc.* **2007**, *154*, H708–H712.

(11) Sivasubramani, P.; Kim, J.; Kim, M. J.; Gnade, B. E.; Wallace, R. M. *J. Appl. Phys.* **2007**, *101*, 114108/1–114108/4.

(12) Hoppe, E. E.; Aita, C. R. *Appl. Phys. Lett.* **2008**, *92*, 141912/1–141912/3.

(13) Marshall, P. A.; Potter, R.; Jones, A. C.; Chalker, P. R.; Taylor, S.; Critchlow, G. W.; Rushworth, S. A. *Chem. Vap. Deposition* **2004**, *10*, 275–279.

(14) Song, M.; Kang, S.; Rhee, S. *J. Electrochem. Soc.* **2005**, *152*, C108–C112.

(15) Ho, M.; Gong, H.; Wilk, G. D.; Busch, B. W.; Green, M. L.; Lin, W. H.; See, A.; Lahiri, S. K.; Loomans, M. E.; Raisanen, P. I.; Gustafsson, T. *Appl. Phys. Lett.* **2002**, *81*, 4218–4220.

(16) Cho, M.; Chang, H. S.; Cho, Y. J.; Moon, D. W.; Min, K.; Sinclair, R.; Kang, S. K.; Ko, D.; Lee, J. H.; Gu, J. H.; Lee, N. I. *Appl. Phys. Lett.* **2004**, *84*, 571–573.

(17) Yamamoto, Y.; Kita, K.; Kyuno, K.; Toriumi, A. *Appl. Phys. Lett.* **2006**, *89*, 032903/1–032903/3.

(18) He, W.; Chan, D. S.; Kim, S.; Kim, Y.; Kim, S.; Cho, B. J. *J. Electrochem. Soc.* **2008**, *155*, G189–G193.

(19) Wang, T.; Ekerdt, J. G. *Chem. Mater.* **2009**, *21*, 3096–3101.

(20) Huang, L.; Li, A.; Zhang, W.; Li, H.; Xia, Y.; Wu, D. *Appl. Surf. Sci.* **2010**, *256*, 2496–2499.

(21) Zhang, M. H.; Rhee, S. J.; Kang, C. Y.; Choi, C. H.; Akbar, M. S.; Krishnan, S. A.; Lee, T.; Ok, I. J.; Zhu, F.; Kim, H. S.; Lee, J. C. *Appl. Phys. Lett.* **2005**, *87*, 232901/1–232901/3.

(22) Lu, J.; Kuo, Y.; Tewg, J. *J. Electrochem. Soc.* **2006**, *153*, G410–G416.

(23) Gu, D.; Li, J.; Dey, S. K.; De Waard, H.; Marcus, S. *J. Vac. Sci. Technol., B* **2006**, *24*, 2230–2235.

(24) Zhao, X.; Vanderbilt, D. *Phys. Rev. B*. **2002**, *65*, 233106/1–233106/4.

(25) Puurunen, R. L. *J. Appl. Phys.* **2005**, *97*, 121301/1–121301/52.

(26) Consiglio, S.; Mo, R. T.; Tai, T.; Krishnan, S. A.; O'Meara, D.; Wajda, C.; Chudzik, M. P. *ECS Trans.* **2007**, *6*, 167–177.

(27) Van, T. T.; Bargar, J. R.; Chang, J. P. *J. Appl. Phys.* **2006**, *100*, 023115/1–023115/8.

(28) Wang, T.; Ekerdt, J. G. *Chem. Mater.* **2010**, *22*, 3798–3806.

(29) Wang, T.; Ekerdt, J. G. *Chem. Mater.* **2010**, *submitted.*

(30) Kukli, K.; Ritala, M.; Sajavaara, T.; Keinonen, J.; Leskela, M. *Chem. Vap. Deposition* **2002**, *8*, 199–204.

(31) Hausmann, D. M.; Rouffignac, P. D.; Smith, A.; Gordon, R.; Monsma, D. *Thin Solid Films* **2003**, *443*, 1–4.

(32) Kuo, Y. *J. Electrochem. Soc.* **1992**, *139*, 579–583.

(33) Atanassova, E.; Dimitrova, T.; Koprinarova, J. *Appl. Surf. Sci.* **1995**, *84*, 193–202.

(34) Fu, Z.; Huang, F.; Chu, Y.; Zhang, Y.; Qin, Q. *J. Electrochem. Soc.* **2003**, *150*, A776–A782.

(35) *NIST X-ray Photoelectron Spectroscopy Database*; http://srdata.nist.gov/xps/.

(36) Lao, S. X.; Martin, R. M.; Chang, J. P. *J. Vac. Sci. Technol., A* **2005**, *23*, 488–496.

(37) Deshpande, A.; Inman, R.; Jursich, G.; Takoudis, C. *Microelectron. Eng.* **2006**, *83*, 547–552.

(38) Atanassova, E.; Spassov, D. *Appl. Surf. Sci.* **1998**, *135*, 71–82.

(39) Barr, T. L. *J. Vac. Sci. Technol., A* **1991**, *9*, 1793–1805.

(40) Moulder, J. F.; Stickle, W. F.; Sobol, P. E.; Bomben, K. D. *Handbook of X-ray Photoelectron Spectroscopy*; Physical Electronics, Inc.: Eden Prairie, MN, 1995.

(41) Garvie, R. C. *J. Phys. Chem.* **1978**, *82*, 218–224.

(42) Wang, J.; Li, H. P.; Stevens, R. *J. Mater. Sci.* **1992**, *27*, 5397–5430.

(43) Toriumi, A.; Kita, K. In *Dielectric Films for Advanced Microelectronics*; Baklanov, M.; Green, M.; Maex, K. ; John Wiley & Sons: Hoboken, NJ, 2007; p. 297–336.

(44) Lucovsky, G.; Whitten, J. L. In *High Dielectric Constant Materials: VLSE MOSFET Applications*; Huff, H. R.; Gilmer, D. C. ; Springer: New York, 2005; p. 311–358.

(45) Hudner, J.; Hellberg, P.; Kusche, D.; Ohlsen, H. *Thin Solid Films* **1996**, *281-282*, 415–418.

(46) Chiu, F.; Wang, J.; Lee, J. Y.; Wu, S. C. *J. Appl. Phys.* **1997**, *81*, 6911–6915.

(47) Lee, J. S.; Chang, S. J.; Chen, J. F.; Sun, S. C.; Liu, C. H.; Liaw, U. H. *Mater. Chem. Phys.* **2002**, *77*, 242–247.

(48) Zeng, W.; Eisenbraun, E.; Frisch, H.; Sullivan, J. J.; Kaloyeros, A. E.; Margalit, J.; Beck, K. *J. Electrochem. Soc.* **2004**, *151*, F172–F177.

(49) Majumder, P.; Jursich, G.; Takoudis, C. *J. Appl. Phys.* **2009**, *105*, 104106/15–104106/6.

(50) Lee, C.; Cho, E.; Lee, H.; Hwang, C. S.; Han, S. *Phys. Rev. B*. **2008**, *78*, 012102/1–012102/4.

(51) Govindarajan, S.; Boscke, T. S.; Sivasubramani, P.; Kirsch, P. D.; Lee, B. H.; Tseng, H.; Jammy, R.; Schroder, U.; Ramanathan, S.; Gnade, B. E. *Appl. Phys. Lett.* **2007**, *91*, 062906/1–062906/3.

(52) Lau, W. S.; Khaw, K. K.; Han, T.; Sandler, N. P. *Appl. Phys. Lett.* **2006**, *89*, 262901/1–262901/3.

(53) Kamiyama, S.; Pierre-Yves; Lesaicherre; Suzuki, H.; Sakai, A.; Nishiyama, I.; Ishitani, A. *J. Electrochem. Soc.* **1993**, *140*, 1617–1625.

(54) Cho, M.; Roh, Y. S.; Whang, C. N.; Jeong, K.; Nahm, S. W.; Ko, D.; Lee, J. H.; Lee, N. I.; Fujihara, K. *J. Appl. Phys.* **2002**, *81*, 472–474.

(55) Navrotsky, A. *J. Mater. Chem.* **2005**, *15*, 1883–1890.

Chapter 7: Research Summary

7.1. CONCLUSION

HfO_2 films were grown using ALD and incorporated with three elements (La, Al, and Ta) to form HfO_2-based ternary oxides with enhanced the thermal stability to stabilize the amorphous phase under high temperature annealing, which show application potentials for the continuous scaling of the CMOS devices. The incorporation can be achieved by growing multiple ALD layers of HfO_2 and one ALD layer of MO_x (M = La, Al, and Ta) alternately (denoted as [xHf + 1M]), and the incorporation concentration can be effectively controlled by varying the HfO_2-to-MO_x ALD cycle ratio (the x value). Besides the [xHf + 1M] films, HfO_2–HfM_xO_y nanolaminate films are also grown to investigate the relationship between film structure and thermal stability.

The 10 nm HfO_2 film crystallizes at 500 °C into the monoclinic phase, whereas the 10 nm La, Al, and Ta-incorporated HfO_2 films can remain amorphous up to 900 °C, with 25, 32, and 46% incorporation concentration (metal basis), respectively. Upon incorporation, a monoclinic-to-tetragonal/cubic phase transformation is observed for the crystallized La, Al, and Ta-incorporated HfO_2 films.

Using high-k material as the amorphizer, the thermal stability of HfO_2 can be enhanced without compromising its high-k property. A 10 nm La-incorporated HfO_2 film with 13% La (metal basis) remains amorphous up to 800 °C, and has a dielectric constant of 16.6, which is about the same value as pure HfO_2 in this study. A 10 nm Ta-incorporated HfO_2 film with 28% Ta (metal basis) remains amorphous up to 750 °C, and has an increased dielectric constant of 21.5.

Ternary oxide films grown by ALD may have a periodic structure (in the growth direction) because of the layer-by-layer growth mechanism of ALD. When the HfO_2-to-MO_x ALD cycle ratio is high enough in [xHf + 1M] flims, HfO_2–HfM_xO_y periodic structure composed of HfO_2-only layers separated by HfM_xO_y layers exits in the as-deposited films. For example, AR-XPS reveals that when $x > 3$ and 4 for [xHf + 1La] and [xHf + 1Al] films, respectively, these two systems are composed of repeated HfO_2-$HfLa_xO_y$ and HfO_2-$HfAl_xO_y$ structures. When $x < 3$ and 4 for [xHf + 1La] and [xHf + 1Al] films, respectively, these two systems are more like homogeneous mixtures.

The periodic structure of the ALD-grown film can effectively affect the film thermal stability. For films without periodic structures (such as HfO_2, [3Hf + 1Al], and [3Hf + 1La]), their thermal stability decreases upon increasing the film thickness, because the surface energy, which favors the amorphous phase, contributes to a smaller portion of the total energy in thicker films. On the contrary, the thermal stability of 10 nm [8Hf + 1Al] and [6Hf + 1La] films are independent of film thickness up to 40 nm. A detailed analysis in Chapter 6 shows that crystallization tend to start from the HfO_2 layers and the role of HfM_xO_y layer is to block the growth of the crystalline phase for films composed of HfO_2-HfM_xO_y periodic structures. The HfO_2-only ultrathin layers have a relatively high crystallization temperature by themselves. Moreover, the existence of extra HfO_2-HfM_xO_y interfaces is also a positive factor for the film to remain amorphous. Thus changing the periodic structure of a film, i.e., changing the thickness of the HfO_2 ultrathin layers or the distribution (in the growth direction) of the incorporated elements, is a potential method to tune the film thermal stability.

The factors determining the film stability for homogeneous/homogeneous-like HfM_xO_y films, HfO_2–HfM_xO_y nanolaminate films, and [xHf + 1M] films with HfO_2–HfM_xO_y periodic structures can be generalized as:

- Homogeneous/homogeneous-like HfM_xO_y films: Species M, concentration of M, and overall film thickness.
- HfO_2–HfM_xO_y nanolaminate films: species M, local concentration of M, thickness of HfO_2, and thickness of HfM_xO_y.
- [xHf + 1M] films with HfO_2–HfM_xO_y periodic structures: species M and thickness of the HfO_2 ultrathin layer.

7.2. RECOMMENDATIONS FOR FUTURE WORK

The ultimate purpose of retaining the amorphous phase of HfO_2 is to reduce the leakage current when use it as the gate dielectric material in CMOS devices. This dissertation is mainly focused the physical and chemical properties of HfO_2-based films with enhanced crystallization temperatures. More detailed studies on the electrical properties of these films would give us better insights in choosing the best high-*k* materials as the gate dielectrics.

La, Al, and Ta-incorporated HfO_2 films are found to crystallize into tetragonal/cubic phase. But definite phase identification between tetragonal and cubic phases are difficult because only two peaks are clearly visible at the $2\theta = 20$–$50°$ range. The crystallized La-incorporated HfO_2 films with tetragonal/cubic phase show distinct optical properties to crystallized HfO_2 films the monoclinic phase, suggesting the disorder in crystallized HfO_2 is largely reduced upon the incorporation of La_2O_3, which is very likely related to the crystalline structure of La-incorporated HfO_2. More characterizations such as high-resolution in-plane XRD or high-resolution transmission electron microscopy (HRTEM) accompanied with selective area electron diffraction (SAD) would give more information to differentiate the two phases, and hence, understand the film structure. First principle calculations may also give more insights in understanding the crystalline structure of crystallized La-incorporated HfO_2, as well as other HfO_2-based ternary oxides.

When studying the distribution of M in [xHf + 1M] films with HfO_2–HfM_xO_y periodic structures, AR-XPS was only conducted in situ for as-deposited amorphous films. AR-XPS for crystallized samples is expected to give more supplementary information about the interaction between the host HfO_2 and the incorporated elements, although this measurement may introduce contamination to the sample surface because our RTA process has to be conducted ex situ. An ALD-XPS system with an additional annealing chamber might be a better solution.

Films with an appropriately high periodicity (appropriately small x and large n in [xHf + 1M] × n) would have an extra thermal stability because of is periodic structure. But the extent of this extra thermal stability enhancement gain by tuning the film structure has not been systematically studied. Theoretically, a HfO_2 film incorporated with a weaker amorphizer with carefully designed periodic structure may turn out to have a higher crystallization temperature than another HfO_2 film homogeneously incorporated with a stronger amorphizer with the same overall incorporation concentration. If one could find two elements satisfying this criterion, their relative amorphizing capability difference may give a hint on estimating the effectiveness of engineering the periodic structure for the purpose of amorphous stabilization.

Appendix

Publications and Presentations:

Wang, T.; Ekerdt, J. G. Atomic Layer Deposition of Lanthanum Stabilized Amorphous Hafnium Oxide Thin Films. *Chem. Mater.* **2009**, *21*, 3096–3101.

Wang, T.; Ekerdt, J. G. Subnanoscale Lanthanum Distribution in Lanthanum-Incorporated Hafnium Oxide Thin Films Grown Using Atomic Layers Deposition. *Chem. Mater.* **2010**, *22*, 3798–3806.

Wang, T.; Ekerdt, J. G. Structure Versus Thermal Stability: the Periodic Structure of ALD-Grown Al-Incorporated HfO_2 and Its Effect on Amorphous Stabilization. *Chem. Mater.* **submitted.**

Wang, T.; Ekerdt, J. G. The Relationship between Film Structure and Enhanced Thermal Stability of Ta_2O_3-Incorporated HfO_2 Grown by Atomic Layer Deposition. **in preparation**.

Wang, T.; Wei, J.-W.; Downer, M. C.; Ekerdt, J. G. Optical Properties of La-Incorporated HfO_2 upon Crystallization. **in preparation.**

Fitzpatrick, P. R.; Wang, T.; Heitsch, A. T.; Korgel, B. A.; Ekerdt, J. G. Oxidation Resistance of Thin Boron Carbo-nitride Films on Ge(100) and Ge Nanowires. *Thin Solid Films* **2009**, *517*, 3686–3694.

Zhou, W.; Ushakov, S. V.; Wang, T.; Ekerdt, J. G.; Demkov, A. A.; Navrotsky, A. Hafnia: Energetics of Thin Films and Nanoparticles. *J. Appl. Phys.* **2010**, *107*, 123514/1–123514/7.

Wang, T.; Ekerdt, J. G. ALD of La Stabilized Amorphous HfO_2 High-*k* Dielectric Thin Films. *AVS 56th International Symposium and Exhibition*, San Jose, CA, November 2009.

Ekerdt, J. G.; Wang, T. Lanthanum Stabilization of ALD-Grown Hafnia. *2008 AIChE Annual Meeting*, Philadelphia, PA, November 2008.

Bibliography

Adelmann, C.; Kesters, J.; Opsomer, K.; Detavernier, C.; Kittl, J. A.; Van Elshocht, S. *Appl. Phys. Lett.* **2009**, *95*, 091911/1–091911/3.

Afanas'ev, V. V.; Stesmans, A.; Chen, F.; Shi, X.; Campbell, S. A. *Appl. Phys. Lett.* **2002**, *81*, 1053–1055.

Aspnes, D. E.; Theeten, J. B.; Hottier, F. *Phys. Rev. B* **1979**, *20*, 3292–3302.

Atanassova, E.; Dimitrova, T.; Koprinarova, J. *Appl. Surf. Sci.* **1995**, *84*, 193–202.

Atanassova, E.; Spassov, D. *Appl. Surf. Sci.* **1998**, *135*, 71–82.

Barr, T. L. *J. Vac. Sci. Technol., A* **1991**, *9*, 1793–1805.

Buiu, O.; Lu, Y.; Mitrovic, I. Z.; Hall, S.; Chalker, P.; Potter, R. J. *Thin Solid Films* **2006**, *515*, 623–626.

Champaneria, R.; Mack, P.; White, R.; Wolstenholme, J. *Surf. Interface Anal.* **2003**, *35*, 1028–1033.

Chang, J. P.; Green, M. L.; Donnelly, V. M.; Opila, R. L.; Eng, J.; Sapjeta, J.; Silverman, P. J.; Weir, B.; Lu, H. C.; Gustafsson, T.; Garfunkel, E. *J. Appl. Phys.* **2000**, *87*, 4449–4455.

Cheng, J.; Li, A.; Shao, Q.; Ling, H.; Wu, D.; Wang, Y.; Bao, Y.; Wang, M.; Liu, Z.; Ming, N. *Appl. Surf. Sci.* **2004**, *233*, 91–98.

Chiou, Y.; Chang, C.; Wu, T. *J. Mater. Res.* **2007**, *22*, 1899–1906.

Chiu, F.; Wang, J.; Lee, J. Y.; Wu, S. C. *J. Appl. Phys.* **1997**, *81*, 6911–6915.

Cho, M.; Chang, H. S.; Cho, Y. J.; Moon, D. W.; Min, K.; Sinclair, R.; Kang, S. K.; Ko, D.; Lee, J. H.; Gu, J. H.; Lee, N. I. *Appl. Phys. Lett.* **2004**, *84*, 571–573.

Cho, M.; Roh, Y. S.; Whang, C. N.; Jeong, K.; Choi, H. J.; Nam, S. W.; Ko, D.; Lee, J. H.; Lee, N. I.; Fujihara, K. *Appl. Phys. Lett.* **2002**, *81*, 1071–1073.

Cho, M.; Roh, Y. S.; Whang, C. N.; Jeong, K.; Nahm, S. W.; Ko, D.; Lee, J. H.; Lee, N. I.; Fujihara, K. *J. Appl. Phys.* **2002**, *81*, 472–474.

Cho, Y. J.; Nguyen, N. V.; Richter, C. A.; Ehrstein, J. R.; Lee, B. H.; Lee, J. C. *Appl. Phys. Lett.* **2002**, *80*, 1249–1251.

Choi, J.; Puthenkovilakam, R.; Chang, J. P. *J. Appl. Phys.* **2006**, *99*, 053705/1–053705/3.

Choi, K.; Kim, J.; Yoon, S.; Shin, W. *J. Vac. Sci. Technol., B* **2004**, *22*, 1755–1758.

Cohen, M. H.; Fritzsche, H.; Ovshinsky, S. R. *Phys. Rev. Lett.* **1969**, *22*, 1065–1068.

Conley, J. F., Jr.; Ono, Y.; Tweet, D. J.; Zhuang, W.; Solanki, R. *Mat. Res. Soc. Proc.* **2002**, *716*, 73–78.

Consiglio, S.; Mo, R. T.; Tai, T.; Krishnan, S. A.; O'Meara, D.; Wajda, C.; Chudzik, M. P. *ECS Trans.* **2007**, *6*, 167–177.

Copel, M.; Cartier, E.; Gusev, E. P.; Guha, S.; Bojarczuk, N.; Poppeller, M. *Appl. Phys. Lett.* **2001**, *78*, 2670–2672.

Copel, M.; Cartier, E.; Ross, F. M. *Appl. Phys. Lett.* **2001**, *78*, 1607–1609.

Craciun, D.; Socol, G.; Axente, E.; Calca, A.; Singh, R.; Craciun, V. *Mater. Res. Soc. Symp. Proc.* **2008**, *1074*, 1074–I03–18.

De Asha, A. M.; Critchley, J. T.; Nix, R. M. *Surf. Sci.* **1998**, *405*, 201–214.

Deshpande, A.; Inman, R.; Jursich, G.; Takoudis, C. *Microelectron. Eng.* **2006**, *83*, 547–552.

Desurvire, E. *Erbium-Doped Fiber Amplifiers*; Wiley: New York, 1994.

Dimoulas, A.; Vellianitis, G.; Mavrou, G.; Apostolopoulos, G.; Travlos, A.; Wiemer, C.; Fanciulli, M.; Rittersma, Z. M. *Appl. Phys. Lett.* **2004**, *85*, 3205–3207.

Essary, C. R.; Ramani, K.; Craciun, V.; Singh, R. K. *Appl. Phys. Lett.* **2006**, *88*, 182902/1–182902/3.

Ferlauto, A. S.; Ferreira, G. M.; Pearce, J. M.; Wronski, C. R.; Collins, R. W.; Deng, X.; Ganguly, G. *J. Appl. Phys.* **2002**, *92*, 2424–2436.

Fu, Z.; Huang, F.; Chu, Y.; Zhang, Y.; Qin, Q. *J. Electrochem. Soc.* **2003**, *150*, A776–A782.

Fujiwara, H. *Spectroscopic Ellipsometry: Principles and Applications*; Wiley: West Sussex, U.K., 2007.

Garvie, R. C. *J. Phys. Chem.* **1978**, *82*, 218–224.

Ghiraldelli, E.; Pelosi, C.; Gombia, E.; Chiavarotti, G.; Vanzetti, L. *Thin Solid Films* **2008**, *517*, 434–436.

Govindarajan, S.; Boscke, T. S.; Sivasubramani, P.; Kirsch, P. D.; Lee, B. H.; Tseng, H.; Jammy, R.; Schroder, U.; Ramanathan, S.; Gnade, B. E. *Appl. Phys. Lett.* **2007**, *91*, 062906/1–062906/3.

Gu, D.; Li, J.; Dey, S. K.; De Waard, H.; Marcus, S. *J. Vac. Sci. Technol., B* **2006**, *24*, 2230–2235.

Guha, S.; Cartier, E.; Gribelyuk, M. A.; Bojarczuk, N. A.; Copel, M. C. *Appl. Phys. Lett.* **2000**, *77*, 2710–2712.

Gusev, E. P.; Cabral, C.; Copel, M.; D'Emic, C.; Gribelyuk, M. *Microelectron. Eng.* **2003**, *69*, 145–151.

Gusev, E. P.; Copel, M.; Cartier, E.; Baumvol, I. J.; Krug, C.; Gribelyuk, M. A. *Appl. Phys. Lett.* **2000**, *76*, 176–178.

Hausmann, D. M.; Kim, E.; Becker, J.; Gordon, R. G. *Chem. Mater.* **2002**, *14*, 4350–4358.

Hausmann, D. M.; Rouffignac, P. D.; Smith, A.; Gordon, R.; Monsma, D. *Thin Solid Films* **2003**, *443*, 1–4.

He, W.; Chan, D. S.; Kim, S.; Kim, Y.; Kim, S.; Cho, B. J. *J. Electrochem. Soc.* **2008**, *155*, G189–G193.

He, W.; Schuetz, S.; Solanki, R.; Belot, J.; McAndrew, J. *Electrochem. Solid-State. Lett.* **2004**, *7*, G131-G133.

Ho, M.; Gong, H.; Wilk, G. D.; Busch, B. W.; Green, M. L.; Lin, W. H.; See, A.; Lahiri, S. K.; Loomans, M. E.; Raisanen, P. I.; Gustafsson, T. *Appl. Phys. Lett.* **2002**, *81*, 4218–4220.

Hoppe, E. E.; Aita, C. R. *Appl. Phys. Lett.* **2008**, *92*, 141912/1–141912/3.

Huang, L.; Li, A.; Zhang, W.; Li, H.; Xia, Y.; Wu, D. *Appl. Surf. Sci.* **2010**, *256*, 2496–2499.

Hubbard, K. J.; Schlom, D. G. *J. Mater. Res.* **1996**, *11*, 2757–2776.

Hudner, J.; Hellberg, P.; Kusche, D.; Ohlsen, H. *Thin Solid Films* **1996**, *281-282*, 415–418.

Inoue, H.; Utsuno, F.; Yasui, I. *J. Non-Cryst. Solids.* **2004**, *349*, 16–21.

Jablonski, A.; Powell, C. J. *J. Electron Spectrosc. Relat. Phenom.* **2000**, *100*, 137–160.

Jones, A. C.; Aspinall, H. C.; Chalker, P. R.; Potter, R. J.; Kukli, K.; Rahtu, A.; Ritala, M.; Leskela, M. *Mater. Sci. Eng., B*. **2005**, *118*, 97–104.

Jones, a.; Aspinall, H.; Chalker, P.; Potter, R.; Manning, T.; Loo, Y.; O'Kane, R.; Gaskell, J.; Smith, L. *Chem. Vap. Deposition* **2006**, *12*, 83–98.

Kamiyama, S.; Pierre-Yves; Lesaicherre; Suzuki, H.; Sakai, A.; Nishiyama, I.; Ishitani, A. *J. Electrochem. Soc.* **1993**, *140*, 1617–1625.

Kang, C. S.; Cho, H.; Onishi, K.; Nieh, R.; Choi, R.; Gopalan, S.; Krishnan, S.; Han, J. H.; Lee, J. C. *Appl. Phys. Lett.* **2002**, *81*, 2593–2595.

Katamreddy, R.; Inman, R.; Jursich, G.; Soulet, A.; Takoudis, C. *Acta Materialia*. **2008**, *56*, 710-718.

Kim, H.; Saraswat, K. C.; McIntyre, P. C. *J. Mater. Res.* **2005**, *20*, 3125–3132.

Kim, S. K.; Choi, G. J.; Kim, J. H.; Hwang, C. S. *Chem. Mater.* **2008**, *20*, 3723–3727.

Kimura, H. *Mater. Res. Soc. Symp. Proc.* **2000**, *621*, Q5.7.1–Q.75.7.6.

Kimura, K.; Nakajima, K.; Conard, T.; Vandervorst, W. *Appl. Phys. Lett.* **2007**, *91*, 104106/1–104106/3.

Kukli, K.; Aarik, J.; Uustare, T.; Lu, J.; Ritala, M.; Aidla, A.; Pung, L.; Harsta, A.; Leskela, M.; Kikas, A.; Sammelselg, V. *Thin Solid Films* **2005**, *479*, 1–11.

Kukli, K.; Pilvi, T.; Ritala, M.; Sajavaara, T.; Lu, J.; Leskela, M. *Thin Solid Films* **2005**, *491*, 328–338.

Kukli, K.; Ritala, M.; Pore, V.; Leskelä, M.; Sajavaara, T.; Hegde, R.; Gilmer, D.; Tobin, P.; Jones, A. C.; Aspinall, H. *Chem. Vap. Deposition* **2006**, *12*, 158–164.

Kukli, K.; Ritala, M.; Sajavaara, T.; Keinonen, J.; Leskela, M. *Chem. Vap. Deposition* **2002**, *8*, 199–204.

Kuo, Y. *J. Electrochem. Soc.* **1992**, *139*, 579–583.

Lao, S. X.; Martin, R. M.; Chang, J. P. *J. Vac. Sci. Technol., A* **2005**, *23*, 488–496.

Lau, W. S.; Khaw, K. K.; Han, T.; Sandler, N. P. *Appl. Phys. Lett.* **2006**, *89*, 262901/1–262901/3.

Lay, T. S.; Chang, S. C.; Din, G. J.; Yeh, C. C.; Hung, W. H.; Lee, W. G.; Kwo, J.; Hong, M. *J. Vac. Sci. Technol., B* **2005**, *23*, 1291–1293.

Lee, C.; Cho, E.; Lee, H.; Hwang, C. S.; Han, S. *Phys. Rev. B* **2008**, *78*, 012102/1–012102/4.

Lee, D.; Suh, D.; Pae, Y.; Kim, H.; Cho, M.; Ko, D. *J. Electrochem. Soc.* **2007**, *154*, H708–H712.

Lee, J. S.; Chang, S. J.; Chen, J. F.; Sun, S. C.; Liu, C. H.; Liaw, U. H. *Mater. Chem. Phys.* **2002**, *77*, 242–247.

Lee, P. F.; Dai, J. Y.; Wong, K. H.; Chan, H. L.; Choy, C. L. *Appl. Phys. Lett.* **2003**, *82*, 2419–2421.

Lehn, J.; Javed, S.; Hoffman, D. *Chem. Vap. Deposition* **2006**, *12*, 280–284.

Lu, J.; Kuo, Y.; Tewg, J. *J. Electrochem. Soc.* **2006**, *153*, G410–G416.

Lucovsky, G.; Whitten, J. L. In *High Dielectric Constant Materials: VLSE MOSFET Applications*; Huff, H. R.; Gilmer, D. C. ; Springer: New York, 2005; p. 311–358.

Mack, P.; White, R.; Wolstenholme, J.; Conard, T. *Appl. Surf. Sci.* **2006**, *252*, 8270–8276.

Majumder, P.; Jursich, G.; Takoudis, C. *J. Appl. Phys.* **2009**, *105*, 104106/15–104106/6.

Marshall, P. A.; Potter, R.; Jones, A. C.; Chalker, P. R.; Taylor, S.; Critchlow, G. W.; Rushworth, S. A. *Chem. Vap. Deposition* **2004**, *10*, 275–279.

Mavrou, G.; Galata, S.; Tsipas, P.; Sotiropoulos, A.; Panayiotatos, Y.; Dimoulas, A.; Evangelou, E. K.; Seo, J. W.; Dieker, C. *J. Appl. Phys.* **2008**, *103*, 014506/1–014506/9.

Molodetsky, I. *J. Non-Cryst. Solids*. **2000**, *262*, 106–113.

Mommer, N.; Lee, T.; Gardner, J. A. *J. Mater. Res.* **2000**, *15*, 377–381.

Moulder, J. F.; Stickle, W. F.; Sobol, P. E.; Bomben, K. D. *Handbook of X-ray Photoelectron Spectroscopy*; Physical Electronics, Inc.: Eden Prairie, MN, 1995.

Navrotsky, A. *J. Mater. Chem.* **2005**, *15*, 1883–1890.

Neumayer, D. A.; Cartier, E. *J. Appl. Phys.* **2001**, *90*, 1801–1808.

Nguyen, N. V.; Davydov, A. V.; Chandler-Horowitz, D.; Frank, M. M. *J. Appl. Phys.* **2005**, *87*, 192903/1–192903/3.

Nguyen, N. V.; Sayan, S.; Levin, I.; Ehrstein, J. R.; Baumvol, I. J.; Driemeier, C.; Krug, C.; Wielunski, L.; Hung, P. Y.; Diebold, A. *J. Vac. Sci. Technol., A* **2005**, *23*, 1706–1713.

Nieminen, M.; Putkonen, M.; Ninisto, L. *Appl. Surf. Sci.* **2001**, *174*, 155–166.

Ohshita, Y.; Ogura, A.; Ishikawa, M.; Kada, T.; Hoshino, A.; Suzuki, T.; Machida, H.; Soai, K. *Chem. Vap. Deposition* **2006**, *12*, 130–135.

Park, T. J.; Kim, J. H.; Jang, J. H.; Na, K. D.; Hwang, C. S.; Yoo, J. H. *Electrochem. Solid-State. Lett.* **2008**, *11*, H121–H123.

Pitcher, M. W.; Ushakov, S. V.; Navrotsky, A.; Woodfield, B. F.; Li, G.; Boerio-Goates, J.; Tissue, B. M. *J. Amer. Cer. Soc.* **2004**, *88*, 160–167.

Plummer, J. D.; Deal, M. D.; Griffin, P. B. *Silicon VLSI Technology: Fundamentals Practice and Modeling*; Prentice Hall: Upper Saddle River, NJ, 2000.

Powell, C. J.; Jablonski, A. *NIST Electron Effective-Attenuation-Length Database*; Version 1.; National Institute of Standards and Technology: Gaithersburg, MD, 2001.

Puurunen, R. L. *J. Appl. Phys.* **2005**, *97*, 121301/1–121301/52.

Robertson, J. *Appl. Surf. Sci.* **2002**, *190*, 2–10.

Robertson, J. *J. Vac. Sci. Technol., B* **2000**, *18*, 1785–1791.

Seah, M. P.; Dench, W. A. *Surf. Interface Anal.* **1979**, *1*, 2–11.

Sivasubramani, P.; Kim, J.; Kim, M. J.; Gnade, B. E.; Wallace, R. M. *J. Appl. Phys.* **2007**, *101*, 114108/1–114108/4.

Song, M.; Kang, S.; Rhee, S. *J. Electrochem. Soc.* **2005**, *152*, C108–C112.

Stemmer, S.; Maria, J.; Kingon, A. I. *Appl. Phys. Lett.* **2001**, *79*, 102–104.

Streetman, B. G.; Banerjee, S. K. *Solid State Electronic Devices*; 6th Editio.; Prentice Hall: Upper Saddle River, NJ, 2006; p. 154–168, 269–270.

Suntola, T. *Thin Solid Films* **1992**, *216*, 84–89.

Suntola, T.; Antson, A. US Pat. 4058430 (1977).

Suzuki, M.; Kagawa, M.; Syono, Y.; Hirai, T. *J. Cryst. Growth.* **1991**, *112*, 621–627.

Tauc, J. *Amorphous and Liquid Semiconductors*; Plenum: London, 1974; p. 159.

Tomida, K.; Kita, K.; Toriumi, A. *Appl. Phys. Lett.* **2006**, *89*, 142902/1–142902/3.

Tompkins, H. G.; McGahan, W. A. *Spectroscopic Ellipsometry and Reflectometry: A User's Guide*; John Wiley & Sons: New York, 1999.

Toriumi, A.; Kita, K. In *Dielectric Films for Advanced Microelectronics*; Baklanov, M.; Green, M.; Maex, K. ; John Wiley & Sons: Hoboken, NJ, 2007; p. 297–336.

Toriumi, A.; Iwamoto, K.; Ota, H.; Kadoshima, M.; Mizubayashi, W.; Nabatame, T.; Ogawa, A.; Tominaga, K.; Horikawa, T.; Satake, H. *Microelectron. Eng.* **2005**, *80*, 190-197.

Triyoso, D. H.; Hegde, R. I.; Grant, J. M.; Schaeffer, J. K.; Roan, D.; White, B. E.; Tobin, P. J. *J. Vac. Sci. Technol., B* **2005**, *23*, 288–297.

Triyoso, D. H.; Hegde, R. I.; Grant, J.; Fejes, P.; Liu, R.; Roan, D.; Ramon, M.; Werho, D.; Rai, R.; La, L. B.; Baker, J.; Garza, C.; Guenther, T.; White, B. E.; Tobin, P. J. *J. Vac. Sci. Technol., B* **2004**, *22*, 2121–2127.

Triyoso, D.; Liu, R.; Roan, D.; Ramon, M.; Edwards, N. V.; Gregory, R.; Werho, D.; Kulik, J.; Tam, G.; Irwin, E.; Wang, X.; La, L. B.; Hobbs, C.; Garcia, R.; Baker, J.; White, B. E.; Tobin, P. *J. Electrochem. Soc.* **2004**, *151*, F220–F227.

Umezawa, N.; Shiraishi, K.; Sugino, S.; Tachibana, A.; Ohmori, K.; Kakushima, K.; Iwai, H.; Chikyow, T.; Ohno, T.; Nara, Y.; Yamada, K. *Appl. Phys. Lett.* **2007**, *91*, 132904/1–132904/3.

Ushakov, S. V.; Brown, C. E.; Navrotsky, A. *J. Mater. Res.* **2004**, *19*, 693–696.

Van, T. T.; Hoang, J.; Ostroumov, R.; Wang, K. L.; Bargar, J. R.; Lu, J.; Blom, H.; Chang, J. P. *J. Appl. Phys.* **2006**, *100*, 073512/1–073512/7.

Van, T. T.; Bargar, J. R.; Chang, J. P. *J. Appl. Phys.* **2006**, *100*, 023115/1–023115/8.

Van, T. T.; Chang, J. P. *Appl. Phys. Lett.* **2005**, *87*, 011907/1–011907/3.

Vitchev, R. G.; Defranoux, C.; Wolstenholme, J.; Conard, T.; Bender, H.; Pireaux, J. J. *J. Electron Spectrosc. Relat. Phenom.* **2005**, *149*, 37–44.

Wang, J.; Li, H. P.; Stevens, R. *J. Mater. Sci.* **1992**, *27*, 5397–5430.

Wang, S. J.; Chai, J. W.; Dong, Y. F.; Feng, Y. P.; Sutanto, N.; Pan, J. S.; Huan, A. C. *Appl. Phys. Lett.* **2006**, *88*, 192103/1–192103/3.

Wang, T.; Ekerdt, J. G. *Chem. Mater.* **2009**, *21*, 3096–3101.

Wang, T.; Ekerdt, J. G. *Chem. Mater.* **2010**, *22*, 3798–3806.

Wang, T.; Ekerdt, J. G. *Chem. Mater.* **2010**, *submitted*.

Wei, F.; Tu, H.; Wang, Y.; Yue, S.; Du, J. *Appl. Phys. Lett.* **2008**, *92*, 012901/1–012901/3.

Wilk, G. D.; Wallace, R. M.; Anthony, J. M. *J. Appl. Phys.* **2000**, *87*, 484–492.

Wilk, G. D.; Wallace, R. M.; Anthony, J. M. *J. Appl. Phys.* **2001**, *89*, 5243–5275.

Wooten, F. *Optical preoperties of Solids*; Academic: New York, 1972.

Yamamoto, Y.; Kita, K.; Kyuno, K.; Toriumi, A. *Appl. Phys. Lett.* **2006**, *89*, 032903/1–032903/3.

Yang, Z. K.; Lee, W. C.; Lee, Y. J.; Chang, P.; Huang, M. L.; Hong, M.; Yu, K. L.; Tang, M.; Lin, B.; Hsu, C.; Kwo, J. *Appl. Phys. Lett.* **2007**, *91*, 202909/1–202909/3.

Yeo, Y.; King, T.; Hu, C. *Appl. Phys. Lett.* **2002**, *81*, 2091–2093.

Zeng, W.; Eisenbraun, E.; Frisch, H.; Sullivan, J. J.; Kaloyeros, A. E.; Margalit, J.; Beck, K. *J. Electrochem. Soc.* **2004**, *151*, F172–F177.

Zhang, M. H.; Rhee, S. J.; Kang, C. Y.; Choi, C. H.; Akbar, M. S.; Krishnan, S. A.; Lee, T.; Ok, I. J.; Zhu, F.; Kim, H. S.; Lee, J. C. *Appl. Phys. Lett.* **2005**, *87*, 232901/1–232901/3.

Zhao, X.; Vanderbilt, D. *Phys. Rev. B* **2002**, *65*, 233106/1–233106/4.

Zhao, Y.; Kita, K.; Kyuno, K.; Toriumi, A. *Appl. Phys. Lett.* **2009**, *94*, 042901/1–042901/3.

Zhu, W.; Tamagawa, T.; Gibson, M.; Furukawa, T.; Ma, T. *IEEE Electron. Device Letters*. **2002**, *23*, 649–651.

NIST X-ray Photoelectron Spectroscopy Database; http://srdata.nist.gov/xps/.

International Technology Roadmap for Semiconductor.

Powder Diffraction File PDF 08–0342; International Center for Diffraction Data: Newtown Square, PA, 2001

Vita

Tuo Wang was born in Tianjin, China. He attended Tianjin No. 20 High School from 1999 to 2002. In September of 2002, he enrolled at Tianjin University in Tianjin, China. Tuo received his Bachelor of Science in Chemical Engineering in July of 2006.

In August of 2006, Tuo began his graduate studies in chemical engineering at the University of Texas at Austin. Advised by Prof. John G. Ekerdt, he conducted research on the growth of hafnia-based thin films by atomic layer deposition (ALD) as a high permittivity material. After building and optimizing an ALD system, he studied the growth and properties of various hafnia-based oxides to explore the underlying mechanism determining the film thermal stability of the amorphous phase.

Tuo Wang authored or co-authored seven publications that are either in print or in review in refereed journals at the date of the dissertation filing. Research results during graduate studies were presented at the 2008 AIChE Annual Meeting in Philadelphia, PA, in November of 2008 and the AVS 56th International Symposium and Exhibition in San Jose, CA, in November of 2009.

Permanent address: 5106 N Lamar Blvd, Apt 148, Austin, TX 78751
This dissertation was typed by the author.